GEORGIA INSTITUTE OF TECHNOLOGY — OFFICE OF CONTRACT ADMINISTRATION

PROJECT ADMINISTRATION DATA SHEET

[X] ORIGINAL [ ] REVISION NO. ____

Project No. Q5218-7A0 G-41-667 (Cont. of G-41-653) XXXXX/GIT DATE 1 / 3 /85

Project Director: Dr. Uzi Landman School/~~Lab~~ Physics

Sponsor: Department of Energy, Oak Ridge Operations

Type Agreement: Contract DE-AS05-77ER05489; Mod. A007

Award Period: From 1/1/85 To 12/31/85 (Performance) 12/31/85 (Reports)

Sponsor Amount:	This Change	Total to Date
Estimated:	$ 167,000*	$ 1,020,306
Funded:	$ 167,000	$ 1,020,306

Cost Sharing Amount: $ 33,251 Cost Sharing No: G-41-326

Title: The Structure and Reactivity of Heterogeneous Surfaces and Study of the Geometry of Surface Complexes

ADMINISTRATIVE DATA — OCA Contact Brian J. Lindberg x4820

1) Sponsor Technical Contact:

Drs. T. A. Kitchens and M. C. Wittles
U. S. Dept. of Energy
Division of Material Sciences, ER-132
Office of Basic Energy Sciences
Mail Stop G-226 GTN
Washington, DC 20545

2) Sponsor Admin/Contractual Matters:

Mr. J. D. Burleson, Contracting Officer
U. S. Dept. of Energy
Oak Ridge Operations
Post Office Box # E
Oak Ridge, Tennessee 37831
(615) 576-7564

Defense Priority Rating: N/A Military Security Classification: N/A

(or) Company/Industrial Proprietary: N/A

RESTRICTIONS

See Attached Government Supplemental Information Sheet for Additional Requirements.

Travel: Foreign travel must have prior approval – Contact OCA in each case. Domestic travel requires sponsor approval where total will exceed greater of $500 or 125% of approved proposal budget category.

Equipment: Title vests with GIT, if acquired by us and listed in Appendix "A"

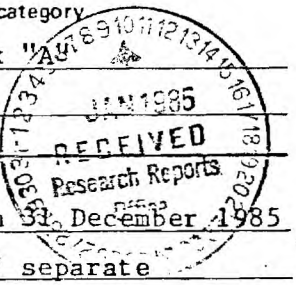

COMMENTS:

Mod A007 Adds $167,000 and extends period of Performance through 31 December 1985 as a continuation of G-41-653. New project number is because of separate financial reporting requirement.

*Total Contract Value (Including Previous Project #'s) is $1,020,036.

COPIES TO:

ID# 02.141.002.85.005

Project Director	Procurement/EES Supply Services	GTRI
Research Administrative Network	Research Security Services	Library
Research Property Management	Reports Coordinator (OCA)	Project File
Accounting	Research Communications (2)	Other A. Jones

FORM OCA 4 383

GEORGIA INSTITUTE OF TECHNOLOGY OFFICE OF CONTRACT ADMINISTRATION

SPONSORED PROJECT TERMINATION/CLOSEOUT SHEET

SR74

Date 9/12/86

Project No. G-41-667 Contract No. DE-AS05-77ER05489 School/~~XXX~~ PHYSICS
(All prior projects under this contract have already been terminated.)

Includes Subproject No.(s) N/A

Project Director(s) Uzi Landman ~~XXXX~~ / GIT

Sponsor Department of Energy, Oak Ridge Operations

Title The Structure and Reactivity of Heterogeneous Surfaces and Study of the Geometry of Surface Complexes

Effective Completion Date: 12/31/85 (Performance) (Reports)

Grant/Contract Closeout Actions Remaining:

- [ ] None
- [X] Final Invoice or Final Fiscal Report - Covering all projects under this contract no.
- [X] Closing Documents
- [X] Final Report of Inventions - Questionnaire sent to P.I.
- [X] Govt. Property Inventory & Related Certificate - Covering all projects under this contract no.
- [ ] Classified Material Certificate
- [ ] Other

Continues Project No. G-41-653 Continued by Project No.

COPIES TO:

Project Director
Research Administrative Network
Research Property Management
Accounting
Procurement/GTRI Supply Services
Research Security Services
Reports Coordinator (OCA)
Legal Services

Library
GTRC
Research Communications (2)
Project File
Other A. Jones
I. Newton
R. Embry

OPM OCA 89.285

"THE STRUCTURE AND REACTIVITY OF HETEROGENEOUS SURFACES AND STUDY OF THE GEOMETRY OF SURFACE COMPLEXES"

Progress Summary (1977-1985) and
Progress Report for
January 1, 1985 - December 31, 1985

THE STRUCTURE AND REACTIVITY OF HETEROGENEOUS SURFACES AND STUDY OF THE GEOMETRY OF SURFACE COMPLEXES

Progress Summary (1977-1985) and

Progress Report for January 1, 1985 - December 31, 1985

Uzi Landman

School of Physics

Georgia Institute of Technology

Atlanta, Ga. 30332

Summary of Progress

June 1, 1977 - December 31, 1985

PREPARED FOR THE U. S. DEPARTMENT OF ENERGY

UNDER CONTRACT NO. DE-AS05-77ER05489

DOE F 1332.16 (10-84)
(Formerly RA-427)

OMB Approval
No. 1910-1400

U. S. DEPARTMENT OF ENERGY

UNIVERSITY CONTRACTOR, GRANTEE, AND COOPERATIVE AGREEMENT RECOMMENDATIONS FOR ANNOUNCEMENT AND DISTRIBUTION OF DOCUMENTS

See Instructions on Reverse Side

1. DOE Report No. DOE/ER/04589-1

2. DOE Contract No. EG-S-05-5489

3. Title The Structure and Reactivity of Heterogeneous Surfaces and Study of the Geometry of Surface Complexes

4. Type of Document ("x" one)
- [X] a. Scientific and technical report
- [ ] b. Conference paper:
  - Title of conference _____
  - Date of conference _____
  - Exact location of conference _____
  - Sponsoring organization _____
- [ ] c. Other (Specify) _____

5. Recommended Announcement and Distribution ("x" one)
- [X] a. Unrestricted unlimited distribution.
- [ ] b. Make available only within DOE and to DOE contractors and other U. S. Government agencies and their contractors.
- [ ] c. Other (Specify) _____

6. Reason for Recommended Restrictions

7. Patent and Copyright Information:
Does this information product disclose any new equipment, process, or material? [X] No [ ] Yes If so, identify page nos. _____
Has an invention disclosure been submitted to DOE covering any aspect of this information product? [X] No [ ] Yes
If so, identify the DOE (or other) disclosure number and to whom the disclosure was submitted.
Are there any patent-related objections to the release of this information product? [X] No [ ] Yes If so, state these objections.
Does this information product contain copyrighted material? [X] No [ ] Yes
If so, identify the page numbers _____ and attach the license or other authority for the government to reproduce.

8. Submitted by: Uzi Landman
Name and Position (Please print or type): Professor
Organization: School of Physics, Georgia Institute of Technology
Signature: U. Landman
Phone: (404) 894-3368
Date: August 28, 1985

FOR DOE OR OTHER AUTHORIZED USE ONLY

9. Patent Clearance ("x" one)
- [ ] a. DOE patent clearance has been granted by responsible DOE patent group.
- [ ] b. Report has been sent to responsible DOE patent group for clearance.

TABLE OF CONTENTS

I. INTRODUCTION: PROJECT OUTLINE

Investigations of fundamental physical processes and underlying materials properties, materials modifications via processing (or in the course of operation) and novel material preparation and design are a major thrust of modern materials science. Such investigations contribute to our basic knowledge of materials phenomena and impact materials technologies. It is often the case that understanding, initiation and improvement of technological applications require, or are induced by knowledge on a basic level. In particular, further progress in a number of energy related technologies (such as catalysis, prevention of degradation via wear, tribological processes, or corrosion, recovery of damage, growth of novel materials, electrochemical processes, microelectronics, solar energy conversion and fusion) requires basic understanding of materials (structure, dynamics, response and transformations) and the identification of materials parameters and ambient conditions which control the pathways, rates and efficiencies of chemical and physical materials processes.

Our research program focuses on four major materials science areas:

(1) surface, interface and interphase-interface phenomena;

(2) phase transformations; materials growth and materials processing;

(3) small material aggregates; and systems in confirming environments.

The complex nature of the materials systems which we investigate, requires a comprehensive, concerted research program which combines the development and implementation of novel theoretical methods and modeling strategies with employment of established theoretical analytical techniques. In particular, studies of certain of the materials problems which we explore in the context of the technologies to which they apply, require special modeling considerations and simulation techniques which while preserving the

complexity (and reality) of the system under study, render it soluble thus allowing systematic studies.

In the following we summarize our research achievement since the initiation of the Department of Energy contract support to our project (progress realized during the 1985 reporting period is identified by a (*) to the left of the subject heading.

II. RESEARCH TOPICS

1. Surfaces, Interfaces and Interphase-Interface Phenomena (1-36)

The importance of surfaces and interfaces in a variety of chemical and physical processes has been long recognized. Due to the wide range of applications and phenomena ranging from chemical catalysis, corrosion research, electrochemistry and the application of surface-active agents (detergents, adhesives, etc.), to electronics and methods of crystal growth, this field of research is of an interdisciplinary nature, referred to as surface and interface science.

All physical surfaces are in fact interfaces between material systems. The systems connected by the interface may possess several common physical attributes, such as chemical identity, composition, state of aggregation and structure, as in certain solid-solid or liquid-liquid interface systems, or may be of vastly different physical character as in solid-gas and solid-liquid interphase-interface systems. In addition, we distinguish between equilibrium interfaces where all components of the system are in thermodynamic equilibrium and nonequilibrium interfaces occurring in phase transformations such as crystal growth (from the liquid or gas) or melting. In all cases, the interface region is of finite extent often possessing unique physical characteristics (crystallographical structure, electronic, vibrational and elementary excitation spectra) different from those of the systems connected through it.

In the past two decades there has been a rapid proliferation in the development and application of spectroscopies which probe the composition, crystallographical arrangement and electronic and vibrational structure of surfaces on the atomic scale. At the same time theoretical formulations which allow the analysis of experimental observations and calculations of surface

properties have been advanced. At this stage of development emphasis was placed on the characterization of surface systems with less work directed at the dynamics of surface interactive processes. Static information such as (i) atomic arrangement at the top-most layers of the solid and that of adsorbed species (LEED, ion scattering, SEXAFS); (ii) surface electronic structure (UPS, AES, EELS, ILEED); and (iii) vibrational structure (EELS and IR), along with theoretical studies of the above issues are most valuable (and often a prerequisite) to the understanding of surface phenomena. At the same time, new methods and approaches are necessary in order to tackle successfully the dynamical aspects of surface interactions. The budding generation of new experiments (some of which are well known in gas-phase chemical dynamics but novel in their employment to surface systems) such as laser-induced fluorescence studies of the rotational and vibrational-state distribution of molecules adsorbed, scattered and thermally desorbed from metallic surfaces, rotational and vibrational state distributions obtained from analysis of optical emission from electronically excited ejected molecules, measurements of angular distributions of desorbed particles, investigations of diffusion rates and mechanisms (FIM, FEM) provide the impetus and have profound implications on theoretical strategies for future modeling of the physical and chemical processes which underly the mechanisms and dynamics of elementary surface interactive and rate processes.

Recognizing the multifaceted and interdisciplinary aspects of surface phenomena we have directed our research program such as to provide a comprehensive approach to these problems.

a) Surface Structure: (1-11)

The changes in the atomic coordination and conduction-electron distribution due to a termination of a solid by a surface (or interface) cause

near surface structural changes. Thus it has long been observed that the spacing between the outermost atomic planes of a metal crystal often deviates from the bulk spaceing. This phenomena known as surface relaxation, is most pronounced for open (loosely packed) crystal faces. Theoretical investigations of surface relaxation require a minimization of the total energy of the semi-infinite metal crystal with respect to the structural parameters, which in turn requires an expression for the total energy which depends explicitly on the identity of the ionic species and their spatial arrangement. Unlike rare-gas, molecular, and ionic systems for which satisfactory descriptions may be given in terms of pairwise (and higher-order) interactions, it is well known that the cohesive energy of a metal contains, in addition, density dependent contributions which do not depend on interparticle distances (and thus may not be expressed via pair-potentials) and that the metallic effective pair potentials themselves depend on the conduction-electron density distribution. Therefore, relaxation models based solely on pair-interactions (semi-empirical or theoretically calculated) are inadequate.

In order to elucidate the energetics of surface interactions and the nature of surface relaxation phenomena and to provide a theory of predictive capabilities we have developed theoretical models for the total energy of a semi-infinite simple metals which are not restricted to crystalline surfaces and allow investigations of both single and multi-component systems.

These developments have led to the formulation and implementation of a total energy minimization scheme based on pseudo-potential theory for simple metals. In this theory, the total energy is calculated and minimiized as a function of the atomic positions, self-consistently with the corresponding conduction electron density distribution, while preserving the

three-dimensional crystalline nature of the semi-infinite solid.

Our studies resulted in the prediction of damped oscillatory multi-layer relaxation phenomena and provided quantitative estimates of surface relaxations for simple metals. This work provided the impetus for refined LEED and ion-scattering experiments and analysis which have verified the existence of the theoretically predicteed multi-layer relaxations (relaxation in interlayer spacings as well as interlayer registry at high-index surfaces), and when applicable, resulted in quantitative agreement with the theoretical results (see references in ref. 24) and results of a joint experimental (ion
(*) scattering by J. W. H. Frenken and J. F. Van der Veen, FOM, Amsterdam, Holland) - theoretical study of the Pb(110) surface[9]).

In addition we have used the theory to investigate surface segregation phenomena[(7)]. We have discovered multilayer oscillatory segregation in binary simple-metal alloy surfaces. Recent atom-probe composition depth-profiles (T. T. Tsong et al., Surface Science 149, L7 (1984)) show such non-monotonic segregation behavior.

b) Surface Interactions and Reactions (12-35)

One of the major objectives of surface science is the understanding of the fundamental processes involved in chemical reactions catalyzed by solid surfaces. A catalyzed surface reaction may conveniently be described by a sequence of elementary kinetic steps such as adsorption (which may proceed via stages involving precursor states, physisorption etc.); diffusion (on the surface and in certain cases through the bulk); reaction (dissociation, association, rearrangement, etc.) and desorption. The traditional thermochemical analysis of reactions involving the balance of heats of the above distinct processes, such as heats of adsorption, desorption, dissociation, and bond formation, provides criteria for the occurrencce of

certain reaction paths. However, such analysis, while determining the direction of the process in the reactants-products space, does not provide detailed information about the reaction rates and the fundamental microscopic processes which govern them. The employment of specific catalytic agents in a chemical reaction provides the means for modifying reaction paths and rates. In addition, through the use of the proper catalyst a particular reaction channel, selected from the manifold of thermodynamically allowed ones, may be enhanced. In order to enable one to choose specific catalysts with the objective of optimizing the yield of a desired reaction product it is necessary to develop an understanding of the microscopic interaction processes and to identify the physical parameters of the catalytic system (catalyst, reactants, and ambient conditions) which govern the outcome and rate of the reaction.

(i) Surface Diffusion (12-25)

Diffusion processes on or in the vicinity of surfaces are of importance in many surface controlled, or driven physical and chemical phenomena. Such phenomena include crystal growth, surface phase transformations, annealing and recovery of damage, surface and interfacial segregation and chemical processes, heterogeneously catalyzed by surfaces.

The advent, development and application of experimental techniques such as Field Ion Microscopy (FIM) and Field Emission Microscopy (FEM) provide quantitative information about the microscopic nature of surface diffusion processes and serve as the impetus for refined theoretical studies, and methods of analysis. The objective of these studies is to understand on a microscopic level the mechanism, kinetics, dynamics and energetics (all of which are related) of surface diffusion. It is convenient to classify the theoretical approaches as: (a) stochastic processes, (b) dynamical

simulations, and reaction dynamics.

Stochastic Models: We have developed a general stochastic description[12-22] of diffusion processes which incorporates a detailed set of states (and corresponding transition rates), through which the system evolves and allows the investigation of atomistic mechanisms of diffusion in complex systems. When applied to the analysis of experiments of sufficient resolution the method provides a means of determining the "spectroscopy of internal states". The internal states may correspond to the energetics of the motion (i.e., they may represent selected points on the energy surface), spatial configurations (as in the description of cluster diffusion) or other characteristic internal states which may participate in the migration mechanism. We have shown that for a number of varied transport systems the set of allowable states can be mapped onto lattices, possibly with multiple sites in each unit cell[18]. The stochastic time development of these systems, which may be semi-Markovian or non-Markovian, can be treated as a continuous-time random walk (CTRW) process on these lattices.

These methods provide a framework and explicit expressions for the analysis of FIM diffusion data and the extraction of rate parameters (frequency factors and activation energies) for complex (multi-state) diffusion processes.

(*) Dynamical Simulations: The nature of current experimental probes limits the temporal resolution with which diffusion processes can be studied. Valuable information about diffusion systems can be obtained via computer dynamical simulation which enable investigations on arbitrarily short time scales and refined spatial resolution.

We have performed extensive computer simulations of single particle and cluster diffusion on crystalline surfaces.[23-25] In these simulations we have

employed "conventional" molecular dynamics methods as well as special techniques which allow determination of rates of rare-event processes. Of particular interest is our finding of a dynamical enhancement of a dimer-diffusion rate over the single particle rate. The enhancement originates from the dimer librational motion which through coupling to the substrate provides an effective channel to energy flow. The dependence of the dynamical enhancement on the system characteristic parameters (masses, interaction potential parameters) and ambient conditions (temperature) have been investigated.

(ii) Desorption (25-31)

Energy dissipation and redistribution via coupling to substrate phonons is likely a dominant process in many surface reactive and scattering processes. Of paramount importance for the understanding of reaction dynamics on a microscopic level are the mechanisms of coupling and energy exchange and redistribution between the reactants.

We have developed a microscopic model of thermal desorption[26] which combines a microscopic derivation of the substrate coupling to the adsorbate vibrations with a stochastic description of the excitation evolution (i.e., climbing the vibrational ladder of the adsorbate-surface bond). Additionally, we have proposed a "door-way" mechanism in which the need for (low probability) multiphonon mechanisms which are otherwise necessary in order to excite bond-stretch modes is circumvented via coupling first to low-frequency bending or wagging modes of the adsorbate. Subsequently the excitation is transferred to the higher-lying stretch vibrational levels leading to desorption. The model provided quantitative agreement, particularly for desorption rates of weakly bonded species, and has been used by other researchers in further studies.

Adsorption (or trapping) of a gas molecule by a surface lowers the spatial dimensionality of the molecular degrees of freedom. In addition the motions (translational and rotational), of the adsorbed molecule may be hindered by the substrate. Upon desorption to the gas phase the desorbed species regains the unhindered three-dimensional motions. We have analyzed in detail the states and spectra[31] of hindered molecular motions on surfaces and have used them in conjunction with a model of desorption.

In our model[24,30] the "localization" energy due to the hinderance of the adsorbate motions is converted upon release, to rotational and center of mass translational energy. Our result predict hot-rotational desorbed molecules, depending on the degree of hinderance in the initial state. The model suggests a mechanism for the existence of high-rotational states observed in recent state-selective measurements of desorbed species.

(*) (iii) Binding to Surfaces (33-35)

Knowledge of the mechanisms and energetics of atoms and molecule binding to solid surfaces is an essential element in the development of a fundamental theory of catalytic and other processes.

Water is one of the most abundant chemical species in our environment and the nature of its interaction with metal surfaces is of great importance for the elucidation of the mechanisms of corrosion, catalytic reactions, electrochemical processes in aqueous solutions and ice nucleation on surfaces. Motivated by recent high-resolution-electron-loss (EELS) experiments of monomer H_2O adsorption aat low temperatures of Cu(100) (S. Andersson et al., Chem. Phys. Lett. 104, 306 (1984)) we have developed and performed molelcular-orbital self-consistent-field cluster model calculations of H_2O adsorption on copper.[33]

In our calculations we have used an extended basis set spin-unrestricted

SCF-LCAO method with local Xα exchange, and performed systematic optimizations with regard to the molecular internal coordinates as well as the location and orientation of the molecule with respect to the metallic cluster. For a Cu_5 cluster we have determinied that in the optimal configuration the molecule is adsorbed in the on-top site arrangement, with an adsorption energy of 0.38 eV. Bonding is through the oxygen with the molecular plane tilted from the normal by 70^o. Bonding involves the H_2O lone-pair orbitals and is accompanied by a charge donation to the metal (0.15e). We have also constructed the potential surface for inter- and intra-molecular vibrations and have determined the normal mode frequencies. The geometry, magnitude of adsorption energy and vibrational frequencies are in agreement with experimental observations. Additionally, we have discussed in detail the binding mechanism. This is the first non-semi-empirical study of H_2O adsorption on a transition metal surface, and as such sets a bench-mark for further studies.

The electrical and optical properties of bulk semiconductors and semiconductor interfaces (semiconductor-vacuum or metal-oxide semiconductor (MOS) devices) are strongly affected by impurities. The energy levels and states of the impurity should depend on the distance from the interface. In order to analyze the results of experiments performed on MOS devices we have developed a variational solution metho[d34,35] to the effective mass equations describing a hydrogenic donor impurity located near semiconductor-vacuum and semiconductor-insulator interfaces. The interface was modeled via imposing an infinite potential barrier, which is an excellent assumption due to the height of the surface barrier ($\sim$ 3 eV in $Si-SiO_2$) in comparison to the millivolt binding energies of the shallow donor impurity. In our method we have used a non-hydrogenic basis set which assures completeness (without the need to use Coulomb wave functions) and have solved accurately for the ground and excited

states, as a function of the distance of the impurity from the interface. Comparison of our results to the experimental data allowed us to conclude that the impurities in the MOSFET device used in the experiment were located in the SiO_2 layer at a distance of $\sim$ 10-15 Å from the interface. Ground and excited state spectra for impurities near the (100) interface (vacuum and Si-SiO_2) of Si and (111) surface of Ge, as a function of the location of the impurity were calculated. These can be used in analyses of the spectroscopical studies of these systems.

(c) Surface Lattice Dynamics

The development of high-resolution-electron loss spectroscopy (EELS) and ultra-high vacuum infra-red studies of clean surface and adsorption systems provides the motivation for theoretical development of methods for calculating the vibrational spectra of solid surfaces. Such information is of relevance for studies of surface stability, perfect modes, the identification of steps in catalytic reactions, surface thermal expansion, surface phase-transformations (melting) and energy transfer in gas-surface collisions.

Several of the theoretical issues involved in surface lattice dynamics calculation are: input force constants for the near surface region, rotational invariance of the model, efficient methods for high-index (large unit cell) surfaces, and calculatiions of single defect modes.

The first issue has been addressed by us in our studies of surface energetics[4] (see discussion under (a) surface structure). We found, that for simple metals the forces on ions near the surface region are highly non-isotropic and that the effective pair-potentials for ion-pairs near the surface region are non-isotropic and as a function of distance differ in magnitude and curvature from the bulk pair-potentials.

The traditional surface lattice-dynamics method employs the dynamical

matrix for a slab configuration. This method applies only to ordered structures and becomes computationally prohibitive for structures with a large unit cell. In order to overcome this difficulty we have introduced the first application of the recursion method (developed originally by Heine and coworkers for calculations of electronic spectra in solids) to a lattice dynamical problem[36]. We have applied the method to study the origin of the high-frequency modes above the bulk maximum frequency, observed by EELS experiments, at the stepped Pt(332) surface. In this study the near surface force constants were treated parametrically. We have shown that the observations can be explained by a 30-40% increase in the force-model parameters for atom located at the steps (unlike previous estimates which were based on one-dimensional models, requiring over 70% changes). Apart from the scientific findings, we have demonstrated for the first time the use of the recursion approach in lattice dynamics calculations. The method has since been further developed and applied extensively by other workers.

(d) Equilibrium Interphase-Interfaces (24)

The structure and dynamics of crystal-liquid interface systems have been the subject of increasing theoretical (as well as experimental) interest. Apart from the pure scientific interest, microscopic understanding of these interfaces is of importancne in developing a microscopic theory of crystal growth under quasi-static and under ultra-rapid growth conditions (such as in laser and electron beam annealing). In this section we report our work on the equilibrium interfaces delaying a discussion of their properties under growth conditions until the next section ((2) phase transformations; material growth).

Theoretical methods of treating the equilibrium thermodynamics of interfaces in general were introduced by Gibbs in 1878 and much of this seminal work still forms the conceptual framework for research in this field.

Most studies aimed towards the development of a molecular theory of equilibrium interfaces are phenomenological in nature. The main difficulty in developing a microscopic theory of the solid-liquid interface (and other liquid interfaces) arises from the presence of the liquid. A satisfactory theory has not yet been developed for the description of homogeneous liquids, although significant progress in this direction has been made, particularly through the advent of numerical simulation methods. The problem of a solid-liquid interface is further complicated since the structural and dynamical properties of the liquid are perturbed by the presence of the solid. The three main theoretical approaches which were developed and applied in investigations of solid-liquid interfaces are: (1) The model approaches which follow and extend the original work by Bernal of the structure of bulk liquids [applied to fcc(111) and hcp(0001) interfaces]. (2) Statistical mechanics theories which employ the liquid-state integral equation methodology in juxtaposition with perturbation theory [applied to fcc (100) and (111) interfaces]. (3) Monte Carlo and molecular dynamics simulation methods [applied to fcc (100) and (111) interfaces]. All three treatments result in a diffuse, layer structured in the liquid, interface. However, the model approaches yield a density deficit at the immediate vicinity of the crystalline surface which is not observed in molecular dynamics simulations. This discrepancy is due partly to the static nature of the crystalline surface in the hard sphere models.

We have developed and applied molecular dynamics simulations for studies of liquid-crystal interface systems. In these studies we used generic 6-12 Lennard-Jones potentials and have performed investigations for the three low-index faces of an fcc crystal.

Our main findings may be summarized as follows:

While all three low-index fcc crystal-liquid interface systems studied by us exhibit a diffuse, layer-structured interfaces subtle differences due to crystalline face anisotropy have been detected. It appears that the extent of the diffuse interface is largest for the (100) interface, decreasing slightly for the (111) interface and further decreasing for the (110) interface. Upon analysis we find that for the (100) interface intralayer order is changing across the interface transition layer in a gradual manner, as compared to the more abrupt changes occurring for the (111) and (110) interfaces.

The crystalline anisotropy of the transition interface region is further demonstrated via the different manners in which the particle densities and interlayer spacings vary across that region for the (111) and (100) interfaces. Analysis of the particle density profiles shows that for the (111) system the interlayer spacing remains constant throughout the transition region, equaling roughly that of the crystalline interlayer spacing. The density decrease is achieved for this surface by reducing the number of particles in successive layers. At the (100) interface the interlayer spacing in the transition layer increases gradually from the crystalline value while the number of particles per layer remains constant. These differences between the two interfaces reflect the larger dissimilarity between the bulk liquid structure and the local arrangement in the interfacial liquid layer at the (100) surface, than between the structures of the bulk liquid and interfacial liquid at the (111) surface. At the (100) surface the induced local structure in the liquid in the vicinity of the crystal is octahedral while hard-sphere packing near a flat plane exhibits a nearly perfect two-dimensional hexagonal structure which upon approaching the three-dimensional liquid bulk turns into a

polytetrahedral structure of pentagonal symmetry. At the (111) surface the symmetry of the crystalline potential matches closely that of a liquid in contact with a flat wall. The oscillatory behavior of the density profile in the transition region of the (111) interface is then due to the transition between the two-dimensional symmetry of the packing at the immediate vicinity of the crystalline surface and that which occurs in the three-dimensional spherically symmetric bulk liquid.

The diffusion constants at the interface regions for the three surfaces studied, are similar in magnitude. Furthermore, the diffusion constants do not show significant anisotropy.

(*) The Equilibrium Crystal-Melt Interface of a Semiconductor: Si(100)-melt

From a technological point of view, perhaps the most important interface systems are the crystal-melt interfaces of semiconductors, Si in particular. Fundamental understanding of these interfaces is of vital importance for the development and improvement of semiconductor device preparation using liquid-phase epitaxy, laser annealing, and zone-melting recrystallization methods. In particular, the network of low-angle grain-boundaries that form during zone-melting recrystallization and the kinetics of rapid growth in laser annealing experiments has been interpreted in terms of the morphology of the solid-melt interface.

In order to understand the nature of these interfaces we have developed molecular dynamics simulations of the melting, dynamics and structure of the interface between Si(100) and its melt. Due to the directional bonding characteristic to tetrahedral semiconductors the potentials for these materials must include contributions beyond pair-wise interactions (i.e., non-additive, angle dependent contributions). We have employed optimized two- and three-body potentials which have been suggested

recently by Stillinger and Weber and have shown to yield a rather adequate description of the structural properties of crystalline and liquid silicone. Our molecular dynamics method which incorporates these potentials allows in addition for density variations (i.e., constant-pressure). These simulations are extremely demanding and have been performed on the CRAY-XMP computer at the Magnetic Fusion Laboratory (Livermore, California).

The most significant observation which we have made is the faceting of the equilibrium Si(100)-melt interface. The interface breaks up into facets defined by alternating (111) and (111) planes (see Figure). The extent (height) of the facets is $\sim$ 5 atomic layers. In addition the melt region in the vicinity of the solid (faceted) phase exhibits a degree of ordering and a limited region of "liquid layering" in the direction normal to the facet planes is observed. These results were obtained for two system sizes: a 24 layer system with 144 atoms/layer and a 48 layer system with 32 atoms/layer. We have also found indications that such faceting occurs upon melting of the crystal. As a result of a collaborative effort with an experimental group at the Philips Laboratories (Briarcliff Manor, N. Y., headed by Dr. Emil Arnold) an experimental confirmation of the faceted equilibrium structure of Si(100)-Si melt interface was obtained in situ, by means of a microscope equipped with visible and near-infrared video camera.

While ample evidence exists that the surfaces of crystalline silicon become faceted upon melting and that the solid-melt interface of a growing Si crystal establishes itself on the (111) crystal planes this is the first microscopic theoretical study of this equilibrium interface.

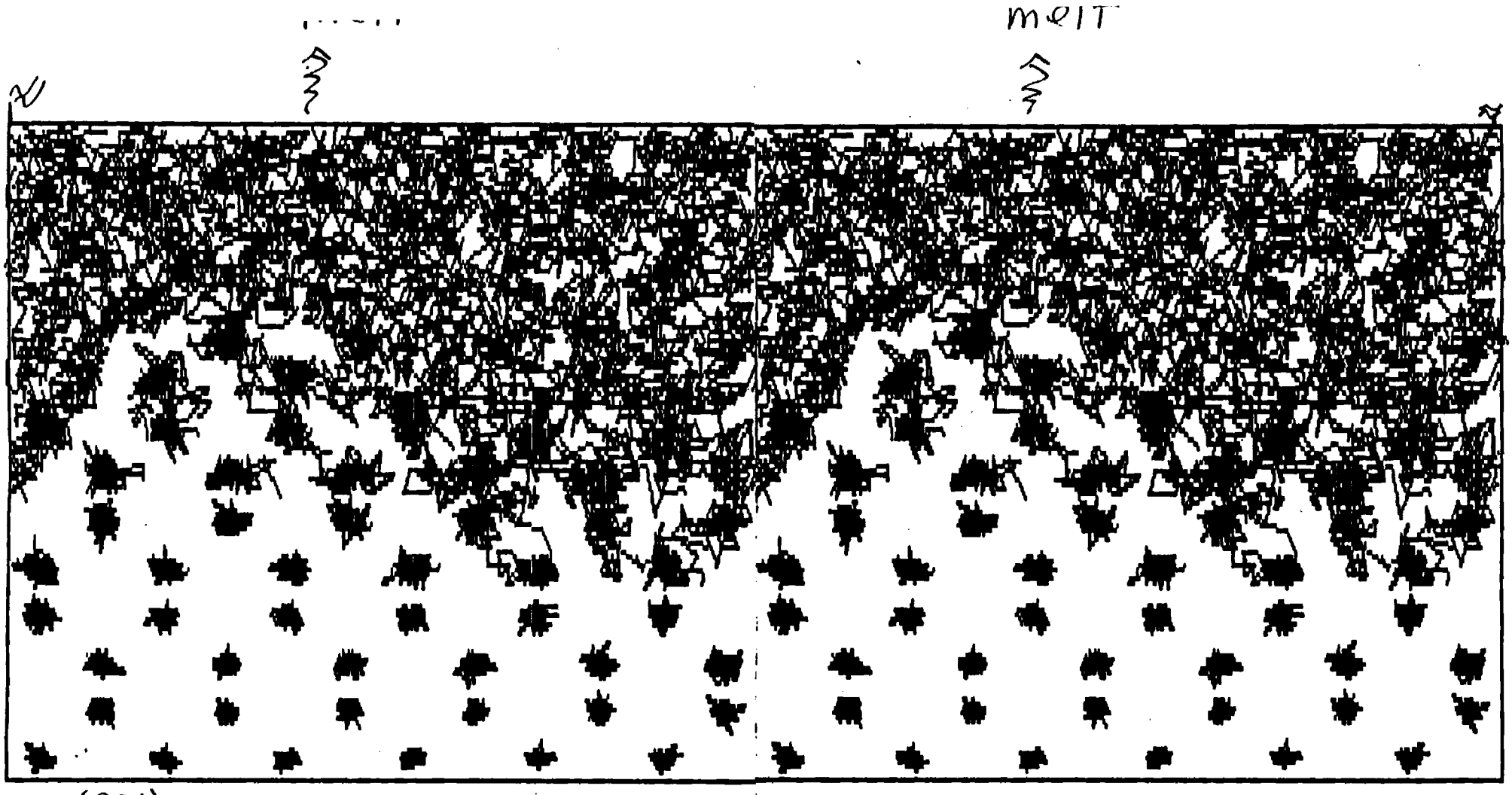

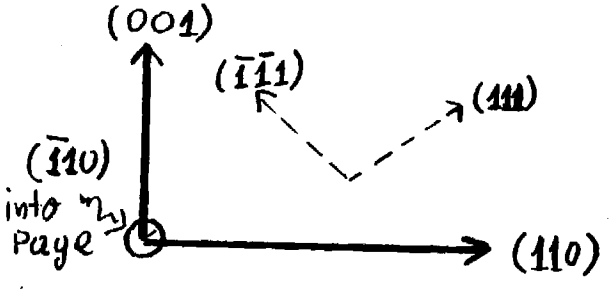

Figure 1: Particle real space trajectories projected onto the $(\bar{1}10)$ plane, showing faceting at the solid Si(100)-Si melt interface, obtained via molecular dynamics simulations. The facets are comprised of alternating (111) and $(\bar{1}\bar{1}\bar{1})$ crystal planes. Ordering in the liquid adject to the facet planes is seen.

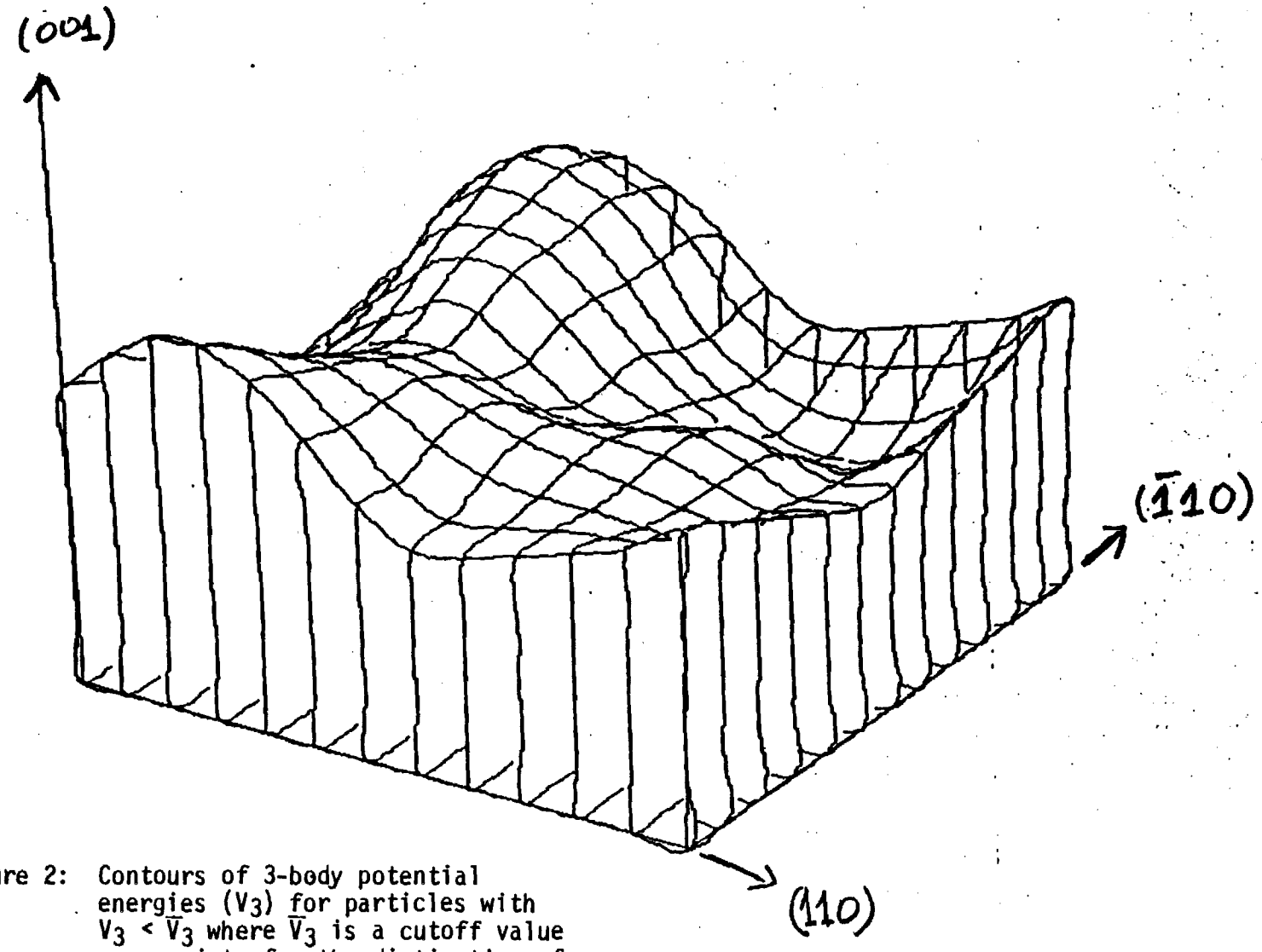

Figure 2: Contours of 3-body potential energies (V_3) for particles with $V_3 < \bar{V}_3$ where $\bar{V}_3$ is a cutoff value appropriate for the distinction of crystalline and liquid regions (the 3-body potential term is small in the crystalline region and larger in the melt).

2. Phase Transformations; Materials Growth and Materials Processing (37-42)

The search for novel materials which possess certain desired properties such as: reactivity, elasticity and strength, electronic, magnetic and optical characteristics, corrosion-immunity and other selected properties, is a frontier area of material science. Among the key issues of interest are methods of preparation and phase stability. Although it is well recognized that the method of preparation and treatment influences greatly the properties of solid materials, little is known about the microscopic mechanisms which govern the kinetics and dynamics of growth. Materials preparation techniques of particular interest are: (a) radiation and electron beam processing of materials for damage recovery, impurity segregation and the preparation of amorphous surface systems, (b) the preparation of glasses, metallic glasses in particular, (c) growth methods which allow the preparation of solid composite materials of unusual (non-thermodynamic equilibrium) compositions (such as laser or electron beam annealing and fast quench methods).

The development and successful applications of the above methods require detailed investigations of the coupling of intense radiation to matter, the structure and dynamics of liquid-solid interfaces, liquid melts and liquid metal alloys, and the nonequilibrium processes which govern solidification. Studies of materials growth (epitaxial and homogeneous, glassy materials, growth of ordered crystals on amorphous substrates and laser annealing) require development of interaction potential models and theoretical characterization methods which allow determination of the degree of order on a local scale and the monitoring of the evolution of the system (energetically and configurationally) towards equilibrium or long-lived metastable (amorphous) states. The ability to gain such knowledge is greatly enhanced by the use of simulation methods performed on high-speed computers and the

employment of modern statistical mechanics techniques. Coupled with spectroscopic methods and high resolution microscopy, such theoretical studies provide information on the atomic mechanisms and dynamics which control the materials growth and/or recovery processes.

(a) Liquid Phase Epitaxy, Melting and Rapid Solidification - Non Equilibrium Crystal - Melt Interfaces

Liquid Phase Epitaxy[37-39]: The reproducibility, structural quality and purity of crystals obtained via LPE depend critically on a number of growth parameters such as the temperatures of the solid and melt, temperature gradients (in the direction of growth and laterally), the rates of heat dissipation and the compositions. The growth parameters, coupled with specific material characteristics such as thermal conductivities, latent heat, segregation and diffusion coefficients and crystalline anisotropies of material properties govern the kinetics and dynamics of the solidification process and the characteristics of the eventual product.

The purpose of our investigations is to provide information about the microscopic dynamics and kinetics of epitaxial crystallization processes. For this purpose we have developed a Surface Molecular Dynamics method which allows one to perform detailed studies of the temporal evolution of interfacial phenomena. We have performed simulations for LPE using 6-12 Lennard-Jones potentials for highly supercooled and hot liquids, growing onto the (100) surface of an fcc crystal. The non-equilibrium evolution of the system was followed via monitoring of the particle density, potential energy and kinetic temperature spatial profiles in the direction of growth (normal to the (100) surface) as well as intraplane orientational order parameters and pair distribution functions. The main findings of our work were:

A detailed study of the density profiles and a number of order

parameters reveals that the first stage of the transformation involves a reorganization of particle density in a region of the liquid of thickness equivalent to 4-5 layers into a persistent stratified (layered) 3D structure in the z (001) direction which lacks intralayer crystalline order. Layers in this region further removed from the solid surface are more diffuse than the closer ones.

Intralayer order is established in a sequential manner, with the layer closer to the solid substrate ordering first and so on. We observed that intralayer ordering of a layer triggers ordering in the layer above it (further removed from the substrate) which in turn accelerates the ordering in the lower layer due to the latent heat of ordering and "crystalline" potential provided by ordering in the layer above.

For a melt in contact with a solid, both at above half the melting point, the crystallization speed was 100 m/sec, while starting from a liquid above the melting point in contact with a cold solid the speed is reduced to 5 m/sec.

Our prediction of a stratified interface structure developing in the melt adjacent to the growing surface of a crystal found recent support through the dynamic light scattering measurement by Cummins and Coworkers (Phys. Rev. B29, 2846 (1984)) and Bilgramm et al. (Phys. Rev. A 30, 946 (1984)). It is likely that the collective ordering in the stratified diffuse interphase-interface region is an important dynamical step in the kinetics of crystal growth.

Rapid Solidification (Laser Annealing)[40,24]: The ultrarapid solidification which follows the irradiation of a solid with pulsed laser or electron beams, commonly known as laser annealing, is the basis for the development of novel materials growth and processing techniques and is the subject of current intensive research efforts concerned with the evolution, phase

transformations, and properties of non-equilibrium materials systems. Experimental studies of the microscopic mechanisms of excitation and solidification in laser annealing systems are difficult due to the fast rates of the physical processes in these systems, necessitating the development of probes of combined temporal and spatial high resolution. Theoretical progress in understanding the dynamics and kinetics of rapid solidification phenomena is equally challenging due to the highly nonequilibrium nature of these systems and the lack of adequate theoretical methods for the description and analysis of materials under such extreme conditions. Nevertheless, significant progress on both the experimental and theroetical fronts has been realized recently, brought about via the development of novel experimental probes and theoretical simulation and modeling techniques (molecular dynamics, solution of moving boundary coupled heat and matter transport equations, and Monte Carlo studies of kinetic Ising models).

The main theoretical issues encountered in studies of laser annealing systems are (a) the mechanisms of radiation (photons, particles) coupling to solids, (b) nonequilibrium thermodynamics and stability analysis (metastability, morphological stability), and (c) the kinetics and dynamics of phase transformations, i.e., investigations of material processes involving changes in structure, compositin, and degree of order. Solidification and melting in general are nonequilibrium phenomena governed by heat and matter transport and kinetic processes at the moving interface between two phases (solid and melt). While the above processes have their origins in particle dynamics, heat and matter transport away from the solidification interface can be described adequately using continuum methods. However, treatment of transport and kinetic processes in the vicinity of the interface requires a microscopic theory, since transport properties in this region are expected to

exhibit a marked spatial variation on the atomic scale and interface kinetic processes are inherently of atomistic nature.

Motivated by these considerations, we have developed and performed molecular dynamics simulations of model laser annealing systems which allow detailed investigations of the dynamics and structure of solid-melt interfaces and studies of the microscopic mechanisms of melting and rapid solidification.

Our initial state is an equilibrated fcc crystalline system exposing one of the low-index faces, composed of 90% host particles with 10% substitutional randomly distributed heavier, larger, and stronger binding impurities, at a temperature $T = (4/7)T_{melt}$ and zero external pressure. The system is then subjected to the influence of a triangular in shape heat pulse of 1.6 ps in duration, allowing for heat conduction to the substrate reservoir.

Following the deposition of energy into the lattice by the heat pulse a region of the crystal melts. When the propagation of the melting front slows down we notice that the temperature of the melt in the region closer to the vapor side is still well above the melting temperature and that the volume of the system has expanded significantly. In addition, a well-developed diffuse, layer-structured in the melt, crystal-melt interface is observed. Subsequently the melting process stops and resolidification begins. Crystallization starts and proceeds while the kinetic temperature of the melt is still above the solid-liquid coexistance temperature. We did not observe any significant degree of supercooling near or at the crystallization front throughout the whole evolution of the system. The moving crystallization front is characterized again by a layer-structured in the melt diffuse interface, possessing density, structural, dynamic and transport properties intermediate between the bulk solid and melt phases connected through it. The final product for all the systems presented in this study is a perfect crystal

with a random substitutional impurity distribution.

From the above observations we conclude that the relaxation times which govern the rate at which the layer-structured diffuse solid-melt interface is established under non-equilibrium conditions are extremely short (occurring both during melting and resolidification). The anisotropic "liquid layering" which establishes the material density in the melt region preceding the solidification front, "prepares" the melt for the subsequent evolution of planar crystalline ordering. The unique structural and transport properties of the diffuse solid-melt interface may play an important role in the crystallizaton kinetics and affect the degree of crystalline perfection and impurity distribution in the resolidified material. We conjecture, that under conditions where the solidification front would be able to advance with a velocity which supercedes that which is necessary for the reorganization of the melt to form the anisotropically structured diffuse interface, a defective, perhaps amorphous, resolidified material would be obtained.

The crystallization velocities deduced from the data are v = 7.7, 10.0, and 8.4 m/s for the (111), (100), and (110) systems, respectively.

Crystal growth from the melt is often discussed in terms of the following mechanisms: (1) Two-dimensional nucleation, where upon nucleation of small monolayer "islands" growth proceeds by further attachment of atoms to the "islands" and spreading of these monolayers across the surface. According to the mechanism the growth rate will be negligibly small for small undercoolings. (2) "Continuous" or "normal" growth, where it is assumed that all atoms arriving at the surface of the solid substrate are able to stick to become solid (thus nucleation is not a necessary kinetic step). According to this mechanism the rate of growth increases with the degree of undercooling, becoming proportional to it for small undercoolings.

Attempts at unifying the two growth modes have been proposed. In particular, the model introduced by Cahn assumes that the free energy of the interface is a periodic function of its mean position relative to the lattice periodicity of the solid phase. Thus this model contains the idea of a diffuse (perhaps structured) solid-melt interface.

The two-dimensional nucleation mechanism is expected to be dominant for atomically smooth interfaces while continuous growth is expected to occur on rough surfaces. The plots of the crystalline interface position as a function of time exhibit different characteristic behavior as we go from the atomically smooth (111) face to the "rougher" (110) face. Growth on the (111) face is monotonous while at the (110) face it is jagged. The difference between the growth modes at these surfaces can be related to the nature of their solid-melt interfaces.

Finally, we should emphasize that the observed crystallization velocities in our simulations (and in experiments on rapid crystallization following pulsed laser or electron beam radiation) coupled with the observed negligible degree of undercooling at the interface cannot be analyzed in terms of the conventional models of "continuous" growth. These models are based on equilibrium concepts, employing equilibrium properties and neglect cooperative effects. As we have demonstrated, all of the above assumptions do not hold under conditions of rapid solidification.

(*) b) Metallic Glasses and Liquid Metal Alloys

The first-order phase transition from a liquid to a crystal proceeds via nucleation processes. For certain liquids the kinetics of nucleation can become exceedingly slow and thus upon cooling such liquids at a sufficiently rapid rate they can supercool far below their melting point, and stay in that state for an extended time. When performing such a quench it is found that a

transition from a liquid to an amorphous solid (glass) occurs. At the glass transition the density, entropy and enthalpy change continuously while the compressibility, heat capacity and thermal expansion change in a sudden manner.

Metallic glasses, i.e., the amorphous solid phases formed when segregation and crystallization are avoided by ultra-rapid cooling of the liquid alloys, are the subject of much recent research effort due to their unique physical properties which suggest several possible technological applications related to their special mechanical, magnetic, electrical and chemical properties. From a pure scientific point of view these materials (and glasses in general) present an immense theoretical challenge. Although several approaches have been suggested in the last thirty years, we still lack a theoretical framework for understanding the dynamics and nature of the glass transition and glasses. In addition, calculations of physical properties of amorphous materials are complex due to the lack of translational invariance which is the anchor of most solid-state theoretical techniques. In this respect molecular dynamics simulations open a new dimension in the investigation of these complex systems and phenomena.

Most previous computer studies of metallic glasses have employed "generic" pair-potentials (such as Lennard-Jones, Morse, etc.). While these studies have contributed to our understanding they do not lend themselves to comparison with experimental results for a specific material and thus do not afford a direct critical assessment of the physical model and numerical procedure employed. Studies using more realistic potentials have based on random packing models (rpm) for the glass structure and thus cannot address questions involving the kinetics and dynamics of the glass transition itself or the dependence of metallic glass properties on thermal history, spatial fluctuations in concentration or temporal fluctuations in local density and

stress and in the underlying glass structure.

A fundamental question in relating computer simulated to laboratory prepared glasses is the short time scale of computer simulations in comparison to the experimental ones. It has been demonstrated, that, althouth the glass transition is broadened by the very rapid cooling rates used in computer simulations, it can be unambiguously observed, and the dependence of quantities such as volume and internal energy on thermal history is small and that trends may be extrapolated to experimental cooling rates. Thus, short of performing simulations employing laboratory cooling rates, an assessment of the correspondence between simulation and experimental results may be provided by simulations which employ a realistic description of the energetics for specific metallic glass systems for which extensive experimental data is available.

(*) (i) A New Molecular Dynamics Method for Metallic Systems and Studies of Liquid Metals (41)

In order to perform a realistic dynamic simulation of the formation and properties of a metallic glass we have developed a new molecular dynamics (MD) formulation for simulations of metallic systems which allows for volume and shape variations and incorporates explicitly the dependence on the density of the "volume energy" and effective pair-potentials. Therefore in this method there is no need to impose an external "electronic" pressure to achieve the correct density. The method is thus suited to simulations of processes which involve changes in temperature, pressure and/or volume such as crystal nucleation and the formation and annealing of metallic glasses. Additionally the method allows studies of realistic liquid metal systems (single and multi-component) above their melting point and in the supercooled state.

Our first application of the newly developed method was in studies of

liquid Mg, yielding good agreement with experiments for several properties including internal energy, density and structure factors at several temperatures and pressures.

In parallel with our molecular dynamics studies we have developed a method of optimized iterative solution to the Percus-Yevick equation for a liquid metal mixture.

An interest in the structure and dynamics of supercooled liquid metal mixtures and of the metallic glasses which may form from them if they are cooled quickly leads naturally to an interest in the structure of normal metallic liquid mixtures and the 'quasi-equilibrium' structure of supercooled metal mixtures, and consequently in the predictions of the theories for the structure of classical liquids, such as that due to Percus and Yevick. However, obtaining solutions to the Percus-Yevick (P-Y) integral equations by iteration, perhaps the only method applicable to arbitrary interaction potentials in mixtures, is well known to be plagued with convergence difficulties if attempted for conditions of moderately high density or low temperature. This is unfortunate, since P-Y generally gives the best agreement with experiment of the common integral equations at higher densities where strongly repulsive atomic cores are more important.

For this reason among others, most P-Y solutions are for pure species, and usually for Lennard-Jones, hard sphere, or other canonically simple interactions, where scaling to dimensionless units can make the results apply to a wider range of experimental conditions and materials.

Along the lines of the systems of immediate interest to us, Leribaux and Miller (J. Chem. Phys. 61, 3327 (1974)) have studied liquids of simple monoatomic metals, using a screened pseudopotential interaction, and have done so at liquid densities and temperatures well below the critical temperature,

employing an optimization technique to accelerate convergence of successive iterations towards a solution. Although they point out that such methods as theirs can be applied as well to other integral equations and may have value to a wide range of studies and systems, to our knowledge they have not extended their methods or calculations to liquid mixtures, which are of particular interest to us.

In this work we generalize the method of Leribaux and Miller to mixtures and obtain results for liquid Ca_2Mg for a wide range of temperatures. The method remains convergent even near the glass transition temperature of this material. Of course, convergence is not a guarantee of accuracy, especially under such unusual conditions, but it is a prerequisite.

Unfortunately, experimental information about the structure of the liquids and glasses of mixtures of simple metals is scarce, although some structure factors have been obtained for Ca_2Mg. However, we may use the new method of molecular dynamics which we have developed[41] for the purpose of studying such systems, (indeed we have applied our simulations to Ca_2Mg with good agreement with the available experimental results); thus we have a ready source of detailed structural information on this material. Furthermore, since exactly the same density dependent potentials are employed in the simulation and in the calculation, the comparison with the simulation pertains directly to the applicability of P-Y calculations to liquid mixtures both above the eutectic temperature and below it.

We find that above the eutectic, over the range of temperatures for which the liquid is the equilibrium state for the specified composition, the agreement between 'experimental' and theoretical radial distribution functions is remarkably good. Below the eutectic temperature we enter the region where the liquid is in a metastable supercooled state. As the simulated material

starts to develop structure in the pair distribution function characteristic of supercooled liquids and glasses, the P-Y solutions systematically fail to do so, although some grosser features of the distribution function are captured. This failure may illuminate some of the ways in which a supercooled liquid begins to depart in structure for a normal one as we examine the differences between the various integral equations for supercooled liquid metals.

These methods may also be applied to the structure of a liquid mixture near a potential wall to give the structure there nonperturbativity. This will be of some value in the evaluation and improvement of perturbative theories of the structure of simple liquids and liquid mixtures both near surfaces, and in bulk liquids.

(*) (ii) Molecular Dynamics of the Structure and Dynamics of a Metallic Glass (42)

In order to simulate the formation and properties of a metallic glass we have extended our molecular dynamic method to: enable studies of binary systems; enable dynamical adjustment of the potentials to instantaneous density; allow controlled cooling of the system.

We have applied the method to investigations of the metallic glass $Ca_{67}Mg_{33}$, a simple metal glass for which the static and dynamic structure factors have been measured by neutron scattering thus affording a direct comparison to experiment.

Our simulations, which are the first such realistic molecular dynamics simulation of a metallic glass yielded results in faithful agreement with the experimental data. In particular we find evidence for the existence of quasi-zone boundaries in the glass.

In addition we found that the fully dynamically relaxed glass can be characterized by several nearly degenerate local potential minima, and that

the transitions between these configurations involve large displacements by a small number of atoms. The transitions between these accessible local potential minima do not lead to an annealing or relaxation of the glass (over extended times), and the underlying topology of the configurational energy is similar to that invoked in the "tunneling level" (TLS) models of low-temperature glass behavior (though the nature of our transitions is different).

(*) 3. SMALL MATERIAL AGGREGATES (43,44)

Small material aggregates (clusters) are an finite assembly of chemical components (atoms or molecules). Depending on the chemical identity and number of components the cluster comprised of them may exhibit properties ranging from those characteristic of molecules to characteristic bulk condensed state behavior. Small clusters can be comprised of components of varied chemical identity and as single or multicomponent systems; metallic,alkali-halides, molecular, rare-gas, organic and intercomponent cluster such as rare-gas-organic and rare-gas-molecular clusters. In addition they may be produced and studied in various charge states e.g., neutral, single and multiple charged (positive or negative ions). Due to their intermediate position, bridging the molecular and condensed matter disciplines they present unique properties of applied technological interest such as in cluster heterogeneous catalysis. In addition the occurrance of clusters and their possible usage has been recognized in diverse areas such as: atmospheric science (where the role of cluster ions in both the upper and even the lower atmosphere has been suggested), combustion science, clusters as species for fuel injection into fusion reactors, aerosols and interpretation of surface bombardment experiments.

Inherent in the size dependence of cluster properties is the possibility of studying systematically the change from molecular to condensed phase behavior, nucleation phenomena, the development of surfaces, elucidation of collective effects and size effects in phase transformations, solvation and localization phenomena and the detailed mechanisms of energy transfer, flow and redistribution and dissociation in unimolecular processes.

Theoretical studies of clusters were hampered by the relatively large number of particles which renders the adaptation of molecular science

techniques rather cumbersome while the lack of translational symmetry inhibits the employment of solid-state methodology. Therefore, molecular dynamics methods which provide a numerical solution to interacting many-body systems are particularly suitable for the study of structure, dynamics and processes occurring in these systems.

We have studied two problems:

(i) Excess electron states in clusters which are of considerable interest with regard to the (nonreactive and reactive) mechanisms of electron attachment, the formation of bulk or surface states, the role of the excess electron as a problem for the interrogation of nuclear dynamics in the cluster and the quantum properties of a finite size system.

(ii) The dynamics of electronically excited clusters - the mechanisms of fragmentation and energy transfer and redistribution.

(*) (i) Electron Loccalization in Alkali-Halide Clusters (43)

We have studied the structure and energetics of an electron interacting with charged alkali-halide clusters of varying sizes. Since the electron wave-length is comparable to the cluster size, quantum phenomena are expected to be pronounced and thus the electronic degrees of freedom have to be described quantum-mechanically.

We have developed a quantum path-integral molecular dynamics method (QUPID) for the study of small clusters where the electron is treated quantum mechanically, interacting with the cluster ions which also interact between themselves and their dynamics is classical.

We have established four modes of localization of an excess electron in alkali-halide clusters:

(a) An F-center defect with the excess electron replacing an internal halide ion.

(b) A new surface state, i.e., a "surface F center" of the excess electron.

(c) Dissociative electron attachment to the cluster resulting in the formation of an "isolated" (to a large degree neutral) alkali atom.

(d) Structural isomerization induced by electron attachment.

(*)(ii) Excited Cluster Dynamics

The dynamics of electronically excited clusters is of relevance to the interpretation of time-of-flight mass spectrometry (since as we have found the excitation leads to fragmentation), studies of excimer systems, and to fundamental studies of excitation transfer and dissociation dynamics.

In our studies we have used neutral rare-gas clusters (for which the interaction potentials in both the ground and electronically excited state are often known) of varying composition, size and temperature. Thus we have studied the excitation in Ar_{13}, Ar_{55}, $Ar_{12}Xe$, $Ar_{11}Xe_2$, $Ar_{54}Xe$ and $Ar_{53}Xe_2$, (the 13 and 55 cluster systems were chosen due to their observed and calculated stablility). In the case of the Ar_n (n = 13,55) systems the excitation mechanism was modeled as follows: (a) first the cluster is equilibrated at a temperature T, (b) a ground-state configuration is chosen and the interaction potential between one of the atoms and the instantaneous nearest-neighbor to him is switched to the electronically excited-state potential of the excimer $(Ar_2)^*$. This change is accompanied by modifying the interaction between the rest of the cluster atoms and those comprising the excimer. Subsequently the dynamics of the system is followed. The simulation is then repeated for several uncorrelated initial ground-state configurations in order to obtain a statistically significant average. In the case of an $Ar_{n-1}Xe$ system the excitation resides on the Xe atom and consists of switching the potential of interaction between the excited Xe atom and the rest of the

cluster atoms.

Our main findings may be summarized as follows:

(i) In all cases (and at all temperatures) which we studied the electronic excitation results in a fragmentation of the cluster.

(ii) The fragmentation of the cluster proceeds in two stages: An impulsive (explosive) stage immediately following the excitation, whose rate is dominated by the repulsive interaction between the excited species and the other atoms and a slower stage in which the fragments continue to dissociate with a rate described by statistical unimolecular dissociation kinetics. The initial, explosive stage exhibit a very strong sensitivity to the range of repulsion and its rate may vary between 1 $psec^{-1}$ to $10\text{-}10^2$ $psec^{-1}$ by a 20% change in the repulsive range.

(iii) The dominant energy transfer from the vibrationally excited excimer (or single excited atom, in the case of $Ar_{n-1}Xe$) to the cluster occurs during the initial fast stage. The repulsion causes an "isolation" of the excited dimer (and in the case of $Ar_{n-1}Xe$, escape of the Xe^* atom) reducing its coupling, and thus further energy transfer rate.

(iv) During the initial stage the cluster effectively "melts" and fragmentation other than the initial explosive one, are essentially evaporation processes.

III. References

1. "Relaxation at Metal Surfaces: An Electrostatic Model", U. Landman, N. R. Hill and M. Mostoller, Phys. Rev. B 21, 448 (1980).

2. "Self-Consistent Linear Response at Metal Surfaces: Interionic Potentials and Formation Energy of Point Defects", R. Barnett, R. Barrera, C. L. Cleveland, and U. Landman, Notas de Fisica 5 (3), 1 (1982).

3. "Interionic Interactions Near Metallic Surfaces", R. Barnett, C. L. Cleveland, and U. Landman, Applied Surface Science 11/12, 703 (1982).

4. "Single-Ion and Pair Interaction Potentials Near Simple Metal Surfaces", R. N. Barnett, R. G. Barrera, C. L. Cleveland, and U. Landman, Phys. Rev. B 28, 1667 (1983).

5. "Multilayer Lattice Relaxation at Metal Surfaces: A Total Energy Minimization", R. N. Barnett, C. L. Cleveland, and U. Landman, Phys. Rev. B 28, 1685 (1983).

6. "Multilayer Relaxation at Metal Surfaces", R. N. Barnett, C. L. Cleveland, and U. Landman, Phys. Rev. B 27, 6534 (1983).

7. "Surface Segregation in Simple Metal Alloys in Electronic Theory", R. N. Barnett, C. L. Cleveland, and U. Landman, Phys. Rev. B 28, 6647 (1983).

8. "Multilayer Relaxation of Interlayer Registry and Spacing at High-Index Metal Surfaces", R. N. Barnett, C. L. Cleveland, and U. Landman, Phys. Rev. Letts. 51, 1359 (1983).

9. "Multilayer Relaxation at the Pb(110) Surface", J. W. M. Frenken, J. F. van der Veen, R. N. Barnett, U. Landman, and C. L. Cleveland (Surface Science, 1986).

10. "Substrate Effects on Long-Range Order and Scattering Low-Dimensional Systems", C. L. Cleveland, C. S. Brown, and U. Landman, Phys. Rev. B 22, 1784 (1980).

11. "Substrate Effects on Long-Range Order and Scattering in Low-Dimensional Systems", C. L. Cleveland, C. S. Brown, and U. Landman, in "Ordering in 2D", Ed. S. K. Sinha (North-Holland, 1980).

12. "Cluster Motion on Surfaces: A Stochastic Model", U. Landman and M. F. Shlesinger, Phys. Rev. B 16, 3389 (1977).

13. "Stochastic Evolution of Systems with Internal States", Proc. of 13th IUPAP Conference on Statistical Physics, M. F. Shlesinger and U. Landman, Annals, Israel Phys. Soc. Vol. 2, 682 (1978).

14. "Diffusion Processes in Defective Crystals and Multistate Diffusion", U. Landman and M. F. Shlesinger, Solid State Comm. 27, 939 (1978).

15. "Stochastic Theory of Multistate Diffusion in Perfect and Defective

Systems I. Mathematical Formalism", U. Landman and M. F. Shlesinger, Phys. Rev. B 19, 6207 (1979).

16. "Stochastic Theory of Multistate Diffusion in Perfect and Defective Systems II. Case Studies", U. Landman and M. F. Shlesinger, Phys. Rev. B 19, 6220 (1979).

17. "Stochastic Theory of Bimolecular Heterogeneous Surface Catalytic Reactions", U. Landman and M. F. Shlesinger, Phys. Rev. Letts. 41, 1174 (1978).

18. "Solutions of Physical Stochastic Processes via Mapping onto Ideal and Defective Random Walk Lattices", M. F. Shlesinger and U. Landman, in Stochastic Methods in the Physical Sciences, G. Adomian, ed. (Academic Press, N. Y., 1980).

19. "Transport and Diffusion Controlled Reactions on Heterogeneous Catalytic Surfaces", M. F. Shlesinger and U. Landman, in the AIP Proceedings Series, "Surface Reactions", Ed., U. Landman (1980).

20. "Conditions for a Rate-Maximizing Temperature in Heterogeneous Catalysis", M. F. Shlesinger and U. Landman, J. Catalysis 61, 270 (1980).

21. "Diffusion and Segregation at Surfaces and Interfaces", with M. Mostoller, T. Kaplan and U. Landman, Phys. Rev. B 25, 7255 (1982).

22. "Electron Scavenging in Glasses", M. F. Shlesinger, J. Chem. Phys. 70, 4813 (1979).

23. "On Energy Pathways in Surface Reactions", U. Landman and R. H. Rast, Proceedings of the 17th Jerusalem Symposium, "Dynamics on Surfaces", Eds. B. Pullman, J. Jortner, A. Nitzan and B. Gerber (D. Reidel, Boston, 1984).

24. "Theoretical Considerations of Energetics, Dynamics and Structure at Interfaces", U. Landman, R. N. Barnett, C. L. Cleveland and R. N. Rast, J. Vac. Sci. Technol. 3 (Part II), 1574 (1985).

25. "On Models of Interactive Dynamical Processes at Surfaces", U. Landman, Israel J. of Chemistry (Special Invited Issue), edited by A. Nitzan and R. B. Gerber, 22, 339 (1982).

26. "Microscopic Theory of Thermal Desorption and Dissociation Processes Catalyzed by a Solid Surface", G. S. De, U. Landman and M. Rasolt, Phys. Rev. B 21, 3256 (1980).

27. "Desorption and Dissociation on Surfaces: Modern Views", U. Landman, in the AIP Proceedings Series, "Surface Reactions", Ed. U. Landman (1980).

28. Aspects of the Kinetics and Dynamics of Surface Reactions, U. Landman (ed.), AIP, New York, N. Y. (1980).

29. "The Finite Conical Well: An Analytical Model for Hindered Rotors", J. W. Gadzuk, U. Landman, E. J. Kuster, C. L. Cleveland and R. N.

Barnett, Phys. Rev. Letts. 49, 426 (1982).

30. "Rovibrational Excitation within the Infinite Conical Well: Desorption of Diatomic Molecules", J. W. Gadzuk, U. Landman, E. J. Kuster, C. L. Cleveland and R. N. Barnett, J. Elec. Spec. 30, 103 (1983).

31. "Hindered Rotations of Adsorbed Diatomic Molecules: States and Spectra", U. Landman, G. G. Kleiman, C. L. Cleveland, E. J. Kuster, R. N. Barnett and J. W. Gadzuk, Phys. Rev. B 29, 4313 (1984).

32. "Quadrupole Interaction in the Scattering of H_2 from the Surface of LiF: Rotational Transitions", R. N. Hill, Phys. Rev. B (June 1979).

33. "A Molecular-Orbital SCF Cluster Model of H_2O Adsorption on Copper", with M. W. Ribarsky, W. D. Luedtke and U. Landman, Phys. Rev. B 32, 1430 (1985).

34. "Variational Treatment of Boundary Perturbations in Quantum Systems I", D. MacMillen and U. Landman, J. Chem. Phys. 80, 1691 (1984).

35. "Variational Treatment of Boundary Perturbations II. Shallow Surface Donor Impurities in Si and Ge", D. MacMillen and U. Landman, Phys. Rev. B 29, 4524 (1984).

36. "High Frequency Vibrational Modes at Stepped Pt(111) Surfaces", M. Mostoller and U. Landman, Phys. Rev. B 20, 1775 (1979).

37. "Epitaxial Crystallization from a Melt: A Molecular Dynamics Study", U. Landman, C. L. Cleveland and C. S. Brown, Phys. Rev. Letts. 45, 2032 (1980).

38. "Epitaxial Crystallization from a Melt", U. Landman, C. L. Cleveland and C. S. Brown, in "Ordering in 2D", Ed., S. K. Sinha (North-Holland, 1980).

39. "Molecular Dynamics of Surfaces and Epitaxial Solidification", U. Landman, C. L. Cleveland and C. S. Brown, in "Nonlinear Phenomena at Phase Transitions and Instabilities", Ed. T. Riste, (Plenum, N. Y., 1981).

40. "Molecular Dynamics of a Laser Annealing Experiment", U. Landman, C. L. Cleveland and R. N. Barnett, Phys. Rev. Letts. 49, 790 (1982).

41. "A New Molecular Dynamics Method for Metallic Systems", R. N. Barnett, C. L. Cleveland and U. Landman, Phys. Rev. Letts. 54, 1679 (1985).

42. "The Structure and Dynamics of a Metallic Glass: Molecular Dynamics Simulations", R. N. Barnett, C. L. Cleveland and U. Landman, Phys. Rev. Letts. (1985).

43. "Electron Localization in Alkali Halide Clusters", U. Landman, D. Scharf and J. Jortner, Phys. Rev. Letts. 54, 1860 (1985).

44. "Ab initio Calculation on Hydrogen-Bonded Silicon Clusters", A. C. Kenton and M. W. Ribarsky, Phys. Rev. B23, 2897 (1981).

Publications (for the 1985 report period)

1. "Theoretical Considerations of Energetics, Dynamics and Structure at Interfaces", U. Landman, R. N. Barnett, C. L. Cleveland and R. N. Rast, J. Vac. Sci. Technol. 3 (Part II), 1574 (1985).
2. "A New Molecular Dynamics Method for Metallic Systems", R. N. Barnett, C. L. Cleveland and U. Landman, Phys. Rev. Letts. 54, 1679 (1985).
3. "The Structure and Dynamics of a Metallic Glass: Molecular Dynamics Simulations", R. N. Barnett, C. L. Cleveland and U. Landman, Phys. Rev. Letts. (1985).
4. "Electron Localization in Alkali Halide Clusters", U. Landman, D. Scharf and J. Jortner, Phys. Rev. Letts. 54, 1860 (1985).
5. "The Structure, Dynamics and Spectroscopy of Non-Metallic Clusters", a review by J. Jortner, U. Landman and D. Scharf to be published in Proceedings of the Enrico Fermi Summer School (1985).
6. "Microscopic Phenomena of Macroscopic Consequences", U. Landman, an invited paper to be published in the Proceedings of the MRS Symposium on "Computer-Based Methods for the Study of Materials" (Boston, Dec. 1985).
7. "A Molecular-Orbital SCF Cluster Model of H_2O Adsorption on Copper", M. W. Ribarsky, W. D. Luedtke and U. Landman, Phys. Rev. B 32, 1430 (1985), (Rapid Communications).

Presentations (Conferences, symposia and workshops) (1985 - reporting period)

1. "A New Lagrangian Formulation for MD Simulations of Simple Metal Systems", R. N. Barnett, C. L. Cleveland and U. Landman, APS Meeting, Baltimore, March 1985.
2. "Structure and Dynamics of Alkali-Halide Microclusters", D. Scharf, U. Landman and J. Jortner, APS Meeting, Baltimore, March 1985.
3. "Path Integral Quantum MD of Electron Interaction with Alkali-Halide Microclusters", U. Landman, D. Scharf and J. Jortner, APS Meeting, Baltimore, March 1985.
4. "Molecular Orbital SCF Cluster Model of H_2O Adsorption on Copper", W. D. Luedtke, M. W. Ribarsky and U. Landman, APS Meeting, Baltimore, March 1985.
5. "The Dynamics of Interactions at Surfaces and Small Clusters", U. Landman, invited talk at the Gordon Conference on "Gas Surface Dynamics", New London, New Hampshire (August, 1985).
6. "The Vibrational Dynamics of Surface Processes", U. Landman, invited talk at the International Conference, "Vibrations at Surfaces IV", English Lake District, England, September 1985.
7. "Theoretical Aspects of Charge Transfer at Surfaces", invited talk at the "Fourth Electrochemical Study Group", Fritz-Haber Institute, Berlin, West Germany (1985).
8. "Microscopic Phenomena of Macroscopic Consequences", U. Landman, invited talk at the MRS Symposium on "Computer Based Methods", Boston, December (1985).
9. "Molecular Dynamic Simulation of a Simple Metal Glass and the Glass Transition", R. N. Barnett, C. L. Cleveland and U. Landman, invited talk at the Glass Symposium of the American Ceramic Society, May 1985.

10. "On the Structure and Dynamics of the Solid-Liquid Interface", U. Landman, invited talk at the "Frontiers in Electrochemistry" Workshop, Los Alamos, March 1985.

PHYSICAL REVIEW B VOLUME 32, NUMBER 2 15 JULY 1985

Molecular-orbital self-consistent-field cluster model of H_2O adsorption on copper

M. W. Ribarsky, W. D. Luedtke, and Uzi Landman
School of Physics, Georgia Institute of Technology, Atlanta, Georgia 30332
(Received 1 May 1985)

The interaction of H_2O with a Cu(100) surface is modeled via cluster calculations using the self-consistent-field–linear-combination-of-atomic-orbitals–$X\alpha$ method. In the equilibrium on-top configuration bonding is through the oxygen with the molecular plane tilted from the normal by 70°. Bonding involves the H_2O lone-pair orbitals and a charge donation to the metal. The calculated normal mode vibrational and low-frequency hindered molecular rotational frequencies agree with recent data.

Understanding of the bonding and structural characteristics of water interacting with metal surfaces is of importance due to the abundance of water in our surroundings and the physical and chemical processes of fundamental and technological interest which occur in such systems, such as corrosion, catalytic reactions in which H_2O is one of the reactants, electrochemical processes in aqueous solutions, and the mechanisms of adsorption and nucleation of ice on solid substrates. Recent experimental studies of water adsorption at low temperatures on single-crystal surfaces[1,2] show that for most metals H_2O monomers adsorb molecularly and tend to form hydrogen-bonded clusters, thus prohibiting studies of the fundamental interaction of H_2O monomers with the surface.

The impetus for our investigations is provided by the electron-energy-loss spectroscopy (EELS) experiments of Andersson, Nyberg, and Tengstal[2] of water adsorption on Cu(100) at low temperatures ($T \sim 10$ K) and low coverages in which evidence for H_2O monomer molecular adsorption has been found. Assignment of vibrational modes and analysis of spectral intensities allowed them to conclude that the water molecule is bonded to the metal via the oxygen with the molecular H_2O axis tilted approximately 60° away from the surface normal. Previous detailed theoretical studies of the molecular electronic structure of neutral aquametallic complexes are limited to simple metal atoms[3] (e.g., Li, Al) and most earlier studies[4] of H_2O interacting with noble and transition-metal clusters are semiempirical or qualitative in nature and do not contain optimized structural information. In this paper we investigate the electronic structure of the H_2O interaction with a Cu atom and a Cu_5 atomic cluster [designed to model localized adsorption on a Cu(100) surface] and provide new structural and dynamical information as well as an elucidation of the bonding mechanisms in these systems. In our calculations we use an extended basis set spin-unrestricted self-consistent-field–linear-combination-of-atomic-orbitals (SCF–LCAO) method with local $X\alpha$ exchange, and perform systematic optimizations with regard to the molecular internal coordinates in addition to its location and orientation with respect to the metallic cluster. The binding energies of the complexes (relative to the separated H_2O and metal) in the calculated optimized configurations are 0.76 and 0.38 eV for H_2O–Cu and H_2O–Cu_5, respectively, in accord with experimental estimates of molecular H_2O adsorption energies on metals.[1,2] Bonding occurs via coupling of the H_2O lone-pair orbitals to the metal states with an associated charge transfer to the metal of $\sim 0.15e$. As a consequence of the bonding mechanism, in the equilibrium geometry the oxygen end of the molecule points toward the metal cluster situated at a distance of 2.2 Å (2.0 Å for H_2O–Cu) with the H_2O molecular axis tilted with respect to the Cu–O bond by angles of 67° and 70° for the single Cu and Cu_5 clusters, respectively. (The molecular internal coordinates change only slightly upon adsorption.)

In the SCF-LCAO-$X\alpha$ method[5] non-muffin-tin $X\alpha$ one-electron equations are solved self-consistently using a Gaussian-type orbitals (GTO) LCAO approach. In our calculations the charge density and the exchange ($X\alpha$) potential are fitted using GTO expansions, thus circumventing four-center integrals and allowing calculations for large systems using extended basis sets.[5] We have used Wachter's[6] $(14s, 9p, 5d)$ GTO orbital basis set for Cu(^2S), augmented with diffuse p, d, and f Gaussians (exponents $=0.1$, 0.1, and 1.0 a_0^{-2}, respectively). Extensive studies by Dunlap and co-workers[7] concerning basis set dependence for transition-metal clusters have shown that exponents in this range yield adequate basis set flexibility. In the case of calculations involving the Cu_5 cluster, the Wachter's basis set is contracted[6] to $(8s, 5p, 3d)$ for the four Cu atoms farthest from the H_2O molecule. Van Duijnevelt's[8] GTO basis was used for oxygen ($9s, 6p$ augmented with diffuse p and d Gaussians) and hydrogen ($4s$ with diffuse p). The above molecular basis sets are used to derive the basis sets for the charge density and exchange fits following a procedure developed by Dunlap, Connolly, and Sabin.[5] We note that the calculations presented in this paper involve the largest basis sets ever used for a system of this size, thus providing a benchmark for future calculations.

First, we present our results pertinent to the separated species. The ground-state electronic configuration for the single-Cu atom is (Ar core, $3d^{10}4s^1$). The Cu_5 cluster is arranged with the atoms located at the vertices of a square base pyramid (see Fig. 1) with an edge length of 2.54 Å (the Cu lattice nearest-neighbor distance). The ground-state molecular-orbital configuration for the cluster was found to be $17a_1^2 11b_1^2 18e^4 5b_2^2 4a_2^2$, in agreement with previous calculations.[9] Throughout our calculation a value of 0.708 96 was used for α in the local exchange potential. While different α values would yield different total energies, extensive studies have shown[5] that structural, binding, and spectroscopic properties are essentially insensitive to moderate variations in α.

In the equilibrium configuration of H_2O, the O-H bond length is 0.968 Å [the experimental value (Ref. 10) is 0.957 Å] and the H-O-H angle is 105.3° [the experimental value

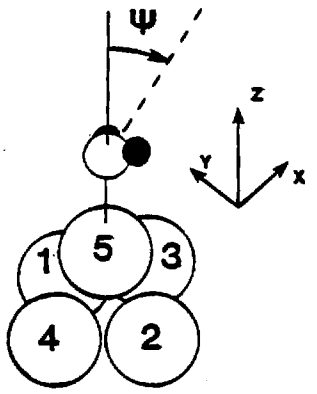

FIG. 1. Schematic picture of the H_2O–Cu_5 equilibrium configuration. Numbered open circles denote Cu atoms. The oxygen atom is represented by an open circle and the hydrogens by solid ones. The molecular H_2O plane is tilted from the Cu(5)–O axis by the angle $\psi = 70°$. The binding energy of H_2O to the Cu_5 cluster is insensitive to rotations of the molecule about the Cu(5)–O axis. In the configuration shown Cu(1) and Cu(2) are equivalent (see also Table I).

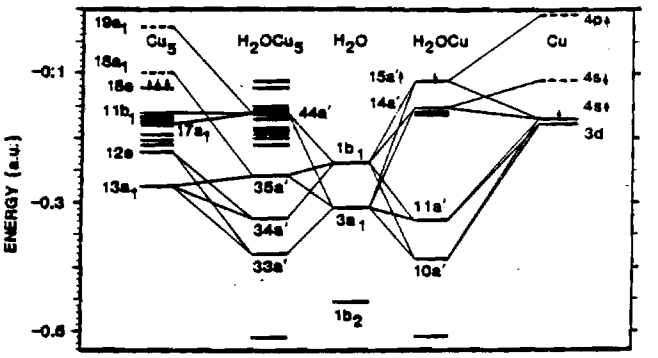

FIG. 2. Orbital-energy correlation diagrams for the equilibrium configurations of H_2O–Cu and H_2O–Cu_5 obtained via spin-unrestricted SCF-LCAO with local $X\alpha$ exchange calculations. Occupied and partially occupied levels are denoted by solid lines; broken lines denote unoccupied levels. The higher-lying states of Cu_5 are predominantly of d character (and s,p character for the top states) and are not all depicted separately.

(Ref. 10) is 104.52°] with a dipole moment of 2.02D [the experimental value (Ref. 10) is 1.88D]. The vibrational frequencies calculated from a 14-point fit to the potential surface in the vicinity of the equilibrium configuration including quadratic, cubic, and angle-bending bond-stretch cross terms are 228, 463, and 470 meV for the H-O-H bending, O-H symmetric and antisymmetric stretches, respectively, in close agreement with measured values[10] (198, 453, 466 meV, respectively).

Having outlined our results for the separated species we turn now to a discussion of comparative studies of the interaction of H_2O with a single-Cu atom and a Cu_5 atomic cluster. The ground-state binding energies determined via systematic mappings of the potential-energy surfaces are $E_B(H_2O\text{–}Cu) = 0.76$ eV and $E_B(H_2O\text{–}Cu_5) = 0.38$ eV. In the equilibrium geometry of the H_2O–Cu system, bonding to the Cu is via the oxygen located at a distance $R_{Cu\text{–}O} = 2.0$ Å, with an O-H bond length $R_{O\text{–}H} = 0.98$ Å, a H-O-H angle $\gamma = 105°$ and a Cu–O–H angle $\alpha = 103.6°$ (i.e., the molecular H_2O plane is tilted by an angle $\psi = 67°$ from the Cu–O axis). The corresponding values for the equilibrium H_2O–Cu_5 system are $R_{Cu\text{–}O} = 2.2$ Å, $R_{O\text{–}H} = 0.98$ Å, $\gamma = 106°$, and $\alpha = 100.6°$ ($\psi = 70°$). Rotations about the Cu–O axis are essentially unhindered. Note that the H_2O structural parameters are close to those of the free molecule except for a slight increase of the O-H bond length which is consistent with the charge transfer, and that the structure is modified only slightly upon increasing the cluster size.

The nature of the bonding is best described using the orbital correlation diagrams (ocd) shown in Fig. 2 deduced from analysis of the orbital coefficients and the Mulliken population analysis shown in Table I. We emphasize that the Mulliken population analysis is employed as a guide in identifying orbital admixtures, and is used in conjunction with detailed analysis of orbital composition and electron-density distributions. Note also that while a small amount of charge transfer from the Cu d-atomic states is seen in the population analysis, the molecular orbitals of predominantly d character are fully occupied in all our calculations involving Cu, in agreement with experimental and theoretical findings.[11] Both our H_2O-metal clusters are of C_S symmetry leading to classification of the molecular orbitals according to their symmetry under reflection in the plane containing the Cu–O and the molecular H-O-H axes (A'-symmetric and A''-antisymmetric representations).

An explanation of the binding mechanism of H_2O to Cu systems must invoke the participation of unoccupied and/or partially occupied orbitals, since combinations of the H_2O lone-pair orbitals (LPO's), $1b_1$ (π–LPO) and $3a_1$ (σ–LPO), with the metal fully occupied orbitals form bonding and antibonding orbitals with net zero bond order (the same argument was used in a recent study of H_2O binding to an Al cluster[12]).

First, in the case of H_2O-Cu, the unoccupied Cu ($4p$) state admixes, in the presence of the H_2O molecule, with the H_2O LPO($|L\rangle$) resulting in charge donation [in the amount given by Eq. (1)] and with the Cu($3d$) orbital resulting in p-d promotion [Eq. (2)],

$$\beta[4p,L] = \langle 4p|V|L\rangle/(\epsilon_{4p} - \epsilon_L) \ , \tag{1}$$

$$\beta[4p,3d] = \langle 4p|V|3d\rangle/(\epsilon_{4p} - \epsilon_{3d}) \ . \tag{2}$$

These effects yield energy lowerings given by (i) ΔE_L

TABLE I. Mulliken atomic populations for Cu atoms in Cu_5, H_2O–Cu_5, and H_2O–Cu.

	s	p	d	f	Total
		H_2O–Cu_5			
Cu(1)	6.706	12.348	9.945	· · ·	28.999
Cu(2)	6.706	12.348	9.945	· · ·	28.999
Cu(3)	6.811	12.259	9.955	· · ·	29.025
Cu(4)	6.873	12.237	9.933	· · ·	29.043
Cu(5)	6.552	12.508	9.957	0.062	29.079
Total	33.648	61.70	49.735	0.062	145.145
		H_2O–Cu			
Cu	7.122	12.107	9.904	0.017	29.15
		Cu_5			
Cu(1–4)	6.748	12.291	9.931	· · ·	28.97
Cu(5)	6.697	12.490	9.877	0.057	29.121
Total	33.689	61.654	49.601	0.057	145.00

$\simeq \beta^2[4p,L](\epsilon_L - \epsilon_{4p})$ and (ii) $\Delta E_{4p} \simeq \beta^2[4p,3d](\epsilon_{3d} - \epsilon_{4p})$. Similar admixtures occur for the spin-down Cu(4s) in the amounts $\beta[4s,L]$ and $\beta[4s,3d]$ and perhaps a $4s\uparrow$ to $4p\uparrow$ promotion. As seen from Table I the net effect is a transfer of $\simeq 0.15e$ from H_2O to Cu and a small amount of charge redistribution from d-type to s- and p-type Cu functions. The resulting bonding orbitals of H_2O–Cu are $10a'$ and $11a'$ (see Fig. 2) which possess large H_2O LPO components. The antibonding orbitals are $14a'$ and $15a'\uparrow$ which are of predominantly d and s character, respectively, and are anchored on the Cu atom.

The situation is more complicated, although similar in principle, in the case of H_2O–Cu_5 due to the larger number of states. The population analysis (Table I) indicates that in comparing the bare Cu_5 cluster with H_2O–Cu_5, the main changes occurring on the Cu atoms are an increase in d-type charge and a decrease in s-type charge on the fifth Cu atom [Cu(5), see Fig. 1] accompanied by an increase in s-type contributions on Cu(3) and Cu(4). This may be explained in terms of a polarization of the s-type charge on Cu(5) which results in mixing with orbitals having d character on Cu(5) and s character on Cu(3) and Cu(4). In addition in the Cu_5 cluster the d-electron population is deficient by $\sim 0.4e$ resulting in a decrease in electron-repulsion energy, thus lowering the centroid of the Cu_5 "d band" relative to the Cu $3d$ atomic level. Upon binding with H_2O the increase in d character is accompanied by an upward shift of the cluster "d band." The bonding orbitals of H_2O–Cu_5, $33a'$ and $34a'$ (Fig. 2), have predominant H_2O LPO components and involve mainly the $13a_1$ (mostly s and some p) and $12e$ (mostly d) orbitals of the Cu_5 cluster. The presence of H_2O causes charge promotion to the originally unoccupied $18a_1$ and $19a_1$ orbitals of Cu_5 from the originally fully occupied $13a_1$, $17a_1$, and $11b_1$ orbitals and a charge donation from the H_2O LPO's in the amounts $\beta[18a_1,L]$ and $\beta[19a_1,L]$. The antibonding orbital $35a'$, in which a cancellation of the large s component on Cu(5) [i.e., $s(5)$ coming from orbital $13a_1$] occurs, results from a mixture of the H_2O LPO's with the $13a_1$ and $18a_1$ orbitals of Cu_5. The increase in d character on Cu(5) is due to the admixture of the fully occupied $17a_1$ and $11b_1$ and the unoccupied $19a_1$ Cu_5 orbitals with the H_2O LPO's, yielding the antibonding orbital $44a'$. These antibonding orbitals contain predominantly Cu functions components.

Since the magnitudes of the charge transfer, proportional to β^2 [see Eqs. (1) and (2)], are similar in both H_2O–Cu and H_2O–Cu_5, the smaller binding energy found for the H_2O–Cu_5 system may be attributed to the fact that the Cu_5 unoccupied orbitals are closer in energy to the H_2O LPO's than are the single-Cu unoccupied states, thus yielding overall smaller energy lowerings [compare Eqs. (i) and (ii) in the text]. Alternatively, the electrostatic repulsion between the excess charge on Cu(5) in the Cu_5 cluster and the excess electronic charge on the oxygen will decrease the binding energy of H_2O to Cu_5.

The equilibrium orientation of the bonded H_2O molecule reflects the energy dependence on the tilt angle ψ. Variations in this angle influence the amount of admixture between the H_2O LPO's and the metal orbitals (MO). The factor $\beta[3a_1,\text{MO}]$ is large at $\psi = 0°$, and decreases while $\beta[1b_1,\text{MO}]$ increases as $\psi \to \pi/2$.

In addition we have calculated the total dipole moment of the complex in terms of the electronic and nuclear-charge distributions. The charge donation to the metal is manifested via comparison of the dipole moment for the equilibrium configuration of H_2O–Cu_5 with those of Cu_5 and H_2O obtained by separating these components of the equilibrium complex to infinity: $\mu(H_2O\text{–}Cu_5) = (1.2, 0.0, 3.2)$, $\mu(H_2O) = (2.0, 0.0, 0.65)$, $\mu(Cu_5) = (0.0, 0.0, 0.6)$ in Debye units. Associated with this value of $\mu(H_2O\text{–}Cu_5)$ is a work function change $\Delta\phi \simeq -4.8$ eV, for a surface density of 10^{15} molecules per square centimeter. The only available experimental values[1] are for hydrogen-bonded water clusters and are typically $\Delta\phi \simeq -1$ eV, indicating strong cancellation and depolarization effects.

Further insight into the equilibrium bonding configuration is obtained via analysis of the dynamics of the complex. The EELS spectrum of H_2O monomers on Cu(100) exhibits[2] losses at 28.5 and 197 meV which were assigned[2] to a hindered rotation of the molecule and the H-O-H bend of H_2O, respectively. A mapping of the potential surface near equilibrium was carried out fixing the Cu_5 coordinates and varying the H_2O internal coordinates, the O-Cu stretch in the z direction, Cu-OH bend (varying the angle α), and O-Cu-Cu bend (for the last three the H_2O internal coordinates were held fixed). A normal mode analysis shows that the internal coordinates couple weakly; the calculated modes at 30, 45, and 84 meV correspond to symmetric O-Cu-Cu bend, O-Cu stretch, and symmetric O-H stretch and the modes at 194 and 423 meV correspond to H-O-H bend and symmetric O-H stretch, respectively. Only the symmetric modes will be seen for dipole excitation in EELS. Both the calculated frequencies and assignments agree with the analysis of the observed modes.[2] It should be noted, however, that not all the calculated modes have been observed experimentally,[2] due to their low intensity (small values of the dynamic dipole moments). Our calculations do not reproduce faithfully the observed relative intensities, indicating perhaps the need for larger clusters.

It is of interest to note that the mechanism of H_2O binding to Cu clusters which we described is similar to that proposed recently for H_2O binding to a simple metal (Al) cluster.[12] Moreover, the equilibrium configuration and magnitudes of the binding energy and charge transfer are found to be similar for these two systems, suggesting common trends in the weak associative binding of molecular H_2O to metals. Finally, while convergence to the semi-infinite metal case may require clusters larger than those used by us, comparison of our results for H_2O–Cu and H_2O–Cu_5 and the agreement with experimental observations lead us to conclude that calculations employing small clusters can allow elucidation of binding mechanisms and provide quantitative estimates of physical properties in weakly bonded adsorption systems.

This work was supported by the U.S. Department of Energy under Contract No. EG-S-05-5489.

[1]K. Bange, D. E. Grider, J. K. Saas, and T. E. Madey, Surf. Sci. 136, 38 (1984), and references therein.
[2]S. Andersson, C. Nyberg, and C. G. Tengstal, Chem. Phys. Lett. 104, 306 (1984).
[3]M. Trenary, H. F. Schaefer III, and P. A. Kollman, J. Chem. Phys. 68, 4047 (1978).
[4]S. Holloway and K. H. Bennemann, Surf. Sci. 101, 327 (1980); A. B. Anderson, *ibid.* 105, 159 (1981); B. C. Khanra, Chem. Phys. Lett. 84, 107 (1981).
[5]B. J. Dunlap, J. W. D. Connolly, and J. R. Sabin, J. Chem. Phys. 71, 4993 (1979), and references therein.
[6]A. J. Wachters, J. Chem. Phys. 52, 1033 (1970).
[7]B. J. Dunlap, J. W. D. Connolly, and J. R. Sabin, J. Chem. Phys. 71, 3396 (1979); B. J. Dunlap and H. L. Yu, Chem. Phys. Lett. 73, 525 (1980).
[8]F. B. Van Duijneveldt, IBM Research Report No. RJ 945, 1971.
[9]P. S. Bagus and M. Seel, Phys. Rev. B 23, 2065 (1981).
[10]W. S. Benedict, N. Gailar, and E. K. Plyler, J. Chem. Phys. 24, 1139 (1956).
[11]J. R. Smith, J. G. Gay, and F. J. Arlinghaus, Phys. Rev. B 21, 2201 (1980).
[12]J. E. Muller and J. Harris, Phys. Rev. Lett. 53, 2443 (1984).

Theoretical considerations of energetics, dynamics, and structure at interfaces[a)]

Uzi Landman, R. N. Barnett, C. L. Cleveland, and R. H. Rast
School of Physics, Georgia Institute of Technology, Atlanta, Georgia 30332

(Received 23 October 1984; accepted 13 November 1984)

We review several of our recent studies investigating the structure and dynamics of two kinds of interfaces: solid–gas and solid–liquid types. For the former, we examine the energetics of some metal–vacuum interfaces and the dynamics of surface diffusion. Metal–vacuum interfaces are studied in the context of pseudopotential theory where the varied contributions to surface energy can be relatively easily categorized and interpreted while still providing quantitative accuracy. We examine the roles of the Madelung energy, surface dipole layer, Hartree energy, and electron response to the relaxation process. While qualitative behavior such as oscillatory multilayer relaxation can be seen even from the simplest "electrostatic" picture, quantitative predictions require both the complete theory and acknowledgment of the full three dimensionality of the system. Results are shown for the (111), (100), and (110) faces of aluminum. In exploring the dynamics of surface diffusion, we discuss a molecular dynamics (MD) simulation of model systems of lead monomers and dimers on a copper (110) surface (where there is a negligible size mismatch between dimer and substrate) and find that dimer diffusion rates can be two to three times those of the monomer. We show typical time evolutions of relevant dimer properties as well as vibrational densities of states and find that a librational or "wagging" mode of dimer motion acts as a "door-way state" for the diffusive jump and associate the elevation of the diffusion rate with its existence. We again employ MD to study solid–liquid interfaces both in equilibrium and under circumstances of rapid melting and recrystallization such as those found during laser annealing. We examine the (111), (100), and (110) faces of a fcc crystal and display profiles versus depth at various times of such properties as number density, temperature, potential energy, and diffusion constant, as well as growth rates. In particular, the close-packed (111) face enjoys a continuous growth process, uniform across the surface and mediated by an extensive interfacial region of liquid layering over the solid, while on the open, "rougher" (110) face the layering is suppressed and growth proceeds laterally across the exposed face in steps.

I. INTRODUCTION

All physical surfaces are in fact interfaces between material systems. The systems connected by the interface may possess several common physical attributes, such as chemical identity, composition, state of aggregation and structure, as in certain solid–solid or liquid–liquid interface systems, or may be of vastly different physical character as in solid–gas and solid–liquid interphase–interface systems. In addition, we distinguish between equilibrium interfaces where all components of the systems are in thermodynamic equilibrium and nonequilibrium interfaces occurring in phase transformations such as crystal growth (from the liquid or gas) or melting. In all cases, the interface region is of finite extent often possessing unique physical characteristics (crystallographical structure, electronic, vibrational and elementary excitation spectra) different from those of the systems connected through it.

Fundamental understanding of the structural and dynamic properties of interfaces is of coupled basic research and technological interest, since often the improvement of technological applications requires knowledge on a fundamental level. The unique structural and dynamical properties of interfaces influence the pathways and rates of physical and chemical processes occurring at interfaces (such as chemical catalysis, corrosion, electrochemical processes, adhesion, electronic and atomic transport, and phase transformations such as crystal growth and melting). In this paper we review recent theoretical studies, performed in our laboratory, investigating the structure and dynamics of two interface systems: solid–gas and solid–liquid types. We have chosen to focus on these systems since in addition to their different nature, exemplifying the richness of interface phenomena, the methods developed and employed in these studies demonstrate different modes of theoretical investigations of interfaces. In Sec. II the energetics underlying the crystallography of certain metal–vacuum interfaces is discussed. Energy pathways and the dynamics of surface diffusion processes are discussed in Sec. III. In Sec. IV we describe molecular dynamics studies of equilibrium crystal–liquid interfaces and of the structure and dynamical evolution of nonequilibrium crystal–liquid interfaces during phase transformations.

II. MULTILAYER STRUCTURAL RELAXATIONS AT METAL–VACUUM INTERFACES

Metal surface structural information is essential for the understanding and elucidation of a large number of surface phenomena. Consequently, major efforts have been devoted

 0734-2101/85/031574-14$01.00

in recent years to the development of surface structure experimental probes and their analysis. Progress in the formulation and implementation of theories of structurally predictive capability has been limited, hindered mainly by difficulties in carrying out a self-consistent energy minimization for the coupled system of ions and conduction electrons and the inadequacy of surface relaxation models based on pairwise interaction potentials.[1] Such theories, however, are of great importance since they can provide structural input parameters to be employed in the analysis of data and reveal the nature of the forces (and their relative contributions) which govern the atomic arrangement and in particular structural modifications (relaxation and reconstruction) which are expected (and indeed observed) at the surface region of materials. These observations have led to the formulation[1] of a simple electrostatic model which predicted, semiquantitatively, multilayer surface relaxation in both fcc and bcc materials dependent upon surface crystallographic orientation and other material parameters. The existence of multilayer relaxation phenomena has since been verified by several careful examinations of low energy electron diffraction (LEED) for several systems [e.g., Al(110),[2] Cu(110),[2,3(a)] V(100),[4(a)] Re(0$\bar{1}$01),[4(b)] Fe surfaces[5]]. In this section we review our recently developed theory[6] of lattice relaxation at simple metal surfaces which is based on a *total energy minimization*, provides *quantitative* estimates of metal surface structural parameters and elucidates the nature of forces governing the structure, multilayer relaxation in particular. We illustrate the theory by applying it to the low-index surfaces of Al.

The total energy, E_T, is expressed[6] as the sum of the ground state electron gas energy E_0, the Madelung electrostatic energy, E_M, of point ions in the presence of a semi-infinite negative neutralizing background, the interaction of point ions with the surface dipole layer, E_{DL}, and of the Hartree and band-structure contributions E_H and E_{BS}, respectively:

$$E_T\{\lambda_n\} = E_0 + E_M\{\lambda_n\} + E_{DL}\{\lambda_n\} + E_H\{\lambda_n\} + E_{BS}\{\lambda_n\} . \quad (1)$$

In our calculation we retain the explicit dependence of the total energy on the crystalline structure. In particular the last four terms depend on layer positions, $z_n^\lambda = (n - \frac{1}{2} + \lambda_n)d$, $n = 1,2,...$, where d is the layer spacing in the bulk and $\lambda_n d$ is the deviation from the truncated bulk location of layer n. E_M and E_{BS} depend in addition on intralayer structure and on interlayer registry (Δ R will denote the shift in origin of the two-dimensional lattice between adjacent layers, and is characteristic to the exposed face). The total energy is minimized with respect to λ_n, $n = 1,2,...,n_s$.

In the evaluation of the Hartree and band-structure energies we use the local form of the Heine–Abarenkov model pseudopotential:

$$V_P(R,z) = ZV_C(R,z); \quad R^2 + z^2 > r_c^2$$
$$- Ze^2u_c/r_c; \quad R^2 + z^2 < r_c^2 , \quad (2)$$

where $V_C(R,z) = -e^2(R^2 + z^2)^{-1/2}$, Z is the valence, and u_c and r_c are the pseudopotential parameters chosen[7] to fit the bulk compressibility and lattice parameter and used to determine vacancy formation energies [for Al ($r_s = 2.06a_0$) $r_c = 1.388a_0$, and $u_c = 0.3894$].

The dipole layer energy is given by

$$E_{DL}\{\lambda_n\} = Z\sum_n \int d^2R \int dz \times [\rho^e(z) - \rho^+(z)]V_C(R,z - z_n^\lambda) , \quad (3)$$

where **R** is a 2*D* vector in the surface plane. The Hartree contribution,

$$E_H\{\lambda_n\} = \sum_n \int d^2R \int dz\, \rho^e(z) \times [V_P(R, z - z_n^\lambda) - ZV_C(R,z - z_n^\lambda)] , \quad (4)$$

constitutes together with E_{DL} the first-order correction to the electron–jellium system (E_0) due to the replacement of the positive background by the ionic pseudopotentials. In Eqs. (3) and (4) the background density is denoted by $\rho^+(z) = (3/4\pi r_s^3)\theta(z)$, where $\theta(z)$ is the Heaviside step function, and the ground state electron density in the presence of $\rho^+(z)$ is $\rho^e(z)$. In our calculations, we employ the Lang and Kohn[8] electron density.

In the most primitive model (the PITB model) the system consists of point ions in the presence of a truncated bulk electron density, $E_T\{\lambda_n\} = E_0 + E_M\{\lambda_n\}$. The addition of the dipole layer and Hartree contributions (the DLH model) significantly improves the physical picture and predictive value by including a more realistic description of the inhomogeneous surface conduction electron density and its first-order interaction energy with the ions.

However, the DLH model of surface relaxation (sometimes termed the "frozen profile model") which has been used previously to predict multilayer relaxation[1] does not include the response of the electrons to the presence of the ions. As is demonstrated by our results and their comparison to experimental data, both multilayer relaxation and the full three-dimensional nature of the ionic system must be included in a proper and quantitative treatment of surface relaxation.

The band-structure energy (second order in the pseudopotentials) can be written as

$$E_{BS}\{\lambda_n\} = \frac{1}{2}\sum_{\mathbf{G}}\sum_{n,m}[\exp(i\mathbf{G}\cdot\Delta\mathbf{R})]^{n-m} \times \int dz\, \rho_n^\lambda(G;z)W_m^\lambda(G;z) , \quad (5)$$

where **G** is the reciprocal lattice vector, and $W_m^\lambda(G;z)$ is the 2*D* Fourier transform of

$$W_m^\lambda(R,z) = V_P(R,z - z_m^\lambda) - \frac{1}{N_A}\int d^2R' \times \int_{(m-1)d}^{md} dz'\rho^+(z')V_C(|\mathbf{R} - \mathbf{R}'|, z - z') , \quad (6)$$

where N_A is the number of ions in a layer. The induced (screening) electron density is linearly related to W_n^λ through

$$\rho_n^\lambda(G;z) = \int dz'\alpha_0(G;z,z')[W_n^\lambda(G;z') + \phi^\lambda(G;z')] , \quad (7a)$$

$$\phi^\lambda(G;z) = \int dz' g(G;z,z')V_C(G;z - z')\rho_n^\lambda(G;z') , \quad (7b)$$

where α_0 is the RPA polarizability and correlation and exchange are included[6] via the local field correction g. The solution of Eqs. (7) is facilitated by using the infinite barrier response model, and by the ansatz $g(G;z,z') = g(G;|z-z'|)$[6].

Including only the G = 0 contribution to E_{BS} [Eq. (5)] is equivalent to a one-dimensional treatment of the electron response obtained by averaging the ionic potential over the layers (we denote this one-dimensional electron response model of E_T by DLHBS0, to contrast with the model, denoted by DLHBS, in which the complete E_{BS} is included).

To demonstrate the method, we summarize in Table I results for the surface structures of the low-index faces of Al obtained via minimization of the total energies corresponding to the various models and those obtained by other theories, as well as values obtained from experimental analyses. Percent changes, $\Delta_{n,n+1}$, of the interlayer distance between layers n and $n+1$ from the bulk value, for differing numbers n_s of layers allowed to relax, are given. Inspection of these results and those obtained for other fcc and bcc systems[6,9] shows that relaxation is more pronounced for the open faces, and that multilayer relaxation is essential in all the models and systems considered. We find damped oscillatory relaxations with a period equal to the layer stacking period.

The principal origin of the multilayer oscillatory relaxation lies in the 3D crystallinity of the system; i.e., in the intralayer structure and the registry shift between layers, and in the relaxation between intralayer structure and interlayer spacing. Thus the less open surfaces show smaller relaxations because the ions are more densely packed within the layer, i.e., the resulting potential has less variation both parallel and perpendicular to the surface plane since the layers are neutrally charged (ions plus negative background slab), and because the layer spacing is larger. These effects of crystallinity appear in the Madelung and band structure contributions: the Madelung force between adjacent unrelaxed (100) and (110) layers ($n_R = 2$) is attractive while the force between next nearest neighbor layers is repulsive, for (111) surfaces ($n_R = 3$) the interlayer forces oscillate with a period of three layers. The Madelung contribution is larger; the band structure terms reduce (screen) the Madelung interactions, but since the electron response is affected by the presence of the surface, this screening is complicated and gives rise to forces which are not simply related to the interlayer distances.

The dipole layer and Hartree energy terms also give rise to oscillatory forces on the layers. However, these forces come from single-ion potentials, i.e., potentials which depend on the position of an individual ion with respect to the bulk, through the interaction with the jellium electron and positive background densities $\rho^0(z)$ and $\rho^+(z)$ [see also the discussion of single-ion potentials in Ref. 6(a)]. These forces, F_{DL} and F_H, are significant only for the topmost layer and, although they do oscillate due to the Friedel oscillations in $\rho^0(z)$, they approach zero rapidly as the z coordinate of the layer increases. The principle effect of the dipole layer and Hartree contributions is to limit the displacement of the first layer with respect to the bulk.

It is evident that a model in which the ions are treated as point ions (PITB) is a poor approximation, and that the second-order (band structure, E_{BS}) effects are small compared

TABLE I. Summary of the surface relaxation results for the low-index surfaces of Al obtained using the PITB, DLH, DLHBS0, and DLHBS models (see the text); available experimental results and the results of other calculations are given in the columns labeled Exp. and Other, respectively. The results are presented as the percent change from the bulk value, $\Delta_{l,l+1}$ of the spacing between the layers numbered l and $l+1$. Negative (positive) values of $\Delta_{l,l+1}$ indicate contraction (expansion) of the layer spacing. n_s is the number of layers which were allowed to relax (the results of other calculations, in the last column, are all for single-layer relaxation).

Model		PITB	DLH	DLHBS0	DLHBS	Exp.	Other
n_s				[Al(100)]			
1	Δ_{12}	−2.1	0.3	1.0	−.7		$\Delta_{12} = -7.5$
3	Δ_{12}	−2.4	0.4	1.0	0.0	$\Delta_{12} = 0$	(Ref. 12)
	Δ_{23}	0.3	0.0	0.7	−0.0	(Ref. 10)	$\Delta_{12} = -4.6$
	Δ_{34}	−0.0	−0.0	−0.1	−0.0		(Ref. 11)
n_s				[Al(100)]			
1	Δ_{12}	−11	−4	−5	−14		$\Delta_{12} = -15$
4	Δ_{12}	−26	−12	−14	−10	$\Delta_{12} = -8.4 \pm 0.8$,	(Ref. 12)
	Δ_{23}	15	8	9	4	$\Delta_{23} = 4.9 \pm 1.0$,	$\Delta_{12} = 2.0$
	Δ_{34}	−7	−4	−2	−3	$\Delta_{34} = -1.6 \pm 1.1$,	(Ref. 13)
	Δ_{45}	2	1	2	0	[Ref. (2b)]	$\Delta_{12} = -16$
							(Ref. 11)
n_s				[Al(100)]			
1	Δ_{12}	−0.4	0.8	1.9	1.8	$\Delta_{12} = .9 \pm .5$	$\Delta_{12} = 1$
3	Δ_{12}	−0.4	0.9	0.7	1.6	[Ref. (2c)]	(Ref. 12)
	Δ_{23}	0.0	−0.1	−0.1	0.1	$\Delta_{12} = 2.5$	$\Delta_{12} = -1.6$
	Δ_{34}	−0.0	0.0	0.1	0.0	(Ref. 10)	(Ref. 11)

to the first-order (Hartree, E_H) effects. However, while certain qualitative features are revealed by the electrostatic model, from the comparison of the results obtained via the various models with values extracted from experimental data [see Table I, and results obtained recently[9] for the Pb(110) surface in agreement with the analysis of ion backscattering data], we conclude that *quantitative* structural predictions require a minimization of the complete total energy expression [Eqs. (1) and (5)] which retains the full three-dimensional nature of the system, i.e., the DLHBS model. In particular, employment of the one-dimensional electron response, DLHBS0 model, does not yield adequate results.

In the above discussion we have limited ourselves to surface structural relaxations in the normal direction (i.e., variations in interlayer spacings). In investigations of the structure of high-index surfaces of fcc and bcc materials,[6(c)] we have further allowed variations in interlayer registry, with no change of the intralayer two-dimensional unit cell. The results obtained via total energy minimization, using the DLH model, predicted that the less symmetrical surfaces undergo damped multilayer oscillatory registry relaxation [which may be termed (1×1) reconstruction] in addition to multilayer oscillatory relaxation of interlayer spacings. In general, the interlayer registry relaxation shifts the first and second layers toward a more symmetric position with respect to each other; however, since the interlayer coupling extends beyond adjacent layers, this is not necessarily true for the deeper layers. Such coupled oscillatory multilayer registry and interlayer spacing relaxations have been found recently[5] in extensive LEED studies of high-index surfaces of Fe, where interesting trends as a function of "surface roughness" have been suggested.

III. ON THE DYNAMICS OF SURFACE DIFFUSION

Diffusion processes on or in the vicinity of surfaces are of importance in many surface controlled, or driven, physical and chemical phenomena. Such phenomena include crystal growth, surface phase transformations, annealing and recovery of damage, faceting, surface and interfacial (grain-boundary) segregation, and chemical processes heterogeneously catalyzed by surfaces.

The nature of current experimental probes[14] limits the temporal resolution with which diffusion processes can be studied. Valuable information about diffusion systems can be obtained via computer dynamical simulation[15–17] which enable investigations on arbitrarily short time scales and refined spatial resolution. In the following we describe our recent molecular dynamics studies[16] of surface diffusion which demonstrate the potential of such theoretical experiments in revealing the microscopic dynamical mechanisms of certain activated processes.

FIM studies of the diffusion of adatom clusters on surfaces have shown that the migration of the clusters proceeds via distinct alternating cluster configurations [most easily observed for diffusion on "channeled" substrates such as the (211) surfaces of bcc solids].[14] Motivated by these observations we have developed[18] a general stochastic theory of diffusion on ideal and defective lattices in which the diffusing system performs transitions over a manifold of internal states, which may correspond to energy levels and/or distinct spatial configurations. Proper analysis of experimental data in terms of such multistate migration mechanisms allows determination of rate coefficients (frequency factors and activation energies) for transitions among the states participating in the migration mechanism thus extending the information content which may be extracted from the data beyond the mere determination of global diffusion coefficients.

A particularly curious FIM observation concerns the diffusion of Re dimers on the (211) surface of tungsten, where the dimer rate of diffusion was found to be over a factor of 5 larger than that of single Re adatoms. The enhanced dimer diffusion was attributed[14] to an incompatibility between the equilibrium distance between the adsorbed dimer atoms and the distance between the cross-channel minima in the adsorption potential surface dictated by the geometrical structure of the substrate. As a consequence, the adsorbed dimer is never found in its natural equilibrium state and this accounts for a decrease in the energy needed to bring the system to a saddle region of the potential surface which may result in a migration event.

In our study we wish to focus on dynamical aspects of dimer diffusion and therefore have chosen the parameters of our system such as to eliminate the geometrical incompatibility. Employing generic 6–12 Lennard–Jones potentials whose parameters (σ and ϵ) were fitted[19] to materials properties we found that for a system of a lead dimer adsorbed in a cross-channeled configuration on the (110) face of copper, no such geometrical mismatch exists. In order to achieve a faithful simulation of the substrate, our simulations were performed on a thick slab consisting of 14 layers (with 70 atoms in each layer) exposing the (110) surface of the fcc copper substrate. The numerical integration of the classical equations of motion was performed using Gears' predictor–corrector algorithm with an integration time step $\Delta t = 0.0075 t_{Cu}$, where $t_{Cu} = (M_{Cu}\sigma_{Cu}{}^2/\epsilon_{Cu}) = 2.9668 \times 10^{-13}$ s (in the following reduced units expressed in terms of the Cu–Cu parameters[19] are used, i.e., distance and energy in terms of σ_{Cu} and ϵ_{Cu}, respectively).

Following equilibration we have performed extensive studies of dimer and single particle diffusion at various temperatures in which we found enhanced dimer diffusion rates (factor of 2–3) compared to the single particle diffusion rates. Since "geometrical mismatch" is absent in our system (by construction) we have set to investigate the origin of the observed enhancement (which as we will demonstrate in the following is dynamical in nature).

In Figs. 1(a)–(c), sample trajectories of the system evolution over a time span of $5\times10^4\ \Delta t$, for a cross-channel adsorbed dimer, calculated at reduced system temperature (in units of ϵ_{Cu}) $T^* = 0.2$ (corresponding to 2/7 of the substrate melting temperature), are shown. In these figures the crosses correspond to time averaged positions of the top layer substrate atoms and the dots are actual instantaneous locations of the atoms comprising the adsorbed dimer as a function of time. A plot of the Pb–Pb bond length as a function of time shown in Fig. 1(d) allows a clear identification of the jump events. We observe that at $t = 0$ the dimer started at a verti-

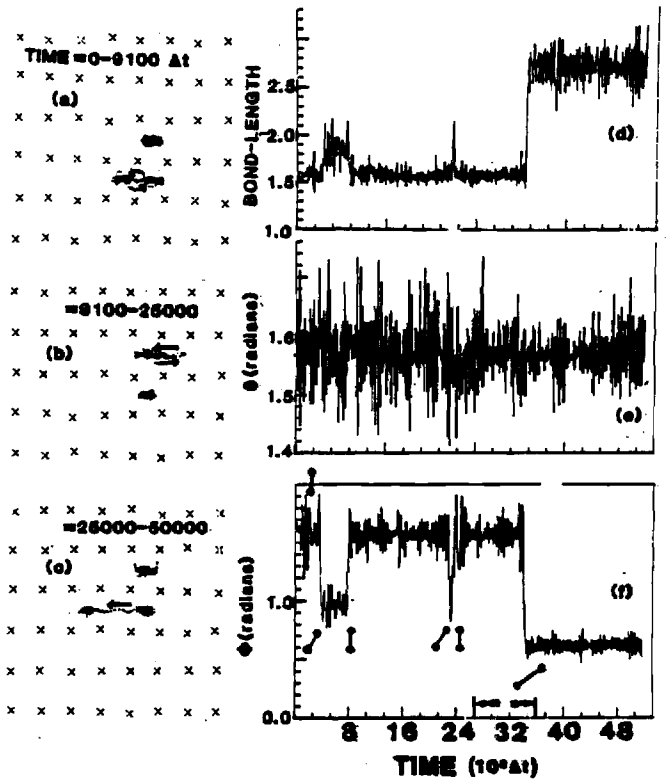

FIG. 1. (a)–(c) Sample trajectories of the system evolution over a time span of $5\times10^4\,\Delta t$, where $\Delta t = 0.0075\,t_{Cu} = 2.25\times10^{-15}$ s. Crosses indicate averaged positions of the first layer substrate atoms and dots are the instantaneous locations of the dimer atoms. The system was equilibrated with the dimer at a cross channel configuration along the Y direction. (d)–(f) Time evolution of the dimer bond length, out-of-plane angle (θ) between the dimer axis and the normal to the surface, (z) and in-plane angle (ϕ), between the dimer axis and the positive x direction, respectively. Bond length in units of σ_{Cu}. Corresponding dimer configurations are shown in (f).

cal configuration (bond length $\sim 1.5\,\sigma_{Cu}$). At $t\simeq4\times10^3\Delta t$ the bottom particle migrated to a neighboring site in the channel, returning to the original site at $t\simeq8\times10^3\Delta t$, and so on. Similar information is contained in Fig. 1(f) where the time evolution of the angle ϕ (in radians), the in-plane angle between the dimer axis and the positive x direction, along the channel, is shown, along with the corresponding dimer configurations. A plot of the angle θ, between the dimer axis and the normal to the surface, shows that the orientation of the dimer axis remained almost parallel to the surface plane throughout the course of the sample simulation [see Fig. 1(e)].

To investigate details of the migration mechanism, we focus on the time interval indicated by arrows on the time axis of Fig. 1(f), which spans the time between two jump events culminating in the migration of the bottom adparticle [see Fig. 1(c)]. A closeup view of the variation in the inplane angle ϕ with time is shown in Fig. 2(a). We observe a regular oscillatory variation about the value $\pi/2$ (with frequency $\sim1\times10^{12}\,s^{-1}$) in time. The amplitude of the dimer libration is modulated, achieving a maximum and decreasing prior to the jump event [marked by an arrow, compare Figs. 1(d) and 1(f)]. In order to interrogate further the type of motion which the dimer is engaged in we show in Fig. 2(b) the equal-time correlation of the x-components of the velocities of the dimer atoms $V_{1x}(t)V_{2x}(t)$. Librational motion in which the two particles move in opposite directions corresponds to a negative value of this correlation function, while a rocking mode in which both particles oscillate in phase yields a positive value. We note that during the increase in the ϕ-oscillation amplitude $V_{1x}V_{2x}$ (as well as $V_{1y}V_{2y}$) takes negative values, while during the decrease in ϕ prior to the jump event a reversal in sign occurs, indicating a change in the nature of the dimer mode of motion. This conclusion is corroborated by the rotational kinetic energy shown in Fig. 2(c) which exhibits a similar sequence. We note also that the same pattern occurs in the time evolution of the adparticle–adparticle bond length [Fig. 2(e)], bond potential energy [Fig. 2(f)], and bond kinetic energy [Fig. 2(g)]. These observations indicate clearly that the librational, out-of-phase motion of the dimer, upon decrease prior to the jump event, exchanged energy with a mode characterized by an in-phase motion of the dimer atoms which did not involve significant vibrations or stretch of the dimer bond. An additional clue to the nature of the prejump mode is provided by a plot of the kinetic energy of the dimer center-of-mass motion as a function of time, given in Fig. 2(h), which exhibits low values while the dimer is librating, and increases in magnitude in coincidence with the noted decrease in the librational motion. Further information concerning the dimer motion is given in Fig. 2(d) which shows the time development of the out-of-plane angle, θ. The oscillations in θ are of a much higher frequency than the in-plane ϕ librational mode and the out-of-plane velocity correlation does not show a clear pattern. In fact, the out-of-plane motion appears rather irregular, while coupled to the in-plane degrees of freedom. Inspection of the time sequences for the dimer particles kinetic energy and dimer total energy (kinetic plus inter-dimer and dimer–substrate potential energies) reveals that the energy content of the dimer increased pursuant to the excitation of the librational mode and remained so until the eventual jump event.

From the above observations we conclude that the evolution of the system leading to the reactive (jump) event is characterized by distinct, though coupled, modes which exchange energy with the substrate and among themselves. The in-phase, rocking mode, which is characterized by a high degree of center-of-mass motion, is coupled directly to the reaction-coordinate (jump event). This mode is excited by the librational mode which preceeds it, whose excitation is caused by coupling to the substrate vibrations and perhaps partially via high-frequency out-of-plane modes (and possibly dimer vibrations), which are orthogonal to the reaction coordinate. The librational mode is therefore identified as the "doorway state" for the reaction.

It is intuitively obvious and rigorously known in the theory of nonlinear oscillators and parametric modulations that the excitation dynamics in such systems depends critically on the frequencies and coupling parameters of the system.[16] To further investigate the activation dynamics and energy pathways in our systems, we calculated the density of vibrational states [Eq. (8a)] and velocity autocorrelation functions [Eq. (8b)], for our system, defined by

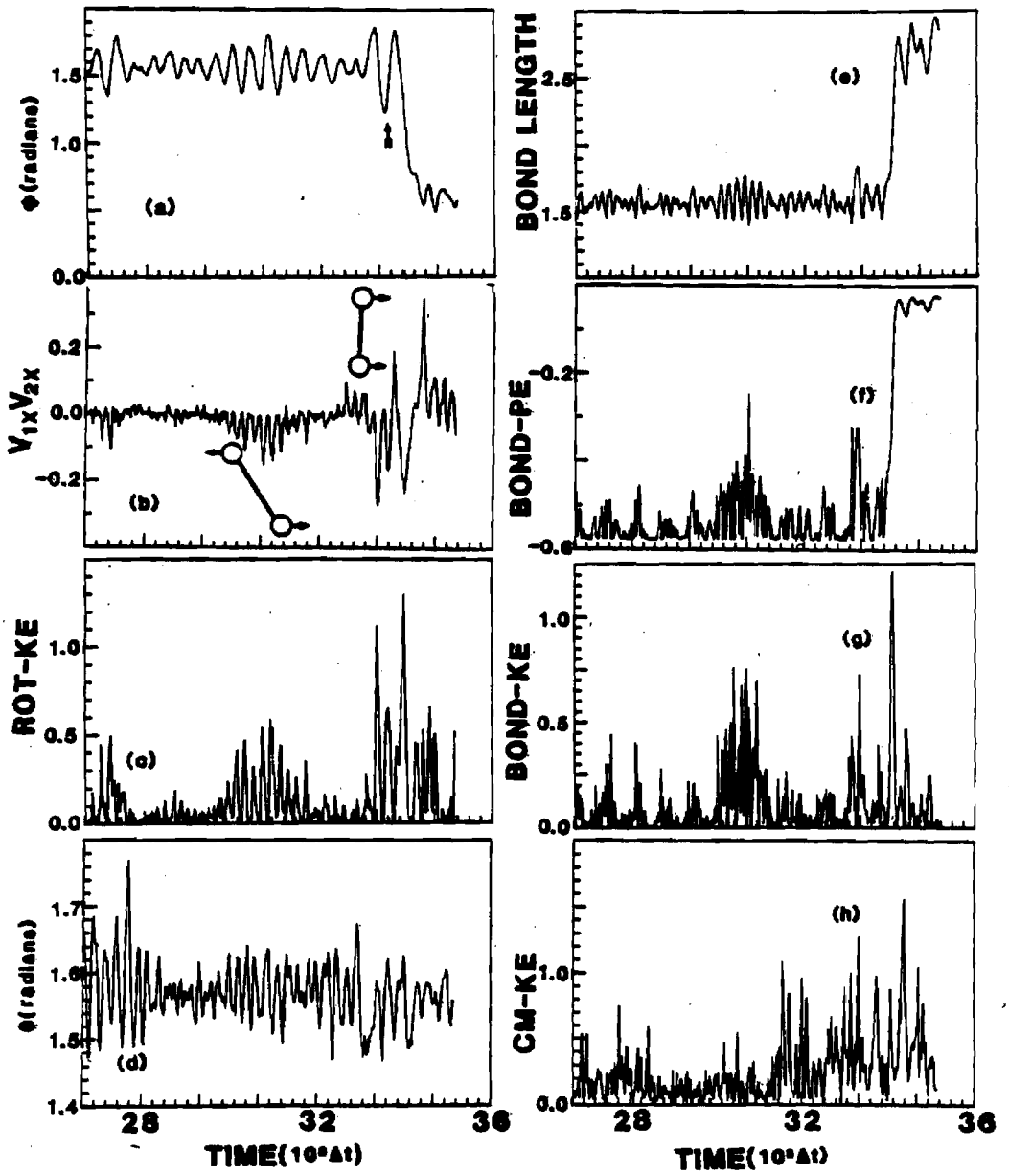

FIG. 2. Time evolution of the angles ϕ and θ [(a) and (d)], are X component of the equal time velocity correlation function $V_{1x}(t)$ $V_{2x}(t)$ in (b), dimer rotational energy (c), dimer bond length (e), bond potential and kinetic energies [(f) and (g)], and dimer center of mass kinetic energy. Energy in units of ϵ_{Cu}, and length in units of σ_{Cu}.

$$\Phi_{A\alpha}(\omega) = \int \Phi_{A\alpha}(t)\cos(\omega t)\,dt; \quad \alpha = x, y, z\,, \tag{8a}$$

$$\Phi_{A\alpha}(t) = \langle A_\alpha(0)A_\alpha(t)\rangle / \langle A_\alpha(0)A_\alpha(0)\rangle\,, \tag{8b}$$

where A is a dynamical variable, and the angular brackets denote averaging over time origins and particles (when applicable). The density of vibrational states for the x, y, and z components of the vibrations of the top-layer atoms of the substrate slab are shown in Figs. 3(a)–3(c), respectively. We observe a marked anisotropy in the vibrational spectrum, which disappears when calculated for deep layers in the slab. This emphasizes the importance of employing a sufficiently extended system in the simulations in order to faithfully represent the dynamics of the system. Components of the velocity autocorrelation functions for motions of the adsorbed dimer atoms, where data have been gathered between jump events, are shown in Figs. 3(d)–3(f). We observe that motion along the surface channel, x [Fig. 3(d)], is of lower frequency than in the normal direction, z [Fig. 3(f)]. In addition, the velocity autocorrelation in the y direction [Fig. 3(e)] is damped rapidly, indicating that motion in this direction is coupled strongly to the substrate, colliding inelastically with the substrate potential (which rises steeply). Finally the velocity autocorrelations for the rate of change of the inplane angle, ϕ, and dimer bond length, r, are shown in Figs. 3(g) and 3(h), respectively. The frequency of the bond vibrations is about double that of the angle variations. Analysis of the dimer modes of motion and their frequencies suggests that the librational mode is excited via direct coupling to the substrate phonons, and to the bond-stretch [see Figs. 3(f) and 3(h)], subsequently channeling energy to the in-phase mode which leads to the jump event. This sequence of activation and energy flow is governed by frequency resonances of the dimer modes with the substrate phonons and by anharmonic couplings. The observed enchancement of the dimer diffusion rate compared to that of single particles is dynamical in

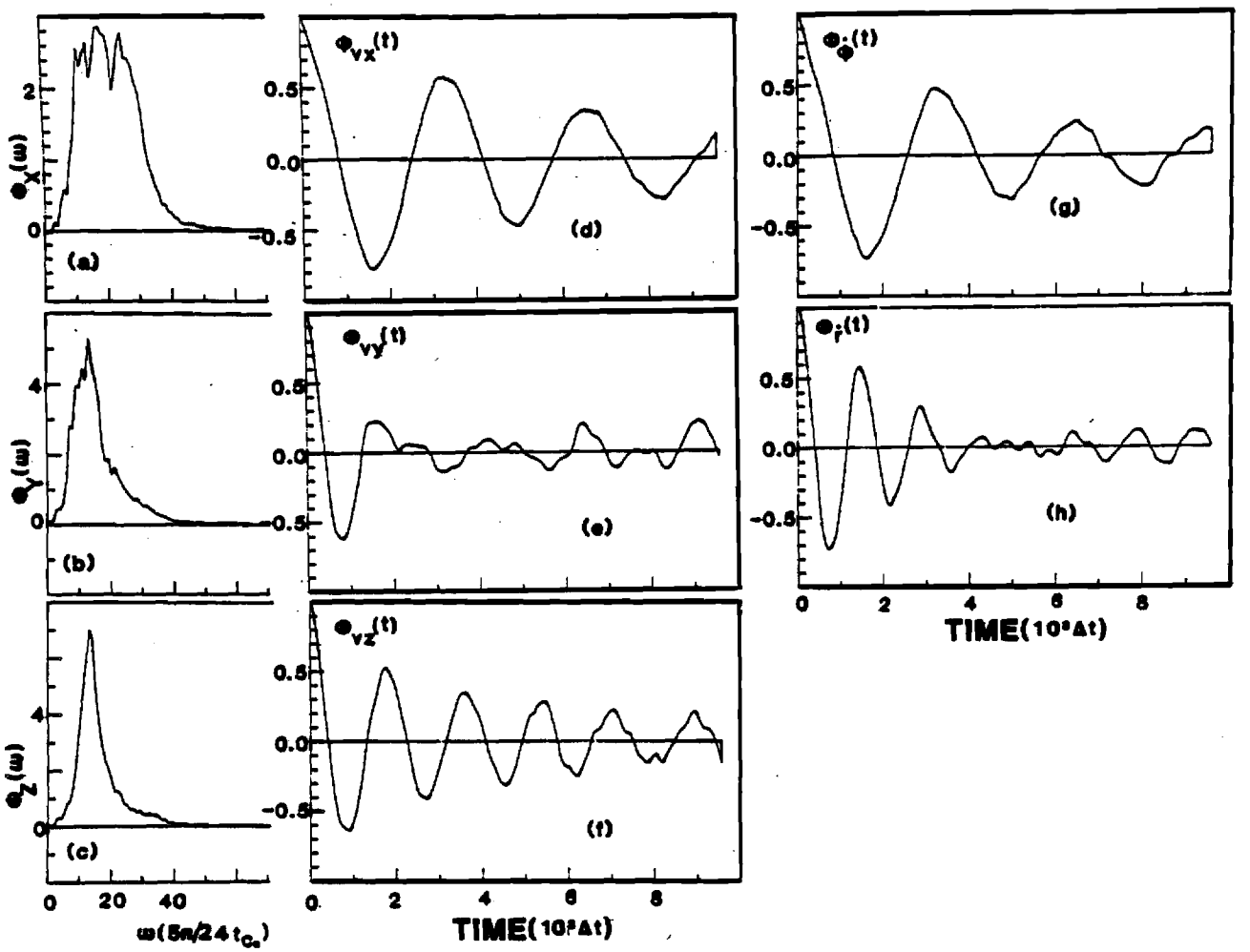

FIG. 3. (a)–(c) Cosine transforms $[\Phi_\alpha(\omega), \alpha = x, y, z]$ of the velocity autocorrelation function for first-layer substrate particles, as a function of ω expressed in units of $(5\pi/24)\ t_{Cu}^{-1} \simeq 2.2 \times 10^{12}$ s. Note anisotropy in the vibrational spectra, which disappears as one moves into the substrate slab. (d)–(f) Velocity autocorrelation functions $[\Phi_{V\alpha}(t) \equiv \langle V_\alpha(0) V_\alpha(t) \rangle / \langle V_\alpha(0) V_\alpha(0) \rangle, \alpha = x, y, z]$ of dimer particles. Data for these correlation functions and those shown in (g) and (h) was accumulated in intervals between jump events. Note the difference in frequency between the x and z modes and the fast damping of the y motion. (g) Autocorrelation function of the angular rate of change, $\Phi_\phi(t) \equiv \langle \dot{\phi}(0) \dot{\phi}(t) \rangle / \langle \dot{\phi}(0) \dot{\phi}(0) \rangle$. (h) Autocorrelation function of the dimer bond, r, rate of change, $\Phi_r(t) \equiv \langle \dot{r}(0) \dot{r}(t) \rangle / \langle \dot{r}(0) \dot{r}(0) \rangle$. Note the higher frequency variations compared to the one shown in (g).

nature, originating from the dimer additional degrees of freedom (bond stretch, libration, and rocking) which provide (resonance) channels to energy flow from the substrate.

While our focus in this study has been on surface diffusion, it is obvious that the concepts which we introduced can be applied in a straightforward manner to other activated rate processes such as desorption and dissociation and perhaps even processes involving energy dissipation such as sticking. Indeed, our present investigations supplement our earlier[20] doorway state model for thermal desorption, in which excitations of the vibrational ladders leading to bond-rupture occurs via coupling of low-frequency nonstretch modes of the adsorbate to substrate phonons. In that case the introduction of the low-frequency doorway modes was necessary due to the frequency mismatch between the frequencies of transitions between low vibrational levels of the bond-rupture stretch mode and the maximum substrate phonon frequency.[20]

IV. ON THE STRUCTURE AND DYNAMICS OF SOLID–LIQUID INTERFACES

The ultrarapid solidification which follows the irradiation of a solid with pulsed laser or electron beams, commonly known as laser annealing, is the basis for the development of novel materials growth and processing techniques and is the subject of current intensive research efforts concerned with the evolution, phase transformations, and properties of nonequilibrium materials systems.[21] Experimental studies of the microscopic mechanisms of excitation and solidification in laser annealing systems are difficult due to the fast rates of the physical processes in these systems, necessitating the development of probes of combined temporal and spatial high resolution. Theoretical progress in understanding the dynamics and kinetics of rapid solidification phenomena is equally challenging due to the highly nonequilibrium nature of these systems and the lack of adequate theoretical meth-

ods for the description and analysis of materials under such extreme conditions. Nevertheless, significant progress on both the experimental and theoretical fronts has been realized recently, brought about via the development of novel experimental probes[21] and theoretical simulation and modeling techniques (molecular dynamics,[22] solution of moving boundary coupled heat and matter transport equations,[23] and Monte Carlo studies of kinetic Ising models[24]).

The main theoretical issues encountered in studies of laser annealing systems are (a) the mechanisms of radiation (photons, particles) coupling to solids, (b) nonequilibrium thermodynamics and stability analysis (metastability, morphological stability[25]), and (c) the kinetics and dynamics of phase transformations, i.e., investigations of material processes involving changes in structure, composition, and degree of order. Solidification and melting in general are nonequilibrium phenomena governed by heat and matter transport and kinetic processes at the moving interface between two phases (solid and melt). While the above processes have their origins in particle dynamics, heat and matter transport away from the solidification interface can be described adequately using continuum methods.[23] However, treatment of transport and kinetic processes in the vicinity of the interface requires a microscopic theory, since transport properties in this region are expected to exhibit a marked spatial variation on the atomic scale and interface kinetic processes are inherently of atomistic nature.

Motivated by these considerations, we have developed and performed molecular dynamics simulations[22,26] of model laser annealing systems which allow detailed investigations of the dynamics and structure of solid–melt interfaces and studies of the microscopic mechanisms of melting and rapid solidification. Prior to the discussion of our results we outline certain of the pertinent features of the molecular dynamics simulation method.

A. Model and technique

In molecular dynamics simulations the classical equations of motion for a set of N interacting particles are numerically integrated yielding the positions and momenta (phase–space) of the particles as a function of time.[27] In simulations of bulk materials periodic boundary conditions (pbc's) are imposed thus extending the parallelopiped "calculational cell" (CC) to infinity by an integral number of translations in the three directions which determine the shape and size of the CC. In simulations of systems involving surfaces or interfaces the periodic boundary condition in the direction perpendicular to the surface plane is removed (resulting in a slab) while maintaining the two-dimensional, in-plane pbc's. In addition since the processes of melting and solidification involve changes in volume and in order to allow for possible structural transformations, we have adapted the Parrinello and Rahman[28] constant pressure molecular dynamics by restricting the boundary conditions and dynamical variation to the vectors **a** and **b** defining the basis of the MD calculational cell thus allowing dynamical variations in areal shape and density, along with free dynamical variation in the direction normal to the surface plane.

The slab configuration is useful in studies of thin film systems. However the phenomena investigated by us in this paper involve systems which are semi-infinite, i.e., while our interest is in processes occurring at the surface region, the physical system is of macroscopic extent in the direction normal to the surface. Consequently, we couple the slab to a substrate of the same crystalline structure and composition. The particles of the substrate are static, exerting forces on the dynamic slab particles (within the interaction range of the potential). To assure that the dynamics is followed faithfully for most of the system and in particular in the vicinity of the interface region of interest, slabs of sufficient thickness are employed in the simulation (typically 30–40 atomic layers for the case of interaction potentials whose range of interaction extends over distances of 2–3 layer spacings thus introducing only a negligible perturbation due to the static nature of the substrate). Geometrical data of the systems which we studied is given in Table II. The numbers of dynamical atoms were chosen such that the areas and thicknesses of the systems, exposing the (111), (100), and (110) low-index surfaces of fcc crystals, are as close as possible, thus affording comparative studies.

Since the bulk of the system serves as a thermodynamic reservoir, and since our dynamic slabs are of thickness which assures proper dynamics in the regions of interest, we treat the two slab layers which are most directly influenced by the forces due to the static substrate as a thermal coupling region. Heat exchange with the constant temperature reservoir (T_R) is achieved via extraction of kinetic energy from the slab through scaling of velocities of the particles in the two-layer coupling region. The scaling factor is determined at each integration time step according to the heat conduction equation

$$\frac{dQ}{dt} = K(T(t))A(t)\frac{dT(z,t)}{dz}, \tag{9}$$

where Q is the rate of heat flow, $A(t)$ is the area of the simula-

TABLE II. Geometrical data used in the simulation of the three low-index fcc crystals; a is the length of the cubic unit cell edge.

Property	(111)	(100)	(110)
Dynamic atoms	1512 (27 layers)	1500 (30 layers)	1505 (43 layers)
Static atoms	168 (3 layers)	150 (3 layers)	175 (5 layers)
Layer area	$24.25a^2$	$25a^2$	$24.75a^2$
Layer spacing	$a/\sqrt{3}$	$a/2$	$a/2\sqrt{2}$
Atoms/layer	56	50	35
Dynamic slab dimension	$15.588a$	$15a$	$15.20a$

tion cell, $K(T(t))$ is the temperature dependent thermal conductivity of the material, and $dT(z,t)/dz$ is the thermal gradient (the explicit time dependence of these quantities is denoted). For our choice of substrate material (6–12 Lennard-Jones potential with parameters corresponding to Ar), the experimental[29] $K(T)$ is used in the simulation. The temperature gradient is obtained by via a linear interpolation between the temperature in the coupling region (determined at each time step by averaging the kinetic energies of particles in that region) and the temperature T_R at a fixed point in the reservoir located at a distance of $20a$ from the coupling region (a is the dimension of the conventional unit cell for our bulk fcc system). This model allows studies of the influence of substrate temperature and/or composition on the melting and solidification processes since different substrate materials or temperatures yield different gradients.

The coupling of the incident radiation pulse to the system is simulated via a time-stepwise scaling of particle velocities applied to the free end of the system, has a triangular intensity-versus-time profile, is of 1.6 ps in duration and carries a total energy of 6.3×10^{-5} J/cm^2. In applying the pulse, an absorption profile given by $\exp[0.02\,z/(1\text{ Å})]$ is used where z (in angstroms) increases in the direction going out from the solid.

In all our studies the material systems consist of two species, 90 at.% of host species α and 10% of initially random substitutionally distributed impurities β. These particles interact via pairwise 6–12 Lennard-Jones potentials:

$$\Phi_{\alpha\beta}(r)=4\epsilon_{\alpha\beta}\left[\left(\frac{\sigma_{\alpha\beta}}{r}\right)^{12}-\left(\frac{\sigma_{\alpha\beta}}{r}\right)^{6}\right], \tag{10}$$

where r is the distance between the particles, $\sigma_{\alpha\beta}=(\sigma_\alpha+\sigma_\beta)/2$ and $\epsilon_{\alpha\beta}=(\epsilon_{\alpha\alpha}\epsilon_{\beta\beta})^{1/2}$. $\epsilon_{\alpha\beta}$ is the well depth at the equilibrium separation which occurs at $2^{1/6}\sigma_{\alpha\beta}$ (thus the interacting species are characterized in terms of their mass, $m_{\alpha(\beta)}$, their binding energy, and their atomic size), systematic studies of dependencies of the properties of the system upon host and impurity atomic sizes, masses, and binding strengths can be performed by selecting the values of the above potential parameters.

In presenting our results we often used reduced temperature, energy, and time units defined as follows: $T^*=k_B\,T/\epsilon_{\alpha\alpha}$. Energy is expressed in $\epsilon_{\alpha\alpha}$ units and $t^*=(\sigma_{\alpha\alpha}^2\,m_\alpha/\epsilon_{\alpha\alpha})$, respectively. For a host α, with Argon LJ parameters ($\sigma_{\alpha\alpha}=3.4$ Å, $\epsilon_{\alpha\alpha}=120$ K and $m_\alpha=40$ amu), $t^*=2.16$ ps. The classical equations of motion are integrated using the Gear predictor–corrector method with a time step $\Delta t^*=0.0075t^*$.

B. Analysis

Integration of the equations of motion yields the phase–space trajectories for the system from which physical properties and their time evolution can be obtained. To facilitate the presentation of our results, we define for any property g_i which depends on the phase–space point $(\mathbf{r}_i,\mathbf{v}_i)$ of atom i located at z_i (with $z=0$ set at the bottom of the slab and increasing toward the surface) a local density (per unit length) of that property at z by

$$\hat{\rho}_g(z)=\frac{1}{\sqrt{2\pi}s}\sum_i g_i\exp[-(z-z_i)^2/2s^2]\,. \tag{11}$$

In our calculations a value of 0.126 of the average layer spacing was used for the width parameter s. This allows us to exhibit our results as continuous profiles in the z direction.

We analyze our results in terms of the following quantities:

(1) The particle number density (per length) profiles, $\rho(z)$, are obtained by letting $g_i=1$ in Eq. (11). All other properties are presented as per particle local densities

$$\rho_g(z)=\hat{\rho}_g(z)/\rho(z)\,. \tag{12}$$

(2) Kinetic energy profiles, KE(z), obtained by setting $g_i=\frac{1}{2}m_i v_i^2$ in Eq. (11). The temperature is related to KE(z) by $T(z)=(\frac{2}{3})\mathrm{KE}(z)$.

(3) Potential energy profiles, PE(z), obtained by setting $g_i=\frac{1}{2}\sum_{j\neq i}\Phi(|r_i-r_j|)$ in Eq. (11).

(4) Planar orientational order parameter profiles $[O_n(z)]$ defined by substituting in Eq. (11):

$$g_m^{(n)}=\frac{1}{W_m}\sum_{j\in nn(m)}W_{mk}\exp(in\theta_{mj})\,, \tag{13a}$$

where

$$W_m=\sum_{j\in nn(m)}W_{mj} \tag{13b}$$

and

$$W_{mj}=\exp[(z_i-z_m)^2/2\sigma_0^2]\,. \tag{13c}$$

In Eqs. (13a)–(13c), $nn(m)$ denotes nearest neighbors to atom m, θ_{mj} is the angle that the "bond" between particles m and j makes with the x axis (in the plane), n is an integer, and the width σ_0 is chosen to be one-half the interlayer spacing for the material. In the figures showing our results, the magnitude of the complex quantity $O_n(z)$ is given. The order parameter $O_n(z)$ measures the degree of particle planar order in an atomic layer which when in the crystalline state possesses n-fold symmetry, i.e., for a perfect fcc crystal at $T=0$ K, $O_4=1$ for the (100) planes and $O_6=1$ for the (111) planes. For the (110) planes, $0_4=1$ after a scaling of the rectangular two-dimensional unit cell which converts it into a square. From our experience, discernable crystalline order in a layer is associated with $O_n\gtrsim0.4$ (see Fig. 4). Values of $O_4<0.4$ indicate a disordered, liquidlike state.

(5) Diffusion constant profiles ($D(z)$), obtained via the time-velocity autocorrelation function. Here g_i in Eq. (11) is taken as

$$g_i=\int_0^\infty dt\,[\mathbf{v}_i(t)\mathbf{v}_i(0)]\,. \tag{14}$$

Diffusion constant profiles in the normal direction and lateral diffusion constants parallel to the surface plane are evaluated by a proper choice of the velocity components in Eq. (14).

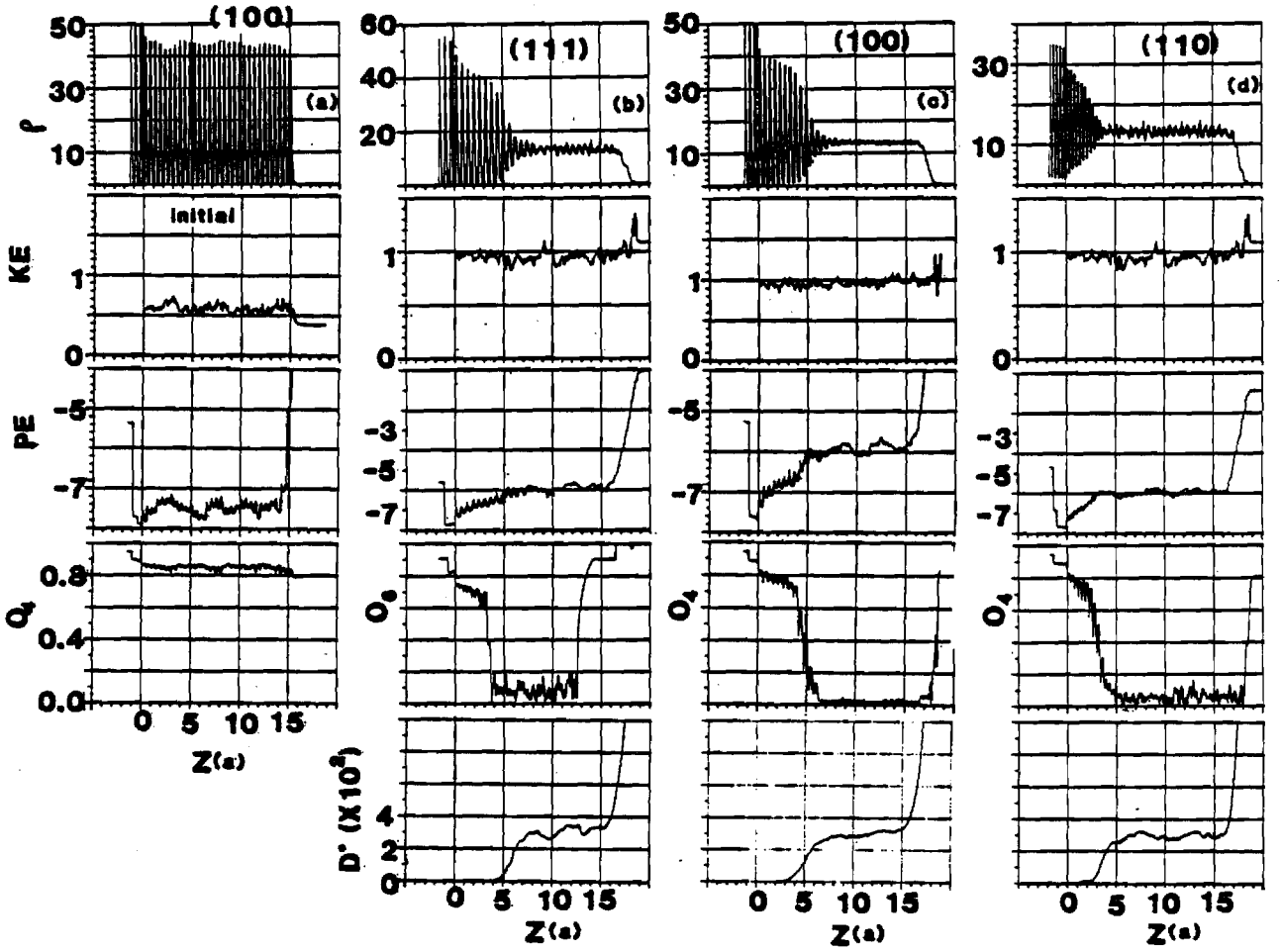

FIG. 4. Number density (ρ), kinetic energy (KE), potential energy (PE), planar orientational order parameter (O_4) and diffusion (D) profiles vs distance Z (in units of a, the cubic unit cell edge length of the bulk crystal, at a reduced temperature $T^* = 0.4$ and zero pressure; at these conditions $a = 5.4$ Å). (a) Profiles for the initial equilibrated (100) system consisting of 90% host particles and 10% random substitutionally distributed impurities (the LJ potential parameters chosen to correspond to Ar as the host and Kr as the impurity). (b)–(d) Profiles of the equilibrium solid–melt coexistence systems, for the three low-index faces of the crystal.

C. Equilibrium solid–melt interfaces

The initial state in all our simulations is an equilibrated fcc crystalline sample composed of 90% host particle with 10% substitutional randomly distributed impurities, at a reduced temperature $T^* = 0.4$, and zero external pressure. We choose

$$\sigma_{\beta\beta}/\sigma_{\alpha\alpha} = 1.07, \quad \epsilon_{\beta\beta}/\epsilon_{\alpha\alpha} = 1.387$$

and

$$m_\beta/m_\alpha = 2.098,$$

i.e., a heavier, slightly larger and stronger binding impurity. The three systems which we study differ by the crystal face exposed at the surface (see Table II). Particle number density, kinetic energy, potential energy, and orientational order parameter profiles for the initial state of the (100) systems are shown in Fig. 4(a). The system exhibits sharp atomic layers [$\rho(z)$] with a high degree of inplane crystalline order ($O_4 \simeq 0.8$). Note the variations in the potential energy profile which attains local minima at values of the normal coordinate z corresponding to atomic layers positions.

Having obtained an equilibrated sample a heating pulse is impinged on the surface. The energy thus deposited into the solid serves to disorder and eventually melt a region whose extent depends upon the energy in the pulse and the materials absorption length. Prior to investigations of the resolidification processes, we study properties of the equilibrium solid–melt coexistence systems which are obtained by turning off heat flow to the substrate reservoir during and after the application of the radiation pulse. The system is then allowed to evolve for an extended period of time, achieving the equilibrium state. The equilibrium profiles for the (111), (100), and (110) systems are shown in Figs. 4(b), (c), and (d), respectively. These profiles have been obtained as time averages of the corresponding quantities in the equilibrium state. To simplify comparisons between the results for the three surface systems, distance for all of them is measured in units of a, the cubic unit cell dimension of the bulk crystal at $T^* = 0.4$ ($a = 5.4$ Å).

As seen from these figures, the energy deposited by the pulse melted over half of the samples, producing equilibrium, two-phase, solid–melt coexistence systems. The kinetic energy profiles, KE, shown in Figs. 4(b), (c), and (d), demonstrate the establishment of uniform temperature distributions in the equilibrated systems. The equilibrium (coexistence) temperature corresponding to the average kinetic

energy shown in Fig. 4(b), (c), and (d) is $\simeq 0.95T_m$ where T_m is the melting temperature of the pure host system (the slight depression of the melting point is due to the 10% impurities in our systems), at the same conditions. The differences between the solid and melt regions are evident from inspection of the particle number density, potential energy, orientational order, and diffusion constant profiles. Note the distinct, sharp density variations in the ordered solid regions associated with distinct minima in the potential energies and high values of the planar orientational order, in contrast to the behavior and values of these quantities in the melt region.

The solid and melt regions differ also in their dynamical and transport properties as demonstrated by the diffusion profiles shown in Figs. 4(b), (c), and (d). Furthermore, the diffusion profiles exhibit a monotonous, continuous variation over a distance of $\sim 4a$ between the value for the bulk solid ($D = 0$) and that for the bulk of the melt ($D \simeq 0.03$ in reduced units, or 5.37×10^{-4} cm^2/s for Ar potential parameters, which is close to previously determined values[30] using a 6–12 LJ potential and the experimental value (0.033) for liquid argon at the triple point[31]). Anticipating the importance of the solid–melt interface to the nonequilibrium growth dynamics of a crystal in contact with its melt (see Sec. IV D) we focus in the following on the properties of the equilibrium crystal–melt interfaces.

The structure and dynamics of crystal–liquid interface systems have been the subject of increasing theoretical (as well as experimental) interest. Theoretical methods of treating the equilibrium thermodynamics of interfaces in general were introduced by Gibbs in 1878,[32] and much of this seminal work still forms the conceptual framework for research in this field. Most studies aimed towards the development of a molecular theory of equilibrium interfaces are phenomenological in nature. The main difficulty in developing a microscopic theory of the solid–liquid interface (and other liquid interfaces) arises from the presence of the liquid. A satisfactory theory has not yet been developed for the description of homogeneous liquids, although significant progress in this direction has been made, particularly through the advent of numerical simulation methods.[27] The problem of a solid–liquid interface is further complicated since the structural and dynamical properties of the liquid are perturbed by the presence of the solid. The three main theoretical approaches which were developed and applied in investigations of solid–liquid interfaces are: (1) The model approaches[33] which follow and extend the original work by Bernal[34(a)] of the structure of bulk liquids [applied to fcc (111) and hcp (0001) interfaces]. (2) Statistical mechanics theories which employ the liquid-state integral equation methodology in juxtaposition with perturbation theory[35] [applied to fcc (100) and (111) interfaces]. (3) Monte Carlo and molecular dynamics simulation methods[36] [applied to fcc (100) and (111) interfaces]. All three treatments result in a diffuse, layer structured in the liquid, interface. However, the model approaches yield a density deficit at the immediate vicinity of the crystalline surface[33] which is not observed in molecular dynamics simulations. This discrepancy is due partly to the static nature of the crystalline surface in the hard sphere models.

While all the three low-index fcc crystal–liquid interface systems studied by us exhibit a diffuse, layer-structured interfaces [see Figs. 4(b), (c), and (d)], subtle differences due to crystalline face anisotropy should be noted. Due to the diffuse continuous nature of the interface it is difficult to delineate clearly the demarkation separating the solid phase from the melt. We may use the diffusion profiles to guide us in drawing that distinction. It should be noted however that even a moderately defective crystal may exhibit a non-negligible rate of diffusion. In any case, adopting the above criterion it appears that the extent of the diffuse interface is largest for the (100) interface, decreasing slightly for the (111) interface and further decreasing for the (110) interface. Further information is provided by the orientational order-parameter profiles [see Figs. 4(b), (c), and (d)] and via inspection of the corresponding projections of particle coordinates onto the xy surface plane. Upon analysis we find that for the (100) interface intralayer order is changing across the interface transition layer in a gradual manner, as compared to the more abrupt changes occurring for the (111) and (110) interfaces. Note that while the (100) surface possesses fourfold intralayer symmetry, and the (110) can be analyzed using O_4 following the scaling of the two-dimensional unit cell mentioned in Sec. IV B, intralayer order in the (111) crystalline layers is characterized by a sixfold symmetry, O_6, which is a more prevalent packing symmetry in the liquid than the fourfold symmetry. Therefore, the sharp drop in O_6 in Fig. 4(a) is somewhat deceptive.

The crystalline anisotropy of the transition interface region is further demonstrated via the different manners in which the particle densities and interlayer spacings vary across that region for the (111) and (100) interfaces.[37] Analysis of the particle density profiles in Figs. 4(b) and (c) shows that for the (111) system the interlayer spacing remains constant throughout the transition region, equaling roughly that of the crystalline interlayer spacing. The density decrease is achieved for this surface by reducing the number of particles in successive layers. At the (100) interface the interlayer spacing in the transition layer increases gradually from the crystalline value while the number of particles per layer remains constant. These differences between the two interfaces reflect the larger dissimilarity between the bulk liquid structure and the local arrangement in the interfacial liquid layer at the (100) surface, than between the structures of the bulk liquid and interfacial liquid at the (111) surface. At the (100) surface the induced local structure in the liquid in the vicinity of the crystal is octahedral while hard-sphere packing near a flat plane exhibits a nearly perfect two-dimensional hexagonal[34(b)] structure which upon approaching the three-dimensional liquid bulk turns into a polytetrahedral structure of pentagonal symmetry. At the (111) surface the symmetry of the crystalline potential matches closely that of a liquid in contact with a flat wall. The oscillatory behavior of the density profile in the transition region of the (111) interface is then due to the transition between the two-dimensional symmetry of the packing at the immediate vicinity of the crystalline surface and that which occurs in the three-dimensional spherically symmetric bulk liquid.[35]

Finally, we remark upon the similarity in the values of the

diffusion constants at the interface regions for the three interfaces studied. Also, we have not found significant differences between the diffusion constants of the interfacial liquid layers in the two lateral directions [although, in the case of the (110) system there seems to be a slight enhancement of the diffusion in the x direction, i.e., along the channels, but this occurs in a region which possesses crystalline, though imperfect, character]. Additionally, we have not found significant differences between the diffusion coefficients at the solid–liquid interface in the lateral and normal to the surface directions. This behavior differs from that which we have found at the liquid–vapor interface and also found recently in molecular dynamics simulations of crystal–vapor interfaces[38] where although no in-plane diffusion anisotropy is observed, the lateral diffusion rate in the topmost liquid layer is significantly larger than the vertical diffusion rate (diffusion in deeper layers is found to be independent of direction), thus demonstrating the difference in particle transport properties at these interfaces.

D. On nonequilibrium crystal–melt interfaces: Melting and rapid solidification

Our initial state is, as before, an equilibrated fcc crystalline sytem exposing one of the low-index faces [see Fig. 4(a) for the (100) case], composed of 90% host particles with 10% substitutional randomly distributed heavier, larger, and stronger binding impurities, at a reduced temperature $T^* = 0.4$ and zero external pressure. The system is then subjected to the influence of a heat pulse of 1.6 ps in duration as described in Sec. IV A, allowing for heat conduction to the substrate reservoir [see Eq. (9)]. A sequence of snapshots of the (100) system evolution at selected times after the end of the heat pulse is shown in Fig. 5. In this figure we show in addition to the number density profiles, the corresponding kinetic energy ($1.5T^*$), potential energy, and planar orientational-order profiles. As seen in Fig. 5(a) 2 ps after the termination of the pulse, the kinetic energy (temperature) of the system is increased and disordering has just started to occur as evident from the PE and O_4 profiles. While the sample is above the melting temperature, not enough time has yet elapsed for significant particle displacements, and for conversion of thermal (kinetic) energy to potential energy. As time progresses the system continues to disorder and melt, with the melting front moving into the interior (to the left in the above figures). Characteristics of the system at the final stages of melting are shown in Fig. 5(b) (25 ps) where about one-half the extent of the system has melted. We notice that the temperature of the melt in the region closer to the vapor side is still well above the melting temperature and that the volume of the system has expanded significantly. In addition, a well-developed diffuse, layer-structured in the melt, crystal–melt interface is observed. At about this time melting stops and resolidification begins, with the solid–melt interface starting to move to the right. As seen in Fig. 5(c), (73 ps) and in subsequent times [Figs. 5(d)–(f)], crystallization started and proceeds while the kinetic temperature of the melt is still above the solid–liquid coexistence temperature. We did not observe any significant degree of supercooling near or at the crystallization front throughout the whole evolution of the system. The moving crystallization front is characterized again by a layer-structured in the melt diffuse interface, possessing density, structural, dynamic and transport properties intermediate between the bulk solid and melt phases connected through it. The final product for all the systems presented in this study is a perfect crystal with a random substitutional impurity distribution.

From the above observations we conclude that the relaxation times which govern the rate at which the layer-structured diffuse solid–melt interface is established under nonequilibrium conditions are extremely short (occurring both during melting and resolidification). The anisotropic "liquid layering," which establishes the material density in the melt region preceding the solidification front, "prepares" the melt for the subsequent evolution of planar crystalline ordering. The unique structural and transport properties of the diffuse solid–melt interface may play an important role in the crystallization kinetics and affect the degree of crystalline perfection and impurity distribution in the resolidified material. We conjecture, that under conditions where the solidification front would be able to advance with a velocity which supercedes that which is necessary for the reorganization of the melt to form the anisotropically structured diffuse interface, a defective, perhaps amorphous, resolidified material would be obtained.

The z location of the recrystallization interface z_i vs time for the three systems is shown in Figs. 6(a)–(c) (this location was determined from analysis of the planar orientational order parameters and analysis of particle trajectories). The crystallization velocities deduced from this data are $v = 7.7$, 10.0, and 8.4 m/s for the (111), (100), and (110) systems, respectively.

Crystal growth from the melt is often discussed in terms of the following mechanisms[40]: (1) Two-dimensional nucleation, where upon nucleation of small monolayer "islands" growth proceeds by further attachment of atoms to the "islands" and spreading of these monolayers across the surface. According to this mechanism the growth rate will be negligibly small for small undercoolings.[40] (2) "Continuous" or "normal" growth,[41] where it is assumed that all atoms arriving at the surface of the solid substrate are able to stick to become solid (thus nucleation is not a necessary kinetic step). According to this mechanism the rate of growth increases with the degree of undercooling, becoming proportional to it for small undercoolings.

Attempts at unifying the two growth modes have been proposed.[42,43] In particular, the model introduced by Cahn assumes that the free energy of the interface is a periodic function of its mean position relative to the lattice periodicity of the solid phase. Thus this model contains the idea of a diffuse (perhaps structured) solid–melt interface.

The two-dimensional nucleation mechanism is expected to be dominant for atomically smooth interfaces while continuous growth is expected to occur on rough surfaces. The plots of the crystalline interface position as a function of time shown in Figs. 6(a)–(c) exhibit different characteristic behavior as we go from the atomically smooth (111) face to the "rougher" (110) face. As seen from these figures, growth on the (111) face is monotonous while at the (110) face it is jag-

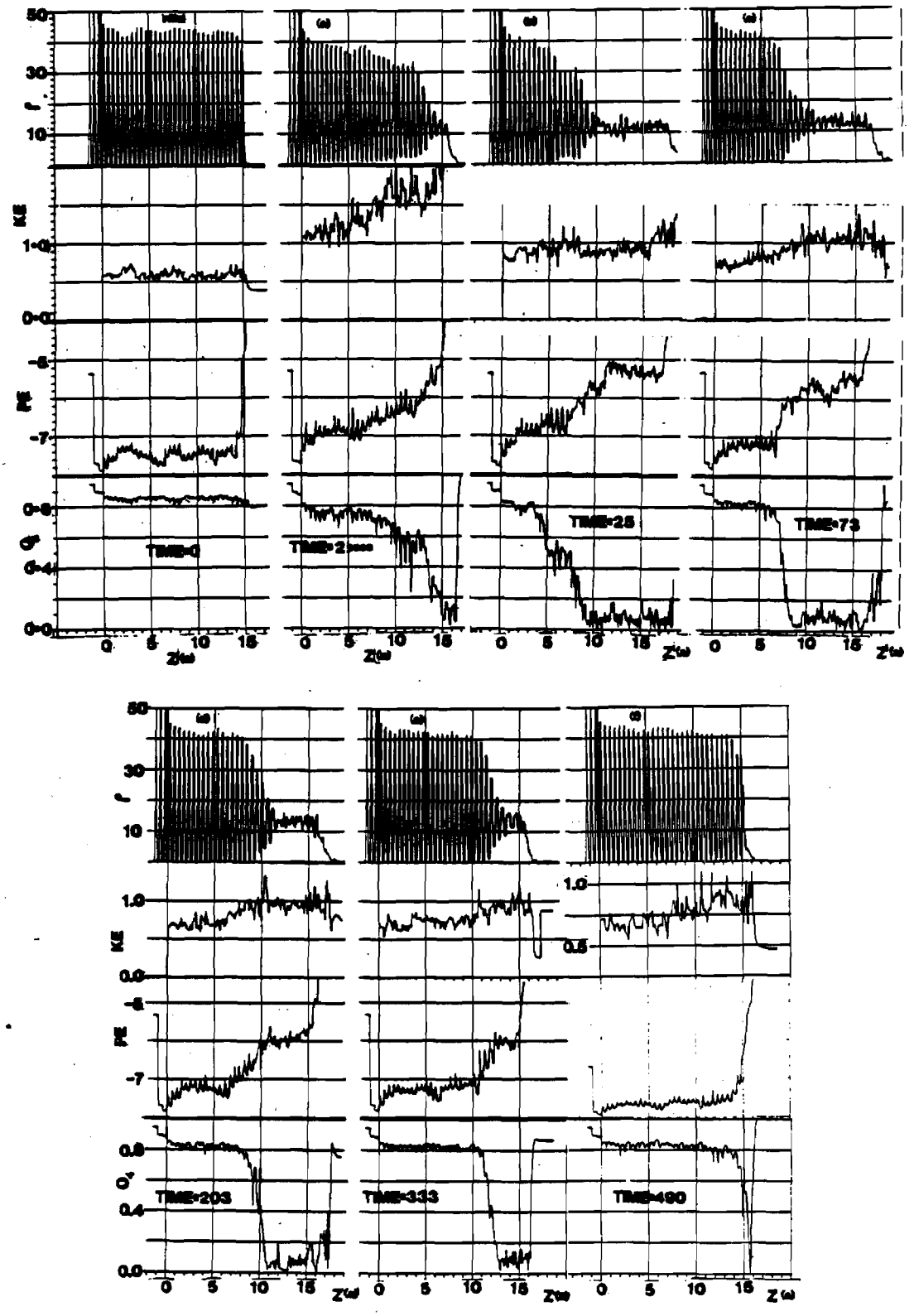

FIG. 5. Profiles of number density (ρ), KE, PE, and O_4 vs Z (in units of a) for the (100) system, at selected times after the termination of the heat pulse. The times (in ps) are given in the figure. Note the melting process in (a) and (b) and the resolidification in (c)–(f).

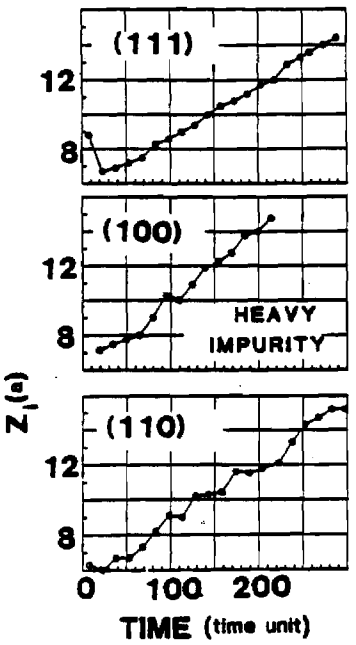

FIG. 6. Interface position z_i (in units of a) vs time (in time units of 2.16 s); (a)–(c) for the heavy impurity systems. The corresponding crystallization velocities are $v = 7.7$, 10.0, and 8.4 m/s for the (111), (100), and (110) systems, respectively.

ged. The difference between the growth modes at these surfaces can be related to the nature of their solid–melt interfaces. As discussed in Sec. IV C, the interface at the close-packed surfaces is of larger physical extent than at the open face (110), exhibiting a more gradual transition between solid to liquid properties. Consequently, growth at the (111) surface involves cooperative ordering over a region in the melt (the diffuse interface) while at the (110) surface it proceeds in a layer by layer fashion. These conclusions are verified by direct observations of the stimulated systems during growth.

Finally, we should emphasize that the observed crystallization velocities in our simulations (and in experiments on rapid crystallization following pulsed laser or electron beam radiation) coupled with the observed negligible degree of undercooling at the interface cannot be analyzed in terms of the conventional models of "continuous" growth. These models are based on equilibrium concepts, employing equilibrium properties and neglect cooperative effects. As we have demonstrated, all of the above assumptions do not hold under conditions of rapid solidification.

[a] Work supported under DOE Contract No. EG-S-05-5489.

[1] U. Landman, R. N. Hill, and M. Mostoller, Phys. Rev. 21, 448 (1980).
[2] (a) D. L. Adams, H. B. Nielsen, J. N. Andersen, J. Stensgaard; R. Feidenhans'l, and J. E. Sørensen, Phys. Rev. Lett. 49, 669 (1982); (b) H. B. Nielsen, J. N. Andersen, L. Petersen, and D. L. Adams, J. Phys. C 15, L1113 (1982) and 17, 173 (1984); (c) N. B. Nielsen and D. L. Adams, *ibid.* 15, 615 (1982); (d) J. R. Noonan and H. L. David, Phys. Rev. B 29, 4349 (1984).
[3] (a) H. L. Davis, J. R. Noonan, and L. H. Jenkins, Surf. Sci. 83, 559 (1979); (b) H. L. Davis and J. R. Noonan, J. Vac. Sci. Technol. 20, 842 (1982).
[4] (a) V. Jensen, J. N. Andersen, H. B. Niellsen, and D. L. Adams, Surf. Sci. 116, 66 (1982); (b) H. L. Davis and D. M. Zehner, J. Vac. Sci. Technol. 17, 190 (1980).
[5] S. Sokolov, F. Jona, and P. M. Marcus, Phys. Rev. B 29, 5402 (1984); 31, 1929 (1985); Solid State Commun. 49, 307 (1984), where work on multilayer relaxation of layer spacings and registry for Fe(211), Fe(310), and Fe(210) is described.
[6] (a) R. N. Barnett, R. G. Barrera, C. L. Cleveland, and U. Landman, Phys. Rev. B 28, 1667 (1983); (b) R. N. Barnett, C. L. Cleveland, and U. Landman, Phys. Rev. B 28, 1685 (1983); (c) R. N. Barnett, U. Landman, and C. L. Cleveland, Phys. Rev. Lett. 51, 1359 (1983); (d) R. N. Barnett, U. Landman and C. L. Cleveland, Phys. Rev. B 28, 6647 (1983).
[7] Z. D. Popovic, J. P. Carbotte, and G. R. Piercy, J. Phys. F 4, 351 (1974).
[8] N. D. Lang and W. Kohn, Phys. Rev. B 2, 4555 (1970).
[9] J. W. M. Frenken, J. F. van der Veen, R. N. Barnett, U. Landman, and C. L. Cleveland, where experimental and theoretical results for Pb(110) are presented (to be published).
[10] For a recent review on LEED, see F. Jona, J. Phys. C. 11, 4271 (1978).
[11] M. W. Finnis and V. Heine, J. Phys. F 4, L37 (1974).
[12] J. P. Perdew, Phys. Rev. B 25, C291 (1982).
[13] C. Tejedor and F. Flores, J. Phys. F 6, 1647 (1976).
[14] G. Ehrlich and K. Stoit, Annu. Rev. Phys. Chem. 31, 603 (1980).
[15] G. De Lorenzi, J. Jacucci, and V. Pontikis, Surf. Sci. 116, 391 (1982).
[16] U. Landman and R. H. Rast, in *Dynamics on Surfaces*, Proceedings of the 17th Jerusalem Symposium, edited by B. Pullman, J. Jortner, A. Nitzan, and B. Gerber (Reidel, Boston, 1984), p. 215.
[17] H. K. McDowell and J. D. Doll, J. Chem. Phys. 78, 3219 (1983); J. D. Doll, H. K. McDowell, and S. M. Valone, J. Chem. Phys. 78, 5276 (1983).
[18] U. Landman, Isr. J. Chem. 22, 339 (1982); M. F. Shlesinger and U. Landman, *Applied Stochastic Processes*, edited by G. Adomian (Academic, New York, 1980).
[19] T. Halicioglu and G. M. Pound, Phys. Status Solidi (a) 30, 619 (1975); $\sigma_{Cu} = 2.338$ Å, $\sigma_{Pb} = 3.197$ Å, $\epsilon_{Cu} = 470$ K, $\epsilon_{Pb} = 2743$ K; $\sigma_{Cu-Pb} = (\sigma_{Cu} + \sigma_{Pb})/2$, $\epsilon_{Cu-Pb} = (\epsilon_{Cu}\epsilon_{Pb})^{1/2}$.
[20] G. S. De, U. Landman, and M. Rasolt, Phys. Rev. B 21, 3256 (1980).
[21] *Laser–Solid Interactions and Transient Thermal Processing of Materials*, edited by J. Narayan, W. L. Brown, and R. A. Lemons (Elsevier, New York, 1983).
[22] C. L. Cleveland, Uzi Landman, and R. N. Barnett, Phys. Rev. Lett. 49, 790 (1982); Phys. Rev. B (to be published).
[23] R. F. Wood and G. E. Giles, Phys. Rev. 23, 2923 (1981); R. F. Wood, J. R. Kirkpatrick, and G. E. Giles, *ibid.* 23, 5555 (1981); R. F. Wood, Phys. Rev. B 25, 2786 (1982).
[24] G. H. Gilmer, in *Laser–Solid Interactions and Transient Thermal Processing of Materials*, edited by J. Narayan, W. L. Brown, and R. A. Lemons (Elsevier, New York, 1983), p. 249.
[25] J. Narayan in Inst. Phys. Conf. Ser. No. 60, (Institute of Physics, London, 1981), p. 101; A. G. Cullis, D. T. Hurle, H. C. Webber, N. G. Chew, J. M. Poate, P. Baeri, and G. Forti, Appl. Phys. Lett. 38, 642 (1981).
[26] U. Landman, C. L. Cleveland, and C. S. Brown, Phys. Rev. Lett. 45, 2032 (1980).
[27] For a recent review, see F. F. Abraham, J. Vac. Sci. Technol. B 2, 534 (1984).
[28] M. Parrinello and A. Rahman, Phys. Rev. Lett. 45, 11996 (1980).
[29] I. N. Krupskii and V. G. Manzhelii, Sov. Phys. JETP 28, 1097 (1969).
[30] A. Rahman, Phys. Rev. 136, A405 (1964).
[31] J. H. Dymond, J. Chem. Phys. 60, 972 (1974).
[32] J. W. Gibbs, in *Collected Works* (Longmans, Green, New York, 1928).
[33] A. Bonissent, in *Interfacial Aspects of Phase Transformations*, edited by B. Mutaftschiev (Reidel, Boston, 1982), p. 143.
[34] (a) J. D. Bernal and S. King, *Physics of Simple Liquids* (North-Holland, Amsterdam, 1968), p. 231; (b) J. D. Bernal, Proc. R. Soc. London, Ser. A 280, 299 (1964).
[35] A. Bonissent and F. F. Abraham, J. Chem. Phys. 74, 1306 (1981).
[36] For a review, see Ref. 26.
[37] J. Q. Broughton, A. Bonissent, and F. F. Abraham, J. Chem. Phys. 74, 4029 (1981).
[38] J. Q. Broughton and G. H. Gilmer, J. Chem. Phys. 79, 5119 (1983).
[39] J. M. Poate, in Ref. 21, p. 263.
[40] D. P. Woodruff, *The Solid–Liquid Interface* (Cambridge University, London, 1973), Chap. 8.
[41] H. A. Wilson, Philos. Mag. 50, 238 (1900); J. Frenkel, Physik Z. Sovjetunion; 1, 498 (1932); K. A. Jackson and B. Chalmers, Can. J. Phys. 34, 473 (1956).
[42] J. W. Cahn, Acta Metall. 8, 554 (1960).
[43] K. A. Jackson, D. R. Uhlmann, and J. D. Hunt, J. Cryst. Growth 1, 1 (1967), where a critique of the model suggested by Cahn (Ref. 42) is given.

New Molecular-Dynamics Method for Metallic Systems

R. N. Barnett, C. L. Cleveland, and Uzi Landman
School of Physics, Georgia Institute of Technology, Atlanta, Georgia 30332
(Received 17 December 1984)

We present a new formulation for simulations of metallic systems which allows for volume and shape variations and incorporates explicitly the dependence on density of the "volume energy" and the effective pair potentials. Simulations of liquid Mg yield good agreement with experiments for several properties including internal energy, density, and structure factors at several temperatures (T) and pressures (P). Correlations between fluctuations in T, P, and volume are in approximate agreement with the appropriate thermodynamic relations.

PACS numbers: 61.20.Ja, 61.25.Mv

Molecular-dynamics (MD) simulations, which consist of the numerical solution of the equations of motion of a many-particle system, have become an important theoretical tool in investigations of the microscopic structure and dynamics of material systems. Practical simulations of extended systems involve up to a few thousand particles (N), contained in a calculational cell (CC) which is repeated via periodic boundary conditions.[1] In earlier work the volume (Ω) of the CC was kept constant, thus yielding phase-space trajectories of an (N,Ω,U) ensemble (or a microcanonical ensemble since the internal energy U is conserved). To study phenomena which inherently involve changes in volume or structure several new methods have been proposed and implemented, such as the *Ansatz* Lagrangian[2,3] and constrained-dynamics[1] techniques.

Underlying the structural and dynamical properties are the various contributions to the total energy of the material. While for the rare-gas, molecular, and ionic systems a satisfactory description may be given in terms of pairwise (and higher-order) interactions, it is well known that the cohesive energy of a metal contains, in addition, density-dependent contributions which are structure independent and that the metallic effective pair potentials themselves depend on conduction-electron density.[4]

In the new method which we have developed the volume-dependent contributions to the energy are explicitly included in the derivation of the Lagrangian equations of motion. The method thus circumvents the need to impose artifically an external "electron pressure" in the simulation and is designed for studies of equilibrium and nonequilibrium phenomena involving volume and structural changes in metallic systems.

Consider a metallic alloy with N_σ particles of species σ and a total number of particles $N=\sum_\sigma N_\sigma$ contained in a CC of volume Ω. The periodic replications of the CC are labeled by $\mathbf{l}=(l_1,l_2,l_3)^T$ with $l_\alpha=0,\pm1,\pm2,\ldots$ $(\alpha=1,2,3)$, and the position of particle j in cell $\mathbf{l}$ is given by $\mathbf{r}_j(\mathbf{l})=\mathbf{H}\cdot(\mathbf{s}_j+\mathbf{l})$, where $\mathbf{s}_j=(s_{j1},s_{j2},s_{j3})^T$, $-\frac{1}{2}<s_{j\alpha}<\frac{1}{2}$ $(\alpha=1,2,3)$, and $\mathbf{H}$ is a 3×3 matrix with $\det(\mathbf{H})=\Omega$. The cohesive energy for a simple metal alloy can be written as[4]

$$E_T=E_\Omega+\tfrac{1}{2}\sum_{\mathbf{l},j}{}'\phi_{ij}^{(2)}(r_s,r_{ij}(\mathbf{l})), \tag{1a}$$

$$E_\Omega=\sum_\sigma N_\sigma[Z_\sigma E_{\rm el}(r_s)+\phi_\sigma^{(1)}(r_s)], \tag{1b}$$

where $r_{ij}(\mathbf{l})=|\mathbf{r}_i-\mathbf{r}_j(\mathbf{l})|$, r_s is the electron density parameter, Z_σ is the valence number, $E_{\rm el}$ is the energy of the uniform electron gas, and $\phi_\sigma^{(1)}$ is a single-particle contribution. $\phi^{(1)}$ and the density-dependent effective pair potential $\phi^{(2)}$ are derived via pseudopotential theory[4] and their specific form depends upon the choice of ionic pseudopotentials (model, local, nonlocal).

To allow for temporal volume and shape variations the components of the matrix $\mathbf{H}$ are taken as dynamical variables. The *Ansatz* Lagrangian is obtained by replacement of all the terms in the kinetic energy which involve $\dot{\mathbf{H}}$ with $\frac{1}{2}W\,\mathrm{Tr}(\dot{\mathbf{H}}^T\cdot\dot{\mathbf{H}})$, where W has the dimension of mass, yielding

$$\mathcal{L}=\tfrac{1}{2}\sum_i m_i\dot{\mathbf{s}}_i^T\cdot\mathbf{G}\cdot\dot{\mathbf{s}}_i-\tfrac{1}{2}\sum_{\mathbf{l},j}{}'\phi_{ij}^{(2)}(r_s,r_{ij}(\mathbf{l}))+\tfrac{1}{2}W\,\mathrm{Tr}(\dot{\mathbf{H}}^T\cdot\dot{\mathbf{H}})-E_\Omega(r_s)-P_{\rm ext}\Omega, \tag{2}$$

where $\mathbf{G}=\mathbf{H}^T\cdot\mathbf{H}$. The above Lagrangian extends that of Parrinello and Rahman[2] to include the volume energy $E_\Omega(r_s)$ and the volume dependence in the pair potentials. The restriction to volume variation only (Andersen's Lagrangian[3]) is obtained by setting $\mathbf{H}=L\hat{\mathbf{H}}$, where $\hat{\mathbf{H}}$ is a constant matrix and L is a dynamical variable with the dimension of length. With the definitions $V_{ij}(r_s,X_{ij}(\mathbf{l}))=\phi_{ij}^{(2)}(r_s,r_{ij}(\mathbf{l}))$, where $X_{ij}(\mathbf{l})=r_{ij}(\mathbf{l})/r_s$, and $\chi_{ij}(r_s,X)=-(1/X)\partial V_{ij}(r_s,X)/\partial X$, and with the prime denoting derivatives with respect to r_s, the Lagrangian

equations of motion follow:

$$m_l\ddot{\mathbf{s}}_l = r_s^{-2}\sum_{j,1}{}'\chi_{lj}(r_s,X_{lj}(1))\mathbf{s}_{lj}(1) - \mathbf{G}^{-1}\cdot\dot{\mathbf{G}}\cdot\dot{\mathbf{s}}_l, \tag{3a}$$

$$W\ddot{\mathbf{H}} = \mathbf{H}\cdot\sum_l m_l\dot{\mathbf{s}}_l\dot{\mathbf{s}}_l^T + \tfrac{1}{2}r_s^{-2}\mathbf{H}\cdot\sum_{l,j,1}{}'\chi_{lj}(r_s,X_{lj}(1))\mathbf{s}_{lj}(1)\mathbf{s}_{lj}(1)^T$$

$$-(\mathbf{H}^{-1})^T\left[\frac{1}{6}\sum_{l,j,1}{}'[r_s V_{lj}'(r_s,X_{lj}(1)) + X_{lj}(1)^2\chi_{lj}(r_s,X_{lj}(1))] + P_{\rm ext}\Omega + \tfrac{1}{3}r_s E_\Omega'(r_s)\right]. \tag{3b}$$

For a constant-shape MD CC, Eq. (3b) is replaced by

$$W\,\mathrm{Tr}(\mathbf{G})L^{-1}\ddot{L} = \sum_l m_l\dot{\mathbf{s}}_l^T\cdot\mathbf{G}\cdot\mathbf{s}_l - r_s\left[\frac{1}{2}\sum_{l,j,1}{}'V_{lj}'(r_s,X_{lj}(1)) + E_\Omega'(r_s)\right] - 3\Omega P_{\rm ext}. \tag{3c}$$

For calculations of dynamical properties a proper magnitude of the mass parameter W is to be chosen. Adopting the approach of Andersen[3] we start from an approximate equation of motion for the cell volume Ω, $d^2\Omega^{1/3}/dt^2 = W^{-1}(P - P_{\rm ext})\Omega^{2/3}$, where the internal pressure is given by $P \simeq -3B_s(1-\Omega^{1/3}/\langle\Omega\rangle^{1/3})$ and B_s is the adiabatic bulk modulus. The wavelength of the acoustic phonon, whose frequency equals that of the volume oscillations determined from the above equation $[\omega_\Omega = (3B_s\Omega^{1/3}/W)^{1/2}]$, is $\lambda_\Omega = 2\pi(W/3M)^{1/2}\Omega^{1/3}$, where M is the total mass of the particles in the CC. Modes with $\lambda \lesssim L$, where L approximates the linear dimension of the CC, are already present in the simulation; we choose W such that $\lambda_\Omega \simeq 2.5L$.

To illustrate the method we carried out simulations of liquid magnesium at several temperatures and external pressures. Since liquids do not resist shear stresses, random fluctuations in the CC shape may eventually result in undesirable cell shapes which lead to interactions between particle images. To alleviate this problem and to minimize any deviation in spherical symmetry due to the periodic boundary conditions, we have used Eq. (3c) (constant-shape CC) with $\dot{\mathbf{H}}$ chosen so that $\dot{\mathbf{H}}\cdot\mathbf{I}$ describes an fcc lattice. The single-particle and pair-particle potentials, $\phi^{(1)}$ and $\phi^{(2)}$, were obtained from a simplified Heine-Abarenkov ionic pseudopotential[5] with exchange correlation included via the Singwi *et al.*[6] local-field correction. In addition, the Hartree contribution to $\phi^{(1)}$ was scaled by a parameter $z_{\rm H}$.[7] The pseudopoential parameters r_c, u_c, and $z_{\rm H}$ were chosen to fit exactly the zero-temperature cohesive energy, bulk modulus, and density and to give the correct, hcp, crystalline structure ($r_c = 1.824a_0$, $u_c = 0.5484$ Ry, $z_{\rm H} = 0.9407$). The resulting pair potential and its derivative with respect to r_s are shown in Fig. 1, for densities corresponding to 0 K and that of the liquid at 960 K. The integration time step was $\Delta t = 1.46\times10^{-15}$ sec and $N = 500$ particles. Simulations were performed for $P_{\rm ext} = 0$ at three temperatures, 960, 1070, and 1150 K, and for $P_{\rm ext} = 0.1$ mRy/a_0^3 at $T = 1070$ K [T(melting) = 922 K]. The period of volume oscillations was found to be $t_\Omega \simeq 1300\Delta t$. The results shown in Table I are averaged over intervals of at least $5t_\Omega$ for the equilibrated samples, chosen so that the average particle and cell temperatures [left- and right-hand sides in Eq. (4), respectively] were approximately equal:

$$(3N-3)^{-1}\langle\textstyle\sum_l m_l\dot{\mathbf{s}}_l^T\cdot\mathbf{G}\cdot\dot{\mathbf{s}}_l\rangle \simeq \langle W\,\mathrm{Tr}(\dot{\mathbf{H}}^T\cdot\dot{\mathbf{H}})\rangle. \tag{4}$$

As mentioned above, an advantage of the present formulation is that the internal pressure P of the system [Eq. (5)] contains all contributions and at equilibrium, $\langle P\rangle = P_{\rm ext}$, which yields the correct density. The internal (virial) pressure is given by

$$P = \left[-r_s\left[E_\Omega'(r_s) + \tfrac{1}{2}\sum_{l,j,1}{}'V_{lj}'(r_s,X_{lj}(1))\right] - \sum_l m_l\dot{\mathbf{s}}_l^T\cdot\mathbf{G}\cdot\dot{\mathbf{s}}_l\right](3\Omega)^{-1}. \tag{5}$$

At $T = 960$ K, the volume, pair-potential, and kinetic contributions to $\langle P\rangle$ are -0.55, 0.52, and 0.03 mRy/a_0^3, respectively.

We have calculated, in addition to average thermodynamic quantities, their mean square deviations for which the following relations hold in the isoenthalpic-isobaric ensemble[12]:

$$c_p = \left[\frac{2}{3} - \frac{N\langle\Delta T^2\rangle}{\langle T\rangle^2}\right]^{-1}, \qquad B_s = \frac{\langle\Omega\rangle\langle T\rangle}{\langle\Delta\Omega^2\rangle},$$

where c_p is the isobaric specific heat per atom; B_s is the adiabatic bulk modulus; T, the kinetic temperature, is defined as twice the instantaneous kinetic energy per degree of freedom; and angular brackets indicate a time average.

The results obtained are shown in Table I along with available experimental values. The internal energy, U, is the sum of the potential- and kinetic-energy terms in the Lagrangian, but with omission of the term in-

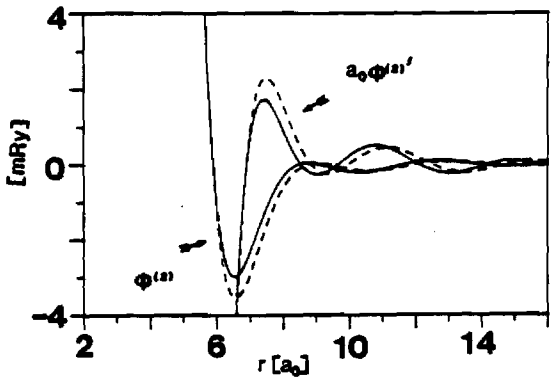

FIG. 1. Effective pair potential, $\phi^{(2)}$, and derivative with respect to r_s, $\phi^{(2)\prime}=\partial\phi^{(2)}/\partial r_s$, plotted vs interparticle distance, r, for densities corresponding to temperatures of 0 K ($r_s=2.650a_0$, solid lines) and 960 K ($r_s=2.764a_0$, dashed lines).

volving $\dot{H}$. The experimental values for U are obtained from the cohesive energy at $T=0$,[8] the ionization energy,[9] the heat of melting,[8] and $c_p(T)$ for liquid and crystalline phases.[10] The thermal expansion coefficient, $\alpha=r_s^{-1}\partial r_s/\partial T$, is obtained from a two-parameter fit to the simulation results, $r_s=a_0(5.404\times10^{-2}-6.94\times10^{-6}T\,[\mathrm{K}])^{-1/3}$. The agreement between experiment and simulation for U, r_s, and α is quite good considering the uncertainty in the experimental values and the fact that a simple local model pseudopotential fit to $T=0$ properties was used in the simulation. The experimental value of B_T was obtained from that of B_s, and the measured value[11] of $B_T/B_s=0.75$ (at melting). The entries in Table I labeled "(diff)" were estimated from differences in $U(T,P)$. Reliable experimental values for c_p are available only near melting, and c_p is estimated[10] to be constant over the temperature range of our simulations, while our results indicate that c_p decreases with increasing T. The differences between the experimental and estimated (diff) quantities and the corresponding thermodynamic relations involving fluctuations may be attributed to the small number of particles ($N=500$) and the difficulty in adequately sampling the phase space due to the time scale associated with volume oscillations [see discussions preceding Eq. (4)]. Finally, we have calculated the diffusion constants, D, via the velocity autocorrelation functions, and the electrical resistivity, ρ, and thermopower, Q, using the Faber-Ziman theory[13] and the static structure factors obtained from the simulation (the correspond-

TABLE I. Simulation results and comparison with available experimental data (expt). Angular brackets indicate time averages (see text). With the exception of B_T(diff), all simulation results correspond to $\langle P\rangle=P_{\mathrm{ext}}=0$.

$\langle T\rangle$	960 K	1070 K	1150 K
U/N (expt) (Ry)[a]	−1.762	−1.759	−1.757
$\langle U/N\rangle$	−1.7496	−1.7464	−1.7443
r_s(expt) (a_0)[b]	2.741	2.759	2.772
$\langle r_s\rangle$	2.764	2.779	2.790
α(expt) (10^{-5} K^{-1})[b]	5.63	5.73	5.83
α	4.88	4.97	5.03
c_p/k_B (expt)[c]	3.9	3.9	3.9
c_p(diff)/k_B[d]	4.88	4.27	3.90
$[\frac{3}{2}-(\langle T\rangle^2/N\langle\Delta T^2\rangle)^{-1}]^{-1}$	3.8	4.7	3.8
B_s(expt) (mRy/a_0^3)[e]	1.75	1.67	1.60
$\langle\Omega\rangle\langle k_BT\rangle/\langle\Delta\Omega^2\rangle$	1.76	1.68	1.70
$\omega_0^2W/3\langle\Omega^{1/3}\rangle$	1.4	1.3	1.3
B_T(expt)[e]	1.31	1.25	1.20
B_T(diff)[d]		1.4	
D (10^{-5} cm^2/sec)	2.4	3.6	4.9
ρ ($\mu\Omega$ cm)	16.5	16.0	15.8
Q (μV/K)	1.45	2.47	2.82

[a]References 8, 9, and 10.
[b]Reference 9.
[c]Reference 10.
[d]Estimated from differences (see text); the averages of the two temperatures used to obtain c_p(diff) are 1015, 1055, and 1100 K, respectively.
[e]Reference 11.

ing pair-correlation function at $T = 960$ K is in good agreement with experiment[14]). Our results of a positive Q and negative $d\rho/dT$ are typical of divalent liquid metals. Experimental values for ρ and Q at melting are 27 $\mu\Omega$ cm and 1.5 μV/k, respectively.[15]

In conclusion, we have developed an *Ansatz* Lagrangian method for the MD simulation of simple metal systems in which the density dependence of both the structure-dependent "volume-energy," E_Ω, and the effective pair potential is explicitly included. The volume (and optionally the shape) of the MD CC is a dynamic variable; the cell responds to pressure fluctuations and there is no need to impose an external "electronic" pressure to achieve the correct density. The method is thus suited to simulation of processes which involve changes in temperature, pressure, and/or volume such as crystal nucleation and the formation and annealing of a metallic glass. Since fluctuations in these quantities are predicted to play an important role in the nonequilibrium processes mentioned above,[16] our method should result in a more realistic simulation of such processes than the conventional constant-volume or density-independent potential simulations.

This work was supported by the U. S. Department of Energy through Contract No. EG-S-05-5489.

[1]For a recent review see F. F. Abraham, J. Vac. Sci. Technol. B2, 534 (1984).

[2]M. Parrinello and A. Rahman, Phys. Rev. Lett. 45, 1196 (1980), and J. Appl. Phys. 52, 7182 (1981).

[3]H. C. Andersen, J. Chem. Phys. 72, 2384 (1980).

[4]See, e.g., W. A. Harrison, *Pseudopotentials in the Theory of Metals* (Benjamin, Reading, Mass., 1966).

[5]R. N. Barnett, Uzi Landman, and C. L. Cleveland, Phys. Rev. B 28, 1685 (1983).

[6]K. S. Singwi, A. Sjolander, M. P. Tosi, and R. H. Land, Phys. Rev. B 1, 1044 (1970).

[7]D. L. Price, K. S. Singwi, and M. P. Tosi, Phys. Rev. B 2, 2983 (1970).

[8]Karl A. Gschneider, in *Solid State Physics: Advances in Research and Applications*, edited by H. Ehrenreich, F. Seitz, and D. Turnbull (Academic, New York, 1964), Vol. 16.

[9]*Handbook of Chemistry and Physics* (CRC Press, Cleveland, Ohio, 1975), 55th ed.

[10]P. Hultgren, R. L. Orr, P. D. Anderson, and K. K. Kelley, *Selected Values of Thermodynamic Properties of Metals and Alloys* (Wiley, New York, 1963).

[11]S. P. McAlister, E. D. Crozier, and J. F. Cochran, Can. J. Phys. 19, 1847 (1974).

[12]J. M. Haile and H. W. Graben, Mol. Phys. 40, 1433 (1980).

[13]T. E. Faber, *Theory of Liquid Metals* (Cambridge Univ. Press, Cambridge, 1972).

[14]Y. Waseda, *The Structure of Non-Crystalline Materials* (McGraw-Hill, New York, 1980).

[15]G. Bush and H. J. Guntherodt, in Ref. 8, Vol. 29.

[16]See, e.g., T. Egami and D. Srolovitz, J. Phys. F 12, 2141 (1982).

Electron Localization in Alkali-Halide Clusters

Uzi Landman
School of Physics, Georgia Institute of Technology, Atlanta, Georgia 30332, and Institute of Theoretical Physics, Chalmers University of Technology, 412 96 Goteborg, Sweden

and

Dafna Scharf and Joshua Jortner
Department of Chemistry, Tel Aviv University, 69978 Tel Aviv, Israel
(Received 14 January 1985)

The quantum path-integral molecular-dynamics method was applied to explore the structure, energetics, and dynamics of an excess electron interacting with an alkali-halide cluster. Four distinct modes of electron localization were established, which depend on the cluster composition, size, and structure; they involve an internal *F*-center defect, an external surface state, dissociative detachment of an alkali atom, and structural isomerization induced by electron attachment.

PACS numbers: 71.45.Nt, 36.40.+d, 61.20.Ja

Structural, electronic, dynamic, and chemical characteristics of materials depend primarily on the state (phase) and the degree (size) of aggregation. Small clusters, i.e., finite aggregates containing 3–500 particles, exhibit unique physical and chemical phenomena, which are of both fundamental and technological significance, and provide ways and means to explore the "transition" from molecular to condensed-matter systems.[1] Theoretical studies of clusters were hampered by the relatively large number of particles, which renders the adaptation of molecular science techniques rather cumbersome, while the lack of translational symmetry inhibits the employment of solid-state methodology. Molecular-dynamics (MD) simulations, consisting of the generation of phase-space trajectories via the numerical integration of the (classical) equations of motion for a many-particle system, are particularly suitable for the study of the structure and dynamics of small clusters.[2,3] In this context, localized excess electron states in clusters[4] are of considerable interest with regard to the (nonreactive and reactive) mechanisms of electron attachment, the formation of bulk or surface states, and the role of the excess electron as a probe for the interrogation of the nuclear dynamics of the cluster. Futhermore, quantum phenomena are expected to be pronounced in such systems since the electron wavelength is comparable to the cluster size. In this paper we report on the structure, energetics, and dynamics of alkali-halide clusters (AHC) studied with classical MD, and of electron alkali clusters studied with the quantum path-integral MD method (QUPID).[5–8] AHC were chosen since the nature of the interionic interactions is well understood and in view of the abundance of model calculations and experimental information of these systems.[9] Our QUPID calculations establish four modes of localization of an excess electron in AHC: (i) an *F*-center defect with the excess electron replacing an internal halide ion; (ii) a new surface state, i.e., a "surface *F* center" of the excess electron; (iii) dissociative electron attachment to AHC resulting in the formation of an "isolated" alkali atom; (iv) structural isomerization induced by electron attachment. Our calculations establish the compositional, structural, and size dependence of these various localization mechanisms.

The QUPID method[6–8] was applied to a system of an electron interacting with an AHC consisting of N ions (N_1 cations and N_2 anions). The interionic potential energy within the AHC is $V_{\rm AHC}=\sum_{i<j}\Phi_{ij}(R_{ij})$, with the interionic pair potentials $\Phi_{ij}(R_{ij})$ being given by the Born-Mayer potential with the parameters determined by Fumi and Tosi.[10] The electron-AHC potential is $V_e(\mathbf{r})=\sum_i\Phi_{ei}(\mathbf{r}-\mathbf{R}_i)$ consisting of a sum of electron-ion potentials, which are described by the purely repulsive pseudopotential $\Phi_{ei}(r)=e^2/r$ for the electron-anion interaction and by the local pseudopotential[11] $\Phi_{ei}(r)=-e^2/R_c$, $r\le R_c$, and $\Phi_{ei}(r)=-e^2/r$, $r>R_c$, for the electron–positive-ion interaction. The Hamiltonian is $H=K_e+V_e+K_{\rm AHC}+V_{\rm AHC}$, where K_e and $K_{\rm AHC}$ are the kinetic-energy operators for the electron (mass m) and of the ions (masses $M_i=M_1$ and M_2), respectively. Observables are obtained from the quantum partition function $Z=\lim_{p\to\infty}[Z_p]^p$ with

$$Z_p=\mathrm{Tr}[\exp(-\tau K_{\rm AHC})\exp(-\tau K_e)\exp(-\tau V_{\rm AHC})\exp(-\tau V_e)],$$

where $\tau=\beta/p$ and $\beta=(k_BT)^{-1}$ is the inverse temperature. If we make use of the free particle propagator[12] Z_p is

$$Z_p=\prod_{\alpha=1,2}\left[\frac{M_\alpha}{2\pi\tau\hbar^2}\right]^{3N_\alpha p/2}\left[\frac{m}{2\pi\tau\hbar^2}\right]^{3p/2}\int\prod_{i=1}^{N}d^3R_i\prod_{i=1}^{p}d^3r_i\exp[-\beta(V_{\rm eff}^e+V_{\rm eff}^I)], \quad (1)$$

where

$$V_{\text{eff}} = \sum_{l=1}^{p}\left[\frac{pm}{2\hbar^2\beta^2}(\mathbf{r}_l-\mathbf{r}_{l+1})^2+V_e(\mathbf{r}_l)/p\right]$$

and

$$V'_{\text{eff}} = \sum_{I=1}^{N}\sum_{l=1}^{p}\frac{pM_I}{2\hbar^2\beta^2}(\mathbf{R}_{I(l)}-\mathbf{R}_{I(l+1)})^2+V_{\text{AHC}}/p.$$

Equation (1) maps the quantum problem onto the classical statistical mechanics of $N+1$ particles, each consisting of a periodic chain (necklace) of p pseudoparticles (beads) with nearest-neighbor harmonic interchain interactions, whose strengths depend upon the masses (m, M_1, M_2), the temperature (T), and the pseudoparticle number (p). When the thermal wavelength [$\lambda_T=(\beta\hbar^2/M_I)^{1/2}$] is smaller than any relevant length scale, the Gaussian factor in Z_p reduces to a delta function and the necklace collapses to a classical particle. This is the case for the ionic part of our system. The average energy of the system is given at equilibrium by

$$E=\frac{3N}{2\beta}+\langle V_{\text{AHC}}\rangle+K_e+p^{-1}\Big\langle\sum_{l=1}^{p}V_e(\mathbf{r}_l)\Big\rangle$$

with the electron kinetic energy

$$K_e=\frac{3}{2\beta}+\frac{1}{2p}\sum_{l=1}^{p}\Big\langle\frac{\partial V_e(\mathbf{r}_l)}{\partial\mathbf{r}_l}\cdot(\mathbf{r}_l-\mathbf{r}_p)\Big\rangle$$

which consists of the free-particle term ($3/2\beta$) and the contribution from the interaction (K_{int}) with the ions.[13] The statistical averages indicated by angular brackets are over the Boltzmann distributions as defined in Eq. (1). This formalism is converted into a numerical algorithm by noting[14] the equivalence of the sampling described above to that over phase-space trajectories generated via MD by the classical Hamiltonian

$$H=\sum_{l=1}^{p}\frac{m^*\dot{\mathbf{r}}_l^2}{2}+\sum_{I=1}^{N}\frac{M_I\dot{\mathbf{R}}_I^2}{2}+\sum_{l=1}^{p}\left[\frac{pm(\mathbf{r}_l-\mathbf{r}_{l+1})^2}{2\hbar^2\beta^2}+\frac{V_e(\mathbf{r}_l)}{p}\right]+V_{\text{AHC}}, \tag{2}$$

the mass m^* being arbitrary and taken as $m^*=1$ u.

Numerical simulations were performed for an electron interacting with sodium-chloride clusters at about room temperature. On the basis of examination of the stability of the variance of the kinetic-energy contribution K_{int}, the number of "electron beads" was taken as $p=399$. By use of an integration step of $\Delta t=1.03\times10^{-15}$ sec, long equilibration runs were performed [$(1-2)\times10^4\Delta t$]. The reported results were obtained via averaging over $8\times10^3\Delta t$, following equilibration. The electron-ion pseudopotential parameters were varied by changing the cutoff radius R_c in the range $(3.22-5.29)a_0$. From QUPID calculations on a single Na atom, the atomic ionization potential is reproduced (see Table I) for $R_c=5.29a_0$, which seems to be a too-high value for the characterization of this pseudopotential.[6] Therefore, on the basis of pseudopotential parametrization studies[11] and a recent QUPID study[8] of F centers in molten and solid KCl in which the same form of pseudopotential was employed, a value of $R_c=3.22a_0$ (yielding a value of -0.3005 a.u. for the electron binding energy to Na^+, see Table I) is preferred. Fortunately, our conclusions regarding internal and surface-localization modes remain unchanged with respect to reasonable variations of this parameter. In simulations involving the electron-AHC interaction, different initial conditions were employed, two of which for the $[Na_{14}Cl_{13}]^+$ system are portrayed in Figs. 1(a) and 1(b). The resulting final state of the system was found to be independent of the initial conditions.

It has previously been suggested on the basis of zero-temperature structural calculations,[9] and has been confirmed by our classical MD simulations, that when the size of the clusters increases ($N\geq20$), the NaCl cyrstallographic arrangement is preferred for particular stability for clusters forming rectangular structures even if the number of positive and negative ions is not equal. Therefore, we have chosen to study first the interaction of an electron with $[Na_{14}Cl_{13}]^+$ and $[Na_{14}Cl_{12}]^{++}$ clusters, which exhibit pronounced stability. In Figs. 1(c) and 1(e), we present our results (using $R_c=3.22a_0$) for the equilibrium electron-charge distribution obtained from 2D projections of the necklace edge points, and for the nuclear configuration of the clusters. In both cases the electron, which starts in either initial configuration as shown in Figs. 1(a), 1(b), has been localized. However, two distinct modes of electron localizations are exhibited involving *internal* and *external localization* for the doubly charged and singly charged cluster, respectively. The vacancy-containing configuration of the $[Na_{14}Cl_{12}]^{++}$ cluster stabilizes an internally localized excess electron state, with the e surrounded by six Na^+ ions in an octahedral configuration and by twelve Cl^- ions [Fig. 1(e)] which is similar to the case of an F center in the extended solid. The electron affinity of the cluster $E_A=E_B^e+E_c$ is obtained by summing the electron binding energy

$$E_B^e=\frac{3}{2\beta}+K_{\text{int}}+p^{-1}\sum_{l=1}^{p}\langle V_e(\mathbf{r}_l)\rangle$$

and the cluster reorganization energy $E_c=\langle V_{\text{AHC}}\rangle-\langle V_{\text{AHC}}\rangle_0$, where $\langle V_{\text{AHC}}\rangle_0$ is the potential energy of the "bare" AHC in the absence of the electron. The ionic configuration of the e-$[Na_{14}Cl_{12}]^{++}$ cluster is somewhat distorted; however, the gain in $E_B^e(-0.249$

TABLE I. Average equilibrium temperature ($\langle T\rangle$), interionic cluster potential energy ($\langle V_{AHC}\rangle$), electron interaction kinetic energy (K_{int}), electron kinetic energy $K_e = 3/2\beta + K_{int}$, e-AHC interaction potential energy ($\langle V_e\rangle$), electron binding energy (E_B^e), cluster reorganization energy (E_c), electron affinity of cluster (E_A), and Cartesian components of the "electron necklace" gyration radii (R_x^2, R_y^2, R_z^2). Atomic units are used (energy and $\langle T\rangle$ in Hartrees, length in Bohr radii). Variances are given in parentheses. Calculated values of $\langle T\rangle$ and $\langle V_{AHC}\rangle$ for the "bare" clusters: $[Na_{14}Cl_{14}]$, $0.976(0.111)\times10^{-3}$, -3.7296; $[Na_{14}Cl_{13}]^+$, $0.948(0.106)\times10^{-3}$, -3.5911; $[Na_{14}Cl_{12}]^{++}$, $0.954(0.093)\times10^{-3}$, -3.3151; $[Na_5Cl_4]^+$, $1.01(0.38)\times10^{-3}$, -1.0999.

	$10^3\langle T\rangle$	$\langle V_{AHC}\rangle$	10^2K_{int}	K_e	$\langle V_e\rangle$	E_B^e	E_c	E_A	R_x^2	R_y^2	R_z^2
e-$[Na_{14}Cl_{13}]^+$	0.983	−3.4856	6.4195	0.0657	−0.2251	−0.1594	0.1055	−0.0539	5.4	7.0	9.8
$R_c = 3.22$	(0.035)		(0.633)								
e-$[Na_{14}Cl_{13}]^+$	0.972	−3.5768	1.5182	0.0166	−0.0700	−0.0534	0.0143	−0.0391	23.5	23.2	55.2
$R_c = 5.29$	(0.031)		(0.426)								
e-$[Na_{14}Cl_{12}]^{++}$	0.938	−3.2372	7.2203	0.0736	−0.3226	−0.2490	0.0799	−0.1691	4.6	6.8	6.3
$R_c = 3.22$	(0.028)		(0.767)								
e-$[Na_{14}Cl_{12}]^{++}$	0.948	−3.3143	1.9995	0.0214	−0.1365	−0.1151	0.0008	−0.1143	55.3	57.9	43.3
$R_c = 5.29$	(0.025)		(0.956)								
e-$[Na_5Cl_4]^+$	0.950	−1.0059	2.6389	0.0278	−0.3012	−0.2734	0.0940	−0.1794	2.2	2.0	2.5
$R_c = 3.22$	(0.132)		(0.582)								
e-$[Na_5Cl_4]^+$	0.946	−1.0483	3.5453	0.0369	−0.1876	−0.1508	0.0516	−0.0992	5.7	7.2	5.5
$R_c = 4.36$	(0.038)		(0.601)								
e-Na^+	1.038		0.713	0.0087	−0.3092	−0.3005				$R^2 = 3.6$	
$R_c = 3.22$	(0.442)		(0.638)								
e-Na^+	1.043		0.034	0.001 98	−0.2299	−0.2280				$R^2 = 3.4$	
$R_c = 4.36$	(0.527)		(0.049)								
e-Na^+	1.084		0.012	0.0017	−0.18897	−0.1872				$R^2 = 4.9$	
$R_c = 5.29$	(0.574)		(0.032)								

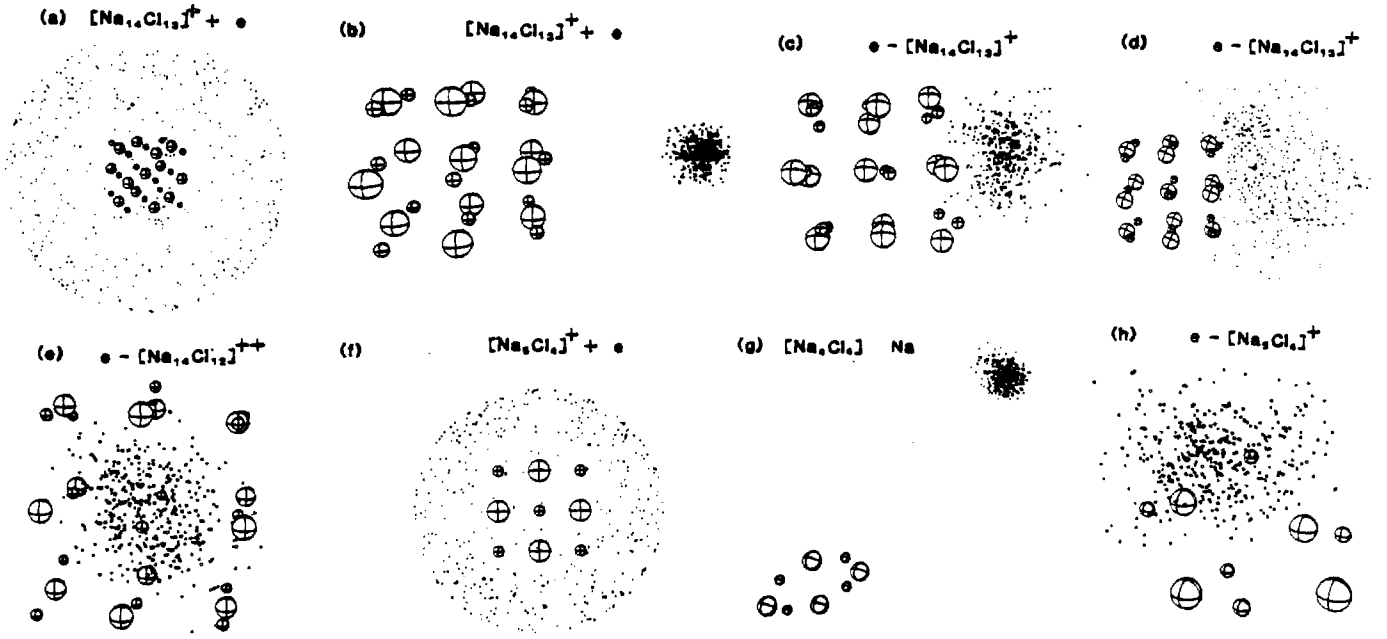

FIG. 1. Ionic configurations and "electron necklace" distributions for an excess electron interacting with sodium-chloride clusters. Small and large spheres correspond to Na^+ and Cl^- ions, respectively. Dots represent 2D projections of the "electron beads." (a),(b) Alternate initial configurations of $[Na_{14}Cl_{13}]^+ + e$ [in (b) the e bead is localized to the right of the cluster] which achieve the equilibrium configurations corresponding to surface states given in (c), $R_c = 3.22a_0$, and (d) $R_c = 5.29a_0$. (e) Equilibrium configuration of e-$[Na_{14}Cl_{12}]^{++}$, $R_c = 3.22a_0$, exhibiting an internal F center. (f) Initial state of e-$[Na_5Cl_4]^+$. (g) Equilibrium configuration of e-$[Na_5Cl_4]^+$ with $R_c = 3.22a_0$ resulting in dissociation of Na. (h) Equilibrium configuration of e-$[Na_5Cl_4]^+$ with $R_c = 4.36a_0$ which corresponds to structural isomerization.

a.u.) exceeds the loss in E_c (0.0799 a.u.) favoring internal localization (Table I). It is of interest to note that the total energy of e-$[Na_{14}Cl_{12}]^{++}$ is rather close to that of $[Na_{14}Cl_{13}]^{+}$, so that the electron binding energy in the cluster is similar to that of a negative ion, analogously to the situation for F-center formation in (extended) ionic crystals,[8] thus establishing the dominance of short-range attractive interactions in electron trapping (localization) phenomena. A drastically different localization mode is obtained in the e-$[Na_{14}Cl_{13}]^{+}$ system [Fig. 1(c)], where a surface state is exhibited. For $R_c = 3.22a_0$ the electron localizes around an Na^+ surface ion [Fig. 1(c)], leaving an essentially neutral $[Na_{13}Cl_{13}]$ cluster, which interacts with the (partially) neutralized Na atom mainly via polarization of the electron cloud (with a residual ionic binding of -0.002 a.u.). We refer to this state as a cluster-surface localized state, which bears close analogy with Tamm's crystal-surface states.[15] When the pseudopotential cutoff R_c increases, the surface state becomes more extended [see Fig. 1(d) for $R_c = 5.29a_0$] [the choice of an abnormally high value for R_c (i.e., $5.29a_0$) prevents internal localization in the $[Na_{14}Cl_{12}]^{++}$ cluster since the internal region is then predominantly repulsive (see Table I), resulting in a surface state]. A measure of the spatial extent of the localized electron is given by the gyration radius of the "electron necklace" $R^2 = (1/2p^2)\langle \sum_{i,j} (r_i - r_j)^2 \rangle$, which demonstrates (Table I) the enhanced localization in the e-$[Na_{14}Cl_{12}]^{++}$ system and the anisotropy of the electron distribution in the e-$[Na_{14}Cl_{13}]^{+}$ system. An estimation of the extent of the electron thermal wave packet is obtained also by

$$R_T = \left[\frac{p}{p-1} \sum_{i=1}^{p} \langle (r_i - r_{i+1})^2 \rangle \right]^{1/2}$$

which for a free electron at room temperature yields $R_T = \sqrt{3}\lambda_T \simeq 56a_0$ ($\lambda_T \simeq 32.34a_0$). In all the calculations reported herein R_T values of $52a_0$–$55a_0$ were obtained, i.e., the same as the free-electron value to within statistical significance (compare to typical interionic distance of $5a_0$ in NaCl clusters).

In smaller clusters novel effects of dissociative electron attachment and cluster isomerization induced by electron localization will be manifested. We have studied the smallest singly ionized cluster exhibiting high stability, i.e., $[Na_5Cl_4]^{+}$, for which the lowest energy configuration is planar with four Na^+ ions at the corners and one at the center of an approximate square.[9] This cluster possesses an isomeric structure (less stable by 0.014 a.u.) in which the ions are arranged in a distorted pyramidal configuration.[9] Adding an electron to the ground-state planar configuration of $[Na_5Cl_4]^{+}$ (with the Na^+ pseudopotential being characterized by $R_c = 3.22a_0$) transforms the system into a neutral $[Na_4Cl_4]$ cluster with a planar ring structure and a dissociated neutral Na atom [Table I and Figs. 1(f) and 1(g), corresponding to the initial- and final-state configurations, respectively]. To demonstrate that this process is driven by the localization of e around a single Na^+ ion, we have performed further simulations by decreasing the cation-electron binding strength, taking $R_c = 4.36a_0$. In this case, extreme localization is not sufficiently counterbalanced by e binding. Instead, the planar structure transforms to the isomeric pyramidal configuration with the electron localized as a diffuse cloud about the tip of the pyramid [Fig. 1(h)]. Electron localization accompanied by structural isomerization will constitute a prevalent phenomenon for AHC with smaller e-cation binding energy, i.e., the heavier alkali metals. In view of the intimate interrelationship between structural isomerization and melting of clusters,[16] it will be interesting to explore the melting of such finite systems induced by electron localization.

This work is supported by the U.S. Department of Energy under Contract No. EG-S-05-5489, and by the U.S. Army through its European Research Office.

[1]See papers in Ber. Bunsenges. Phys. Chem. **88** (1984).

[2]C. L. Briant and J. J. Burton, J. Chem. Phys. **63**, 2045 (1975).

[3]See review by F. F. Abraham, J. Vac. Sci. Technol. **82**, 534 (1984).

[4]J. Jortner, in Ref. 1, p. 188.

[5]D. Chandler and P. G. Wolynes, J. Chem. Phys. **79**, 4078 (1981).

[6]B. De Raedt, H. Sprik, and H. L. Klein, J. Chem. Phys. **80**, 5719 (1984).

[7]D. Chandler, J. Phys. Chem. **88**, 3400 (1984).

[8]M. Parrinello and A. Rahman, J. Chem. Phys. **80**, 860 (1984).

[9]T. P. Martin, Phys. Rep. **95**, 167 (1983).

[10]F. G. Fumi and M. P. Tosi, J. Phys. Chem. Solids **25**, 31, 45 (1964).

[11]R. W. Shaw, Phys. Rev. **174**, 769 (1968).

[12]L. S. Schulman, *Techniques and Applications of Path Integrals* (Wiley, New York, 1981).

[13]M. F. Herman, E. J. Bruskin, and B. J. Berne, J. Chem. Phys. **76**, 5150 (1982).

[14]D. Callaway and A. Rahman, Phys. Rev. Lett. **49**, 613 (1982).

[15]N. F. Mott and R. W. Gurney, *Electronic Processes in Ionic Crystals* (Oxford Univ. Press, Oxford, 1946).

[16]G. Natanson, F. Amar, and R. S. Berry, J. Chem. Phys. **78**, 399 (1983).

The Structure and Dynamics of A Metallic Glass: Molecular Dynamics Simulations

R. N. Barnett, C. L. Cleveland and Uzi Landman

School of Physics

Georgia Institute of Technology

Atlanta, Georgia 30332

(RECEIVED 21 JUNE 1985)

Abstract

The glass transition, structure and dynamics of a $Ca_{67}Mg_{33}$ metallic glass are studied via a new molecular dynamics method incorporating the density dependence of the potentials. Results are in agreement with neutron scattering data. The accessible configurational energy of the glass is found to possess several nearly degenerate potential minima.

Metallic glasses, i.e., the amorphous solid phases formed when segregation and crystalization are avoided by ultra-rapid cooling of the liquid alloys, are the subject of much recent research effort due to their unique physical properties, which are of joint scientific and technological interest.[1] Metallic glasses are distinct from many other glass forming materials due to the lack of bond-network entanglement commonly present in non-metal based glasses. Their stability and ease of formation have been correlated with electronic effects[2] and with metal alloy chemistry and eutectic composition.[3]

Underlying the structural and dynamic properties of materials are the various contributions to the total potential energy, which for a metal alloy can be written as[4]

$$\Phi = E_\Omega(r_s) + \frac{1}{2} \sum_{i,j}' \phi^{(2)}_{i,j}(r_s;|\vec{r}_i - \vec{r}_j|) + \ldots \qquad (1a)$$

$$E_\Omega(r_s) = \sum_\sigma N_\sigma \left[Z_\sigma E_{e\ell}(r_s) + \phi^{(1)}_\sigma(r_s)\right] \qquad (1b)$$

where $\vec{r}_i$ is the position of the i^{th} atom, Z_σ and N_σ are the valence and number of atoms of species σ, r_s is the conduction electron density parameter, $E_{e\ell}$ is the energy per electron of a uniform electron gas,[5] and $\phi^{(1)}$ and $\phi^{(2)}$ are density dependent single-particle and effective pair-interaction potentials. For simple (i.e., s-p bonded) metals Eq. (1a) may be truncated after the second-order (pair-potential) terms, but for other metals higher-order terms may be necessary. $\phi^{(1)}$ and $\phi^{(2)}$ may be derived via pseudopotential theory,[6] and their specific form depends upon the choice of ionic pseudopotential.[7]

Most previous computer studies of metallic glasses have employed "generic" pair-potentials (such as Lennard-Jones, Morse, etc.).[8] While these

studies have contributed to our understanding they do not lend themselves to comparison with experimental results for a specific material and thus do not afford a direct critical assessment of the physical model and numerical procedure employed. Studies using more realistic potentials have been based on random packing models (rpm) for the glass structure[3,9] and thus cannot address questions involving the kinetics and dynamics of the glass transition itself or the dependence of metallic glass properties on thermal history, spatial fluctuations in concentration or temporal fluctuations in local density and stress[10] and in the underlying glass structure.

A fundamental question in relating computer simulated to laboratory prepared glasses is the short time scale of computer simulations in comparison to the experimental ones.[11,12] It has been demonstrated,[12] that, although the glass transition is broadened by the very rapid cooling rates used in computer simulations, it can be unambiguously observed, and the dependence of quantities such as volume and internal energy on thermal history is small and that trends may be extrapolated to experimental cooling rates. Thus, short of performing simulations employing laboratory cooling rates, an assessment of the correspondence between simulation and experimental results may be provided by simulations which employ a realistic description of the energetics for specific metallic glass systems for which extensive experimental data is available.

In order to perform a realistic dynamic simulation of the formation and properties of a metallic glass we have developed a new molecular dynamics (MD) formulation.[4] In our method the density dependence of both the volume energy, E_Ω, and the pair potentials, $\phi^{(2)}$, is explicitly included in the Lagrangian from which the equations of motion are derived. The MD calculational cell (cc) volume (and optionally the shape) respond to differences between the

internal and externally applied stress tensors[4,13] and the potentials are dynamically adjusted in accord with the instantaneous density. Therefore, this method allows isoenthalpic simulations of processes, such as glass formation, which inherently involve changes in density, without having to specify the density at which the pair potentials are evaluated or applying an external "electronic" pressure to partially account for the volume energy.

Temperature control, i.e., cooling, heating, or equilibrating at a specified temperature, is accomplished by including in the Lagrange equations a "dissipation function" $F(t,\{\vec{r}_i\}) = A(t)\ T(\{\dot{\vec{r}}_i\})$ where t is time, T is the instantaneous kinetic temperature (a function of particle velocities[4]) and A(t) is a "viscous damping" coefficient, given by $A(t) = C[T(t) - T_0(t)]/T(t)$, taken to be a function of time but not explicitly of particle velocities. $T_0(t)$ is the "heat reservoir" temperature which may be a specified function of time yielding a well defined continuous heating or cooling rate $\dot{T}_0(t)$.

A most sensitive probe of the nature of inter-atomic forces, and the structure (on various length scales) and dynamics of a glass-forming alloy, is provided by the static and dynamic structure factors obtained from neutron scattering experiments.[1b] To critically assess the structural and dynamical information obtained by our new molecular dynamics simulation method we have chosen to study the metallic glass $Ca_{67}Mg_{33}$, a simple metal glass for which such neutron scattering data is available,[14] and which has been investigated extensively using a random packing model.[9] Our simulation, which is the first such realistic MD simulation of a metallic glass, affords a direct comparison with experiment, provides a faithful description of the material, and our results are in agreement with the experimental data and the principal theoretical results of Hafner.[9] In addition we found that the fully dynamically relaxed glass can be characterized by several nearly degenerate

local potential minima. Transitions between these configurations involve large displacements by a small number of atoms.

The simulated system consisted of 500 particles, 333 Ca and 167 Mg atoms contained in a fixed-shape, variable volume, regular rhombic dodecahedral MD cell.[4] The system of units which we use is: [length] = a_0 (Bohr radius), [mass] = amu (atomic mass unit) and [energy] = Ry, yielding a time unit (tu) = 1.46×10^{-15} sec.

The simulation was performed in four stages (all at zero external pressure): (1) an equilibrium run (with no temperature control) for the hot liquid alloy at T = .01 Ry (1580^0 K, approximately twice the experimental eutectic temperature), for 3×10^4 tu; (2) a "cooling" run of 3×10^4 tu, $\dot{T}_0 = 3 \times 10^{-7}$ Ry/tu (3.2×10^{13} ^{0}K/sec), during which the glass transition occurred; (3) an "equilibrating" run of 14×10^4 tu in duration under temperature control at T_0 = .00191 Ry (300^0K) during which structural relaxation of the glass occurred (the mean-squared- displacement of atoms during the run, $R^2(t) = N^{-1} \sum [\vec{r}_i(t) - \vec{r}_i(0)]^2$, increased in distinct steps while the internal energy decreased); and (4) an equilibrium run for the glass at T = .00191 Ry (without temperature control) of 9×10^4 tu. The MD integration time step size for stages (1) and (2) was Δt = 1 tu, while in the glass Δt = 2.5 tu.

The principal effects of the increase in density in going from the liquid ($r_s = 3.350\ a_0^{-3}$) to the glass ($r_s = 3.136\ a_0^{-3}$) are a decrease in depth of the potential minima and a shift to shorter interatomic distance of the Friedel oscillations in the long-range part.[4] In addition the relative depths of the potentials are altered. The "electronic pressure", $r_s[\partial E_\Omega(r_s)/\partial r_s]/\Omega$, increases from 2.0×10^{-4} Ry/a_0^3 in the liquid to 2.3×10^{-4} Ry/a_0^3 in glass.

The evolution of the system during cooling (stage 2) is shown in Fig. 1.

In Fig. 1(a) the mean squared displacement, $R^2(t)$, and the kinetic temperature, T(t) as functions of time are shown, while Fig. 1(b) shows the (per particle) total internal energy and the potential energies for the two species as functions of temperature (Fig. 1(b) was obtained by performing Gaussian weighted local averages in time (Gaussian width of 1500 tu)). From the break in the slopes of energy vs. T we determine the glass transition temperature to be T_g = 0.0036 Ry (570°K). A similar break in the slope of the volume, Ω, vs. T occurs at the same temperature. This value of T_g is about 0.7 times the experimental eutectic temperature, which is a typical value for measured glass transition temperatures. Note that $R^2(t)$ is constant for t > 2.3×10^4 tu, i.e., after the glass transition, and while the mean potential energies vs. temperature for the two species have markedly different slopes above T_g they have essentially the same slope below T_g, which is to be expected if the glass transition corresponds to a "freezing" of structural relaxation modes. Estimates of the specific heats of the supercooled alloy and glass can be obtained from the slopes of the total internal energy vs. T in the two regions, yielding C_p/k_B = 4 and 3.3, respectively. These values are in approximate agreement with C_p/k_B = 4.15 for the initial equilibrium liquid and 3.16 for the final equilibrium glass obtained from fluctuations in the kinetic temperature.[15,4]

The structure and dynamics of the equilibrium glass are investigated via the radial pair-distribution functions, g(r), and static structure factors, S(q), as well as the density of states, DOS(ω), and dynamic structure factors, S(q,ω). For the glass we observed correspondence between the locations of minima in the partial g(r)'s (not shown) and maxima in the corresponding pair-potentials as discussed by Hafner.[3] Using the known neutron scattering lengths $b_{Ca} = 4.88 \times 10^{-13}$ cm and $b_{Mg} = 5.2 \times 10^{-13}$ cm, we have calculated the

neutron-weighted static and dynamic structure factors which may be compared directly with the experimental results[14] (we omit the incoherent scattering contribution which is estimated[14] to be < 1%). The positions of the first and second peaks of the static structure factor (Fig. 2b), $Q_1 = 1.12\ a_o^{-1}$ and $Q_2 = 1.92\ a_o^{-1}$, are in good agreement with the reported experimental peak positions[14] ($Q_1 = 1.13\ a_o^{-1}$ and $Q_2 = 1.94\ a_o^{-1}$). The density of the simulated alloy, $N/\Omega = .00387\ a_o^{-3}$ is also in good agreement with the experimental value[9] of $.00398\ a_o^{-3}$ (this experimental value is presumably for a $Ca_{70}Mg_{30}$ glass at 6^oK. Indeed, a steepest descent quench of our glass to 0^oK results in a density of $.00397\ a_c^{-3}$). Fig. 2b can also be compared to the relaxed rpm structure factor shown in Fig. 4 of ref. 9. Note that $g_{NN}(r)$ (Fig. 2a), exhibits a split second peak typical of a glass and in addition there are indications of some amount of local order extending to at least the third neighbor shell.

The density of states, DOS, and dynamic structure factor, $S(q,\omega)$ for the equilibrium glass are shown in Fig. 3. The structure factor is shown as a function of frequency, ω, for wavevectors $q_n = nq_1$, where $q_1 = .221\ a_o^{-1}$ is the magnitude of the (220) reciprocal lattice vector of the (fcc) lattice generated by the periodically replicated MD cell. The range of wave vectors, q, for which the structure factor has been reported by Suck et al.[14] corresponds roughly to q_3 through q_{10} in Fig. 3, therefore the calculated results can be compared with the experimental ones given in Fig. 3 of ref. 14, showing general agreement of the line shapes as well as the frequency range (50 meV = $.111\ tu^{-1}$). Note in particular the increase in amplitude at low frequency for $q \simeq Q_1, 2Q_1$, which has been attributed to transverse excitations, suggesting the existence of quasi-zone boundaries in the glass.[8a] From the positions of the peaks in $S(q,\omega)$ for the lower q's in Fig. 3 we may

read points on the dispersion curve for longitudinal phonons which are in agreement with the experimental results and with the theoretical dispersion curves obtained via the relaxed rpm.[9]

The density of states, obtained from the velocity auto-correlation function, is also in agreement with the experimental DOS (Fig. 11 of ref. 9). The small oscillations at low frequencies are an artifact due to the pbc's, complicating the discussion of the power-law behavior of the DOS at low frequencies. The peak in the DOS occurs at about .032 tu^{-1}, compared to .033 tu^{-1} found in the experiment (1 meV = .002219 tu^{-1}). The full width at half maximum of our DOS is .044 tu^{-1}, compared to the experimental width of .042 tu^{-1} while the width of Hafner's model DOS is .051 tu^{-1}. The difference between our DOS and the rpm result[9] occurs on the high frequency side of the maximum where our DOS agrees better with the experimental data.

Having established via direct comparison with experimental data that our MD simulation in which the full energetics of the metallic system is self-consistently incorporated provides a faithful description of the structure and dynamics of the metallic glass system, we conclude with a brief discussion of observations relating to glass dynamics. Examination of the mean squared displacement, $R^2(t)$, at the "equilibrated glass" stage (4) revealed time ranges when $R^2(t)$ increased from about 0.4 a_o^2 to about 0.7 a_o^2, then returned to the original lower value. These changes are accompanied by variations in system properties such as temperature, mean species potential energies, and average shear stress. By performing "steepest descent quenches"[8b] for these different time spans we determined that the system possesses at least four distinct, nearly degenerate, local potential minima ranging from -1.551966 to -1.551942 Ry per atom. Comparison of the atomic positions associated with these potential minima reveals that they result from

structural rearrangements in which, typically, one atom displaces by 3 to 4 a_o (about half the average nearest neighbor distance), the surrounding near-neighbor atoms move less, and the region of rearrangement extends over about three or four nearest neighbor shells of the central atom, or about 15 to 20% of the total volume of the MD cc. We emphasize that the transitions between these accessible local potential minima do not lead to an annealing or relaxation of the glass (over extended times), and that the underlying topology of the configurational energy is similar to that invoked in the "tunneling level" models of low-temperature glass behavior[17] (though the nature of our transitions is different). Further studies of the influence of these configurational transitions on glass properties and the dynamicsnear the glass transition are in progress.

References

Work supported by U. S. DOE Contract No. EG-S-05-5489.

1. (a) Glassy Metals I, eds. H. I. Guntherodt and H. Beck (Springer, N. Y., 1981); (b) Glassy Metals II, eds. H. Beck and H. I. Guntherodt (Springer, N. Y., 1983); (c) S. R. Nagel in Adv. Chem. Phys. 51, 227 (1982).

2. S. R. Nagel and J. Tauc, Phys. Rev. Lett. 35, 380 (1975); see also ref. 1(c).

3. J. Hafner, Phys. Rev. B21, 406 (1981); see also ref. 1(a).

4. R. N. Barnett, C. L. Cleveland, and U. Landman, Phys. Rev. Lett. 54, 1679 (1985).

5. P. Nozieres and D. Pines, Phys. Rev. 111, 442 (1958).

6. See e.g., (a) W. A. Harrison, Pseudopotentials in the Theory of Metals (Benjamin, Reading, Mass., 1966); (b) R. N. Barnett, R. G. Barrera, C. L. Cleveland, and U. Landman, Phys. Rev. B 28, 1667 (1983); see also ref. (3).

7. For the simulation of the Ca-Mg alloy described in this paper we used the simplified Heine-Abarenkov form described in refs. (4) and (6b) with parameters chosen to give the correct zero temperature lattice consntant, cohesive energy, bulk modulus, and crystal structure of the pure species. The values of the parameters are: r_c = 2.191 a_o, u_c = .415029, Z_H = 1.11076 for Ca and r_c = 1.824 a_o, u_c = .548453, Z_H = .940682 for Mg.

8. (a) G. S. Grest, S. R. Nagel and A. Rahman, Phys. Rev. B 29, 5968 (1984); (b) T. A. Weber and F. H. Stillinger, Phys. Rev. B 31, 1954 (1985); see also ref. 1, and 11.

9. J. Hafner, Phys. Rev. B 27, 678 (1983); see also ref. 1.

10. T. Egami and D. Srolovitz, J. Phys. F 12, 2141 (1982).

11. See e.g., C. A. Angell, J. H. R. Clarke, and L. V. Woodcock in Adv. Chem.

Phys. 48, 397 (1981).

12. (a) J. R. Fox and H. C. Andersen, J. Phys. Chem. 88, 4019 (1984); (b) M. H. Grabow and H. C. Andersen in Extended Abstracts, ACerS 87th Annual Meeting (ACerS, Columbus, OH, 1985), p. 160.

13. (a) H. C. Andersen, J. Chem. Phys. 72, 2384 (1980); (b) M. Parinello and A. Rahman, Phys. Rev. Lett. 45, 1196 (1980).

14. J. -B. Suck, H. Rudin, H. J. Guntherodt, and H. Beck, J. Phys. F 11, 1375 (1981); see also ref. 1(b), p. 217.

15. J. M. Haile and H. W. Graben, Molec. Phys. 40, 1433 (1980).

16. A. B. Bahtia and D. E. Thornton, Phys. Rev. B 2, 3004 (1970).

17. See review by J. L. Black in ref. 1(b), p. 167.

Figure Captions

Fig. 1. System evolution during cooling: (a) temperature, T, and mean squared displacement, R^2, vs. time, (b) mean total energy and mean potential energies, PE, versus temperature.

Fig. 2. Number density pair-correlation function, $g_{NN}(r)$, and neutron-weighted static structure factor, S(q) for the glass.

Fig. 3. Neutron-weighted dynamic structure factor, $S(q,\omega)$ in unit of tu (each subdivision equals $(2/\pi)$ tu = 1.41×10^{-3} meV^{-1}, vs. frequency, ω (in tu^{-1}), for wavevectors, q, as specified (Note the scale change for $q < 0.664\ a_o^{-1}$. The scale for each q starts at zero); and density of states, $DOS(\omega)$ (in tu) [total - solid, dashed - Ca, dash-dot - Mg] vs. ω for the glass.

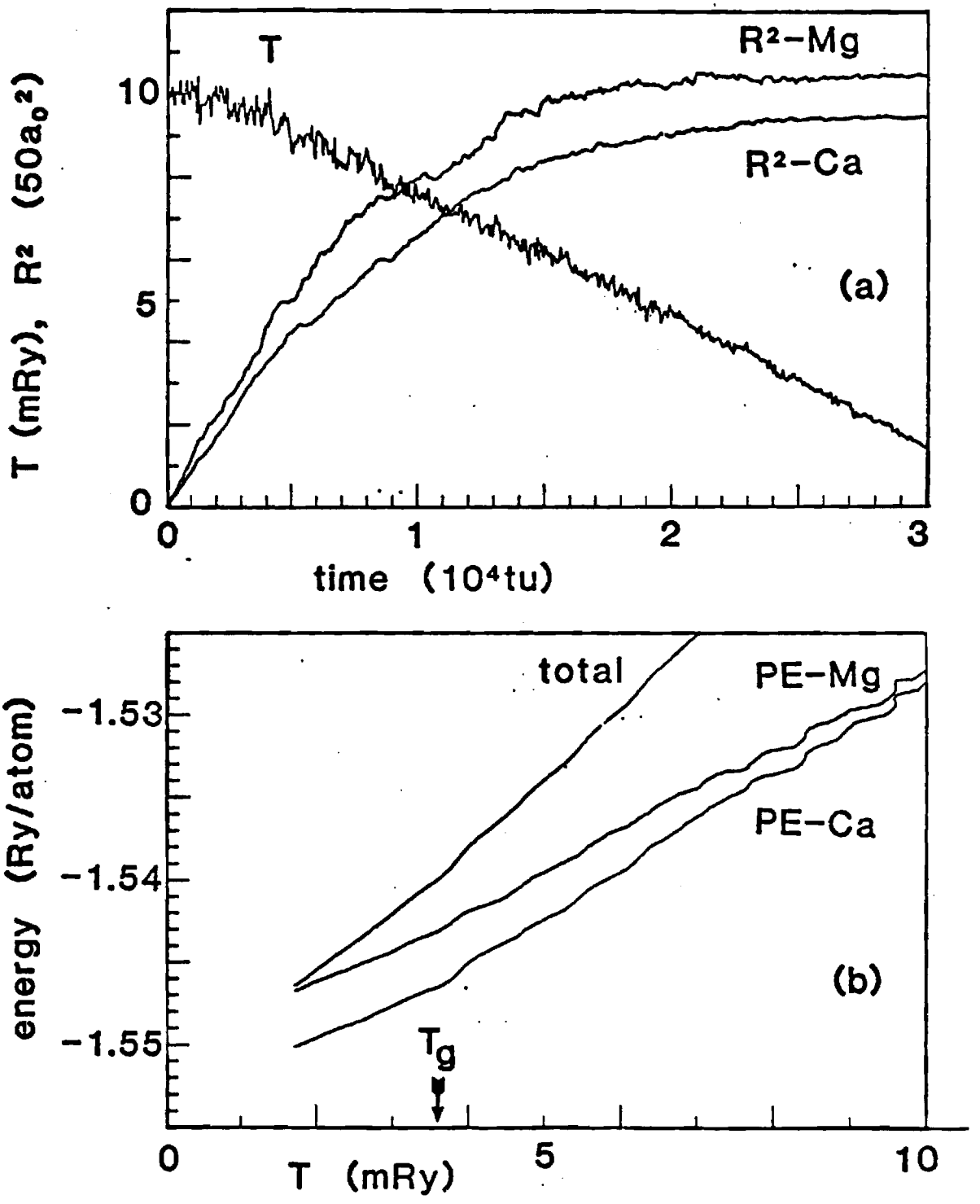
T
R²-Mg
R²-Ca
(a)
T (mRy), R² (50a₀²)
10
5
0
0
1
2
3
time (10⁴tu)
total
PE-Mg
PE-Ca
(b)
energy (Ry/atom)
-1.53
-1.54
-1.55
Tg
0
5
10
T (mRy)

FIGURE I

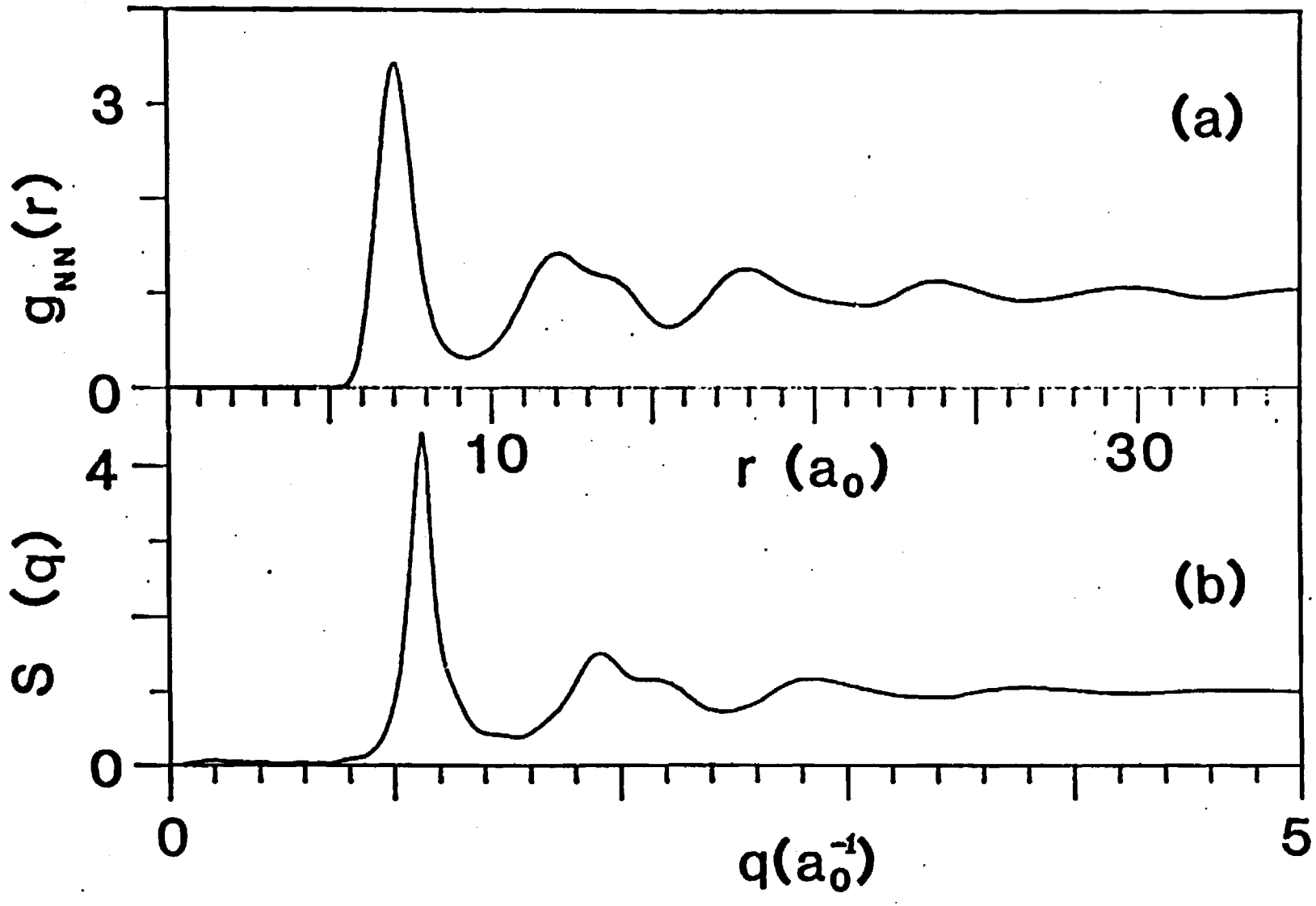

FIGURE 2

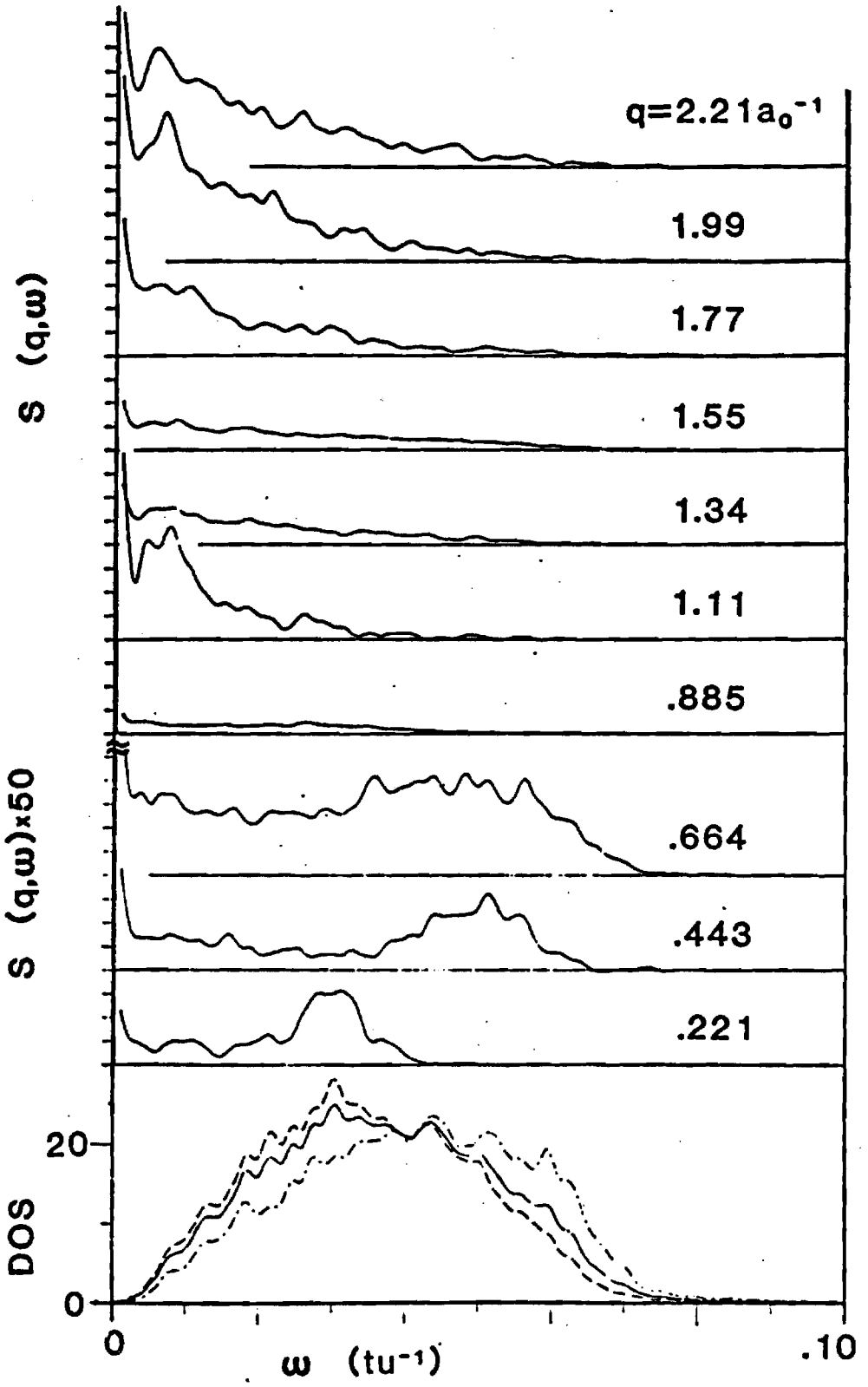
q=2.21a$_0^{-1}$
1.99
1.77
1.55
1.34
1.11
.885
.664
.443
.221
S (q,ω)
S (q,ω)×50
DOS
20
0
0
.10
ω (tu^{-1})

FIGURE 3